Report of Investigation 2016-

TSUNAMI INUNDATION MAPS FOR THE CITY OF SAND POINT, ALASKA

D.J. Nicolsky, E.N. Suleimani, and R.D. Koehler

PLACEHOLDER IMAGE

Place holder image caption here lalalalalala. Photo credit.

Published by

STATE OF ALASKA
DEPARTMENT OF NATURAL RESOURCES
DIVISION OF GEOLOGICAL & GEOPHYSICAL SURVEYS
2016

TSUNAMI INUNDATION MAPS FOR THE CITY OF SAND POINT, ALASKA

D.J. Nicolsky, E.N. Suleimani, and R.D. Koehler

Report of Investigations 2016-

State of Alaska
Department of Natural Resources
Division of Geological & Geophysical Surveys

STATE OF ALASKA

Bill Walker, *Governor*

DEPARTMENT OF NATURAL RESOURCES

Andy Mack, *Commissioner*

DIVISION OF GEOLOGICAL & GEOPHYSICAL SURVEYS

Steve Masterman, *State Geologist and Director*

Publications produced by the Division of Geological & Geophysical Surveys (DGGS) are available for free download from the DGGS website (www.dggs.alaska.gov). Publications on hard-copy or digital media can be examined or purchased in the Fairbanks office:

Alaska Division of Geological & Geophysical Surveys
3354 College Rd., Fairbanks, Alaska 99709-3707
Phone: (907) 451-5010 Fax (907) 451-5050
dggspubs@alaska.gov
www.dggs.alaska.gov

Alaska State Library
State Office Building, 8th Floor
333 Willoughby Avenue
Juneau, Alaska 99811-0571

Alaska Resource Library & Information Services (ARLIS)
3150 C Street, Suite 100
Anchorage, Alaska 99503-3982

CONTENTS

FIGURES

TABLES

APPENDICES

APPENDIX A

APPENDIX B

SHEETS

TSUNAMI INUNDATION MAPS FOR THE CITY OF SAND POINT, ALASKA

D.J. Nicolsky[1], E.N. Suleimani[1], and R.D. Koehler[2]

ABSTRACT

This study evaluates potential tsunami hazards for the city of Sand Point, on Popof Island in the Shumagin Islands archipelago. We numerically model the extent of inundation from tsunami waves generated by local and distant earthquake sources. We consider the results in light of historical observations. The worst-case scenarios are defined by analyzing results of the sensitivity study of the tsunami dynamics with respect to different slip distributions along the Aleutian megathrust. For the Sand Point area, the worst-case scenarios are thought to be thrust earthquakes in the Shumagin Islands region with magnitudes ranging from M_w 8.8 to M_w 9.0. We additionally consider a M_w 9.0 rupture between Shumagin Islands and Kodiak Island, a M_w 9.0 rupture of the Cascadia subduction zone, and a M_w 8.6 outer-rise rupture in the area of the Shumagin Islands. Results from the numerical modeling are intended to provide guidance to local emergency management agencies in tsunami inundation assessment, evacuation planning, and public education to mitigate future tsunami hazards.

INTRODUCTION

The Shumagin Islands lie on top of the Alaska–Aleutian subduction zone and have been shaped by volcanic eruptions, earthquakes, and erosion processes over the course of millions of years. Subduction of the Pacific plate under the North America plate has resulted in numerous earthquakes and still has the greatest potential to generate tsunamis in Alaska (Dunbar and Weaver, 2008). The Aleutian megathrust (fig. 1), the fault formed by the Pacific–North American plate interface, is the most seismically active tsunamigenic fault zone in the U.S. The latest sequence of great earthquakes along the Aleutian megathrust started in 1938 with a M_w 8.3 earthquake west of Kodiak Island (Estabrook and others, 1994). Four subsequent events—the 1946 M_w 8.6 Aleutian (Lopez and Okal, 2006), the 1957 M_w 8.6 Andreanof Island (Johnson and Satake, 1993), the 1964 M_w 9.2 Alaska (Kanamori, 1970), and the 1965 M_w 8.7 Rat Island (Wu and Kanamori, 1973) earthquakes—ruptured almost the entire length of the megathrust. Tsunamis generated by these great earthquakes reached Alaska coastal communities within minutes of the earthquake and resulted in widespread damage and loss of life (National Geophysical Data Center/World Data Service [NGDC/WDS] Global Historical Tsunami Database, 2013). Saving lives and property depends on how well a community is prepared, which further depends on estimating potential flooding of the coastal zone in the event of a local or distant tsunami.

Great historical earthquakes near Sand Point occurred in 1788, 1938, and 1946 and probably triggered some local tsunamis. Unfortunately, there are no comprehensive observations of these tsunamis in Sand Point (Lander, 1996). During the other historical events, no significant waves near the city of Sand Point were reported. However, the potential occurrence of damaging tsunamis at Sand Point must still be evaluated to develop inundation and tsunami evacuation maps. Local tsunamis can arrive within minutes after shaking is felt, leaving little time for warning or evacuation. Community preparedness is critical in the reduction of loss of life and property, and its effectiveness hinges on accurate estimates of potential coastal zone flooding in the event of a local or distant tsunami.

This work provides an in-depth analysis of the tsunami hazard in Sand Point and evaluates existing tsunami inundation maps. Our development of tsunami evacuation maps for a community consists of several stages. First we develop hypothetical tsunami scenarios on the basis of credible potential tsunamigenic earthquakes and submarine landslides. Then we perform model simulations for each of these scenarios and compare the results with historical tsunami observations, if available. Finally we develop a "worst-case" inundation line that encompasses the maximum extent of flooding based on model simulation of all credible source scenarios and historical observations. The worst-case inundation line becomes a basis for local tsunami-hazard planning and evacuation map development.

The Sand Point tsunami inundation maps described in this report represent the results of collaborative efforts between State and Federal agencies[3] to produce inundation maps for many of Alaska's coastal communities. In this report, we generally provide both metric and imperial units of measure. If it is necessary to quote existing data, we state

[1]Geophysical Institute, University of Alaska, P.O. Box 757320, Fairbanks, Alaska 99775-7320; djnicolsky@alaska.edu

[2]Alaska Division of Geological & Geophysical Surveys, 3354 College Road, Fairbanks, Alaska 99709-3707; now at Nevada Bureau of Mines and Geology Mackay School of Earth Science and Engineering, University of Nevada, Reno, 1664 North Virginia Street, MS 178, Reno, Nevada 89557

[3]To help mitigate the hazard that earthquakes and tsunamis pose to Alaska coastal communities, the Alaska Tsunami Mapping Team (ATMT) was created. It consists of personnel from the Geophysical Institute at the University of Alaska Fairbanks and from the State of Alaska Division of Geological & Geophysical Surveys. The ATMT participates in the National Tsunami Hazard Mitigation Program (NTHMP) by evaluating and mapping potential inundation of selected parts of the Alaska coastline using numerical tsunami modeling.

that data in the original and metric units of measure. One foot (1 ft) is approximately 0.305 meters (0.305 m), and one mile (1 mi) is approximately 1.609 kilometers (1.609 km).

This report is intended for use by scientists, engineers, and planners interested in applying the approach to the development of tsunami inundation and evacuation maps. Digital data and documentation provided with the report enable technical users to explore the range of tsunami inundation expected for future events.

PROJECT BACKGROUND: REGIONAL AND HISTORICAL CONTEXT

SETTING

The community of Sand Point (55° 20′ N, 160° 29′ W), also known as Qagan Tayagungin, with a population of 1,018 (Alaska Department of Labor & Workforce Development [DLWD], 2013), is situated along the shore of Humboldt Harbor on Popof Island. Popof Island is part of the Shumagin Islands archipelago (fig. 2), immediately southwest of the Alaska Peninsula. Figure 3 shows the location of the Shumagin archipelago relative to Kodiak Island, Sanak Island, and Unalaska Island. The rupture areas of the latest sequence of great earthquakes are shown by red shaded regions.

Sand Point's economy is based on the fishing industry and a large transient population is employed at the local cannery. According to the Alaska Department of Commerce, Community, and Economic Development's Division of Community and Regional Affairs (Alaska DCRA, 2013), Sand Point was founded in 1898 by a San Francisco-based fishing company as a trading post and cod-fishing station. Aleuts from surrounding villages, such as Unga Village, and Scandinavian fishermen were the first residents of the community. Today the city is home to the largest fishing fleet in the Aleutian Islands chain and hosts a major fish processing plant that provides fuel and other services. Sand Point is characterized as self-sufficient and progressive, with commercial fishing activities at the heart of the local culture. Almost half the inhabitants are of Aleut descent, mainly from the Qagan Tayagungin tribe, and support themselves by fishing and fish processing.

The city government was incorporated in 1966. Sand Point has a state-owned airport with a 4,000 foot runway that is accessible (weather permitting) by daily direct flights from Anchorage. During the summer months and into the fall the Alaska Marine Highway operates the M/V Tustumena, a mainline ferry vessel that stops in Sand Point four times per month. From Sand Point the ferry travels to King Cove, Cold Bay, False Pass, and Dutch Harbor.

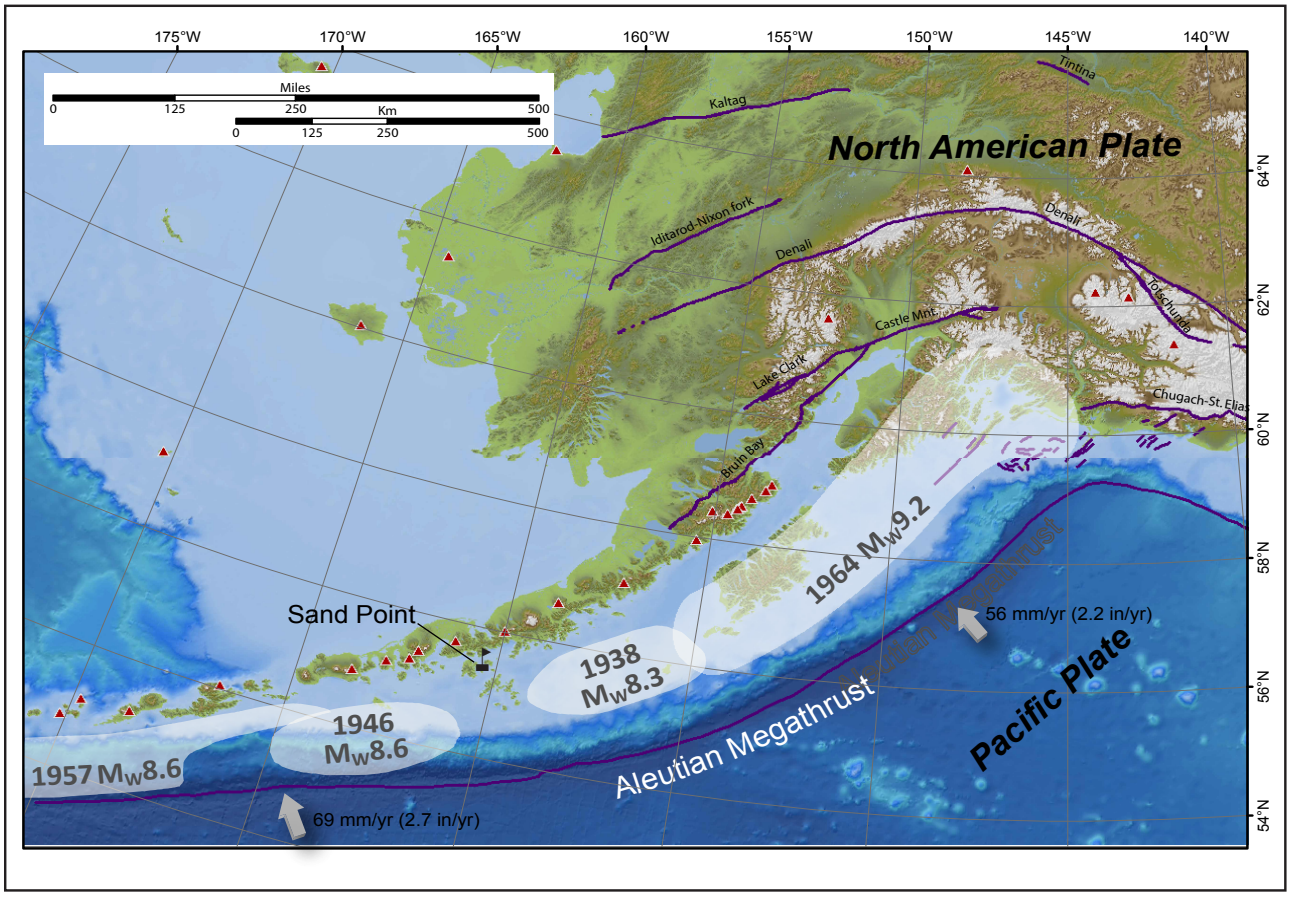

Figure 1. Map of south-central Alaska and the Alaska Peninsula, identifying major active or potentially active faults (purple lines) and rupture zones of the 1938, 1946, 1948, 1957, 1964, 1965, 1986, and 1996 earthquakes (light shaded areas).

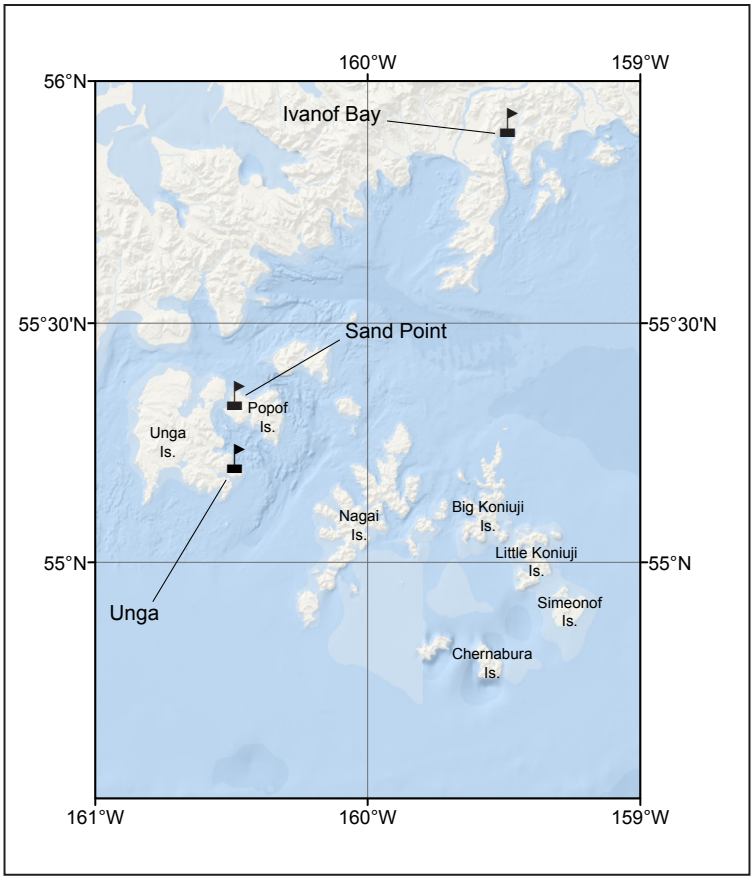

Figure 2. Map of Shumagin Islands archipelago, showing locations of the city of Sand Point and the abandoned village of Unga.

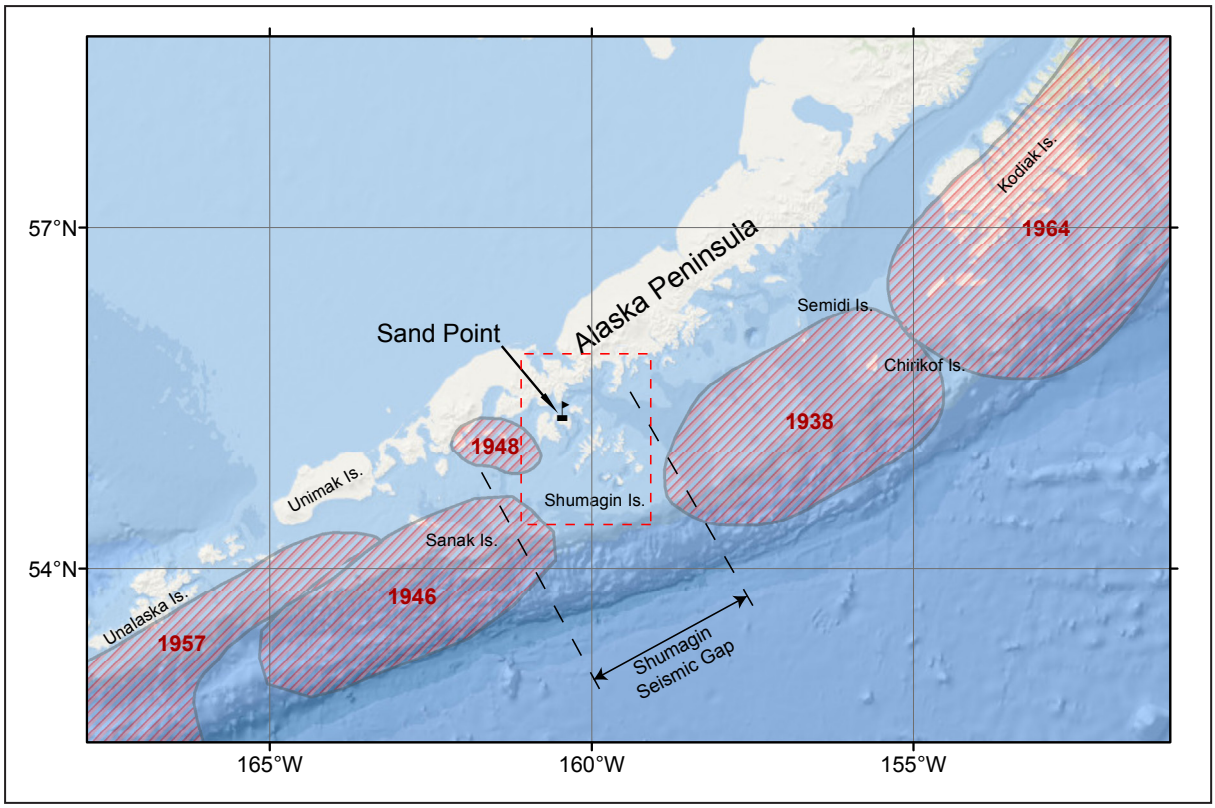

Figure 3. Map of the Alaska Peninsula from Kodiak Island to Unalaska Island. The rupture areas of the latest sequence of great earthquakes are shown by hatched shapes. The red-dashed rectangle marks the spatial extent of the map shown in figure 2.

SEISMIC AND TSUNAMI HISTORY

Popof Island constitutes a part of the Shumagin Islands archipelago of about 20 islands, near the boundary where the Pacific and North American plates converge and form the Alaska–Aleutian subduction zone (AASZ). The rate of plate convergence near the archipelago is approximately 63–66 mm (2.5–2.6 in) per year (DeMets and others, 1990; Page and others, 1991; Argus and others, 2010) and this segment of the megathrust has produced some significant tsunamigenic earthquakes.

In the 20th century, the 1938 M_W 8.3 earthquake ruptured a segment of the megathrust east of Popof Island. The segment is bounded by the Shumagin Islands on the west and by the Chirikof Islands on the east. A lack of high-quality instrumental records (the event occurred before the deployment of the World Wide Standardized Seismograph Network) left the 1938 rupture area poorly defined. A tsunami was recorded in Seward, Dutch Harbor, and Sitka with a maximum amplitude of 0.08 m (0.26 ft) at Sitka. There are no known observations of this tsunami in the Shumagin Islands (Lander, 1996), although this earthquake occurred in direct proximity to the islands.

To the west of the Shumagin Islands, near the tip of Alaska Peninsula, another great earthquake (M_W 8.6) occurred in 1946. This earthquake generated a destructive tsunami along the Alaska shore with as much as 35 m (115 ft) of runup near Scotch Cap on Unimak Island (Lander, 1996). The tsunami also impacted Hawaii and caused minor damage in California before traveling to such distant countries as Chile, Japan, French Polynesia, New Zealand, and other remote parts of the Pacific Ocean.

Between the 1938 and 1946 rupture zones is the Shumagin seismic gap, a segment of the active fault that has not slipped in a long time compared to nearby areas. The seismic gap is about 250 km (155 mi) long and is capable of producing a M_W 8.2 earthquake. Only three significant earthquakes, the 1917 M 7.4 (Estabrook and Boyd, 1992), the 1948 Ms 7.5 (Davies and others, 1981), and the 1991 M 7.1 (National Earthquake Center [NEC], 2013), ruptured some areas of the gap. For more information, see the in-depth discussion of the seismicity and tectonic setting of the Shumagin seismic gap in Davies and others (1981). Kowalik and Murty (1984) published what is likely the first study devoted to numerical modeling of the tsunami dynamics resulting from a major earthquake in the gap. An unanswered question in the analysis of the Shumagin seismic gap seismicity and in its tsunami-generating capacity is whether this region has previously ruptured and generated a significant tsunami. A key to its answer lies in the analysis of great historical and prehistoric earthquakes near the Shumagin Islands.

One of the greatest historical earthquakes in the study area occurred in 1788. Unfortunately, little is known about its rupture area and the sequence of events. After reviewing multiple eyewitness accounts and reports, Soloviev (1968; translated to English in 1990) hypothesized that the 1788 earthquake might have ruptured from Kodiak Island through the Shumagin seismic gap to Sanak Island (fig. 4). A closer examination of the historical records revealed that two consequent earthquakes occurred, on July 22 and August 7, 1788 (Davies and others, 1981). The first event presumably ruptured from Kodiak to Unga Island, while the second ruptured from Unga to Sanak Island. The tsunami maximum amplitude on Sanak Island during the second event was 30 m (~100 ft), while the tsunami was not even observed on Kodiak (Lander, 1996).

Kirby and others (2013) discuss an alternative hypothesis based on Emile Okal's interpretation of the events. In particular, they state that "…a large earthquake occurred on 22 July somewhere along the subduction margin between the Gulf of Alaska and Sanak Island and that 16 days later, on 7 August, a large submarine landslide occurred near the southwest end of the Alaska Peninsula that was triggered as a delayed response by the ground motions of the earlier 22 July earthquake." The latter alternative hypothesis is somewhat supported by a recent discovery, in which Miller and Von Huene (2014) found a recent submarine landslide that might have contributed to the tsunami generation mechanism during the 1946 event. A similar submarine mass failure on the continental slope could have caused the 1788 tsunami.

According to Winslow and Johnson (1989), the occupation of Unga Island by Native Shumagin people ended in 1788 as a result of the destruction and abandonment of the last Native village on the island, most likely from tsunami inundation. We emphasize that in addition to the major tectonic tsunami in 1788, a dormant Augustine Volcano began to erupt (Lander and Lockridge, 1989). The cause of the volcanic eruption is outside the scope of this report; nevertheless, we mention that an erupting volcano in the area of potential inundation can hinder post-tsunami relief efforts and should be considered in future multi-hazard scenarios.

Numerous earthquakes have been felt in Sand Point since the 1800s. Figure 5 shows seismic activity along the Alaska–Aleutian subduction zone with locations determined by the Alaska Earthquake Center (AEC) at the University of Alaska Fairbanks. Davies and others (1981) provide a regional map showing seismicity near the Shumagin Islands. The epicenters and dates of the most significant historical events are shown in figure 6. Following is a description of Sand Point and Unga seismic events according to the National Geophysical Data Center (NGDC) Global Historical Tsunami Database and references therein.

1840–1860s

A series of strong earthquakes affected the Alaska Peninsula (fig. 2 of Davies and others, 1981). The most relevant to this study is an earthquake on April 15, 1847. According to Doroshin (1870, p. 41, translated by J.B. Kisslinger in Davies and others, 1981), "Early in the morning of the same date there was a fairly large earthquake on Unga. At 10:00 a.m. it grew to the point that one could not remain standing." We note that the credibility of the eyewitness reports might be compromised due to multiple citations and translations.

According to Davies and others (1981), the 1847 event is thought to have ruptured the 1938 zone and also at least half of the Shumagin seismic gap. This hypothesis is strengthened

by Lander and Lockridge (1989) who, in turn, refer to Cox and Morgan (1977), noting that a local tsunami was observed along the north coast of Maui, Hawaii, in 1848. Cox and Morgan (1977) suggest that this tsunami might have been generated north of Hawaii. Unfortunately, there are no reports of the tsunami along the Alaska coast, and the extent of the 1848 tsunami remains unknown.

May 15, 1868 Event

According to Lander (1996), who refers to Perry (1875, p. 51) and Tarr and others (1912, p. 89), during a slight earthquake the water became agitated and it rose at Unga to over 6 m (~20 ft); however, it is not clear whether the elevation refers to the height of the wave, the height of the runup, or uplift of the land.

November 10, 1938 Event

A major submarine M_w 8.3 earthquake (Stover and Coffman, 1993; Johnson and Satake, 1994) with a source along the Alaska Peninsula was recorded west of Kodiak. Shaking was felt strongly in Unimak and False Pass. A tsunami followed and was recorded at several tide gauges. However, no observations of the tsunami event were reported from Sand Point or Unga. According to Lander (1996), the very small size of this tsunami for such a great earthquake is unexplained.

April 1, 1946 Event

A strong M_w 8.6 earthquake (Lopez and Okal, 2006) near Unimak Island triggered a major destructive tsunami in the Pacific Ocean. Local waves reached 35 m (115 ft) in height on Unimak Island, 6.1 m (20 ft) in Cold Bay, 3 m (10 ft) in King Cove, and about 1.5 m (5 ft) in Chignik. An Unga school paper reported that at about 4 a.m. several people were awakened by the earthquake, which was followed by a tidal wave (Foster, 1946). The wave swept away two dories and the dock from the old fishing station across the bay. Debris from the dock was found on Agate Beach, about a mile away. Sand and gravel shifted. The "comber waves", with heights of 1.2–1.5 m (4–5 ft), continued rolling into the bay up to eight hours after the earthquake (Lander, 1996).

Simeon Pletnikof, a long-time resident of Nikolski, on Umnak Island, reported that he was aboard a ship at Sand Point when the ship rose and fell repeatedly through a large vertical range (telephone conversation, August 3, 1994, reported in Lander, 1996).

March 28, 1964 Event

The M_w 9.2 Alaska earthquake of 5:36 p.m. March 27, 1964, shook south-central Alaska and generated the most devastating tsunami in Alaska history. Simultaneously, with the major tectonic tsunami generated by an ocean-floor displacement, multiple local tsunamis were generated by submarine landslides; in some glacial fjords, the local runup reached up to 52 m (170 ft) (Plafker and others, 1969). Because the local tsunamis arrived within minutes after the onset of the earthquake, they caused most of the damage and accounted for 76 percent of tsunami fatalities in Alaska (Lander, 1996). The recorded amplitude of the 1964 tsunami in Sand Point is unknown.

Unfortunately, historical records are usually too short to sample the variability of slip at the megathrust (Stein and Okal, 2007). Paleotsunami and paleoseismic studies have the potential to extend available historical records back in time and thus help to develop hypothetical maximum credible scenarios. The most relevant paleoseismic study in the Shumagin Islands was conducted by a U.S. Geological Survey (USGS) expedition in 2011. The goal was to investigate effects of the 1788 tsunami and to collect evidence of tectonic deformation at the outer Shumagin Islands. Simeonof Island, the closest island to the trench, was chosen as a good candidate, based on archeological study by Winslow and Johnson (1989). The latter interpreted coastal landforms on Simeonof Island as tectonically uplifted marine terraces. However, the USGS expedition determined that there is no evidence for either sudden coseismic land-level changes produced by great earthquakes or any trace of marine deposits left by high tsunamis (written commun., R. Witter). Coastal sediment suggests that relative sea level has risen slowly over the past 3,400 years and shows no sign of sudden coseismic displacements evident at other subduction zones (Witter and others, 2014). Based on this information, Witter and others (2014) inferred that possible ruptures of the megathrust beneath Simeonof Island might have caused coseismic uplift or subsidence that was too small to be recorded in the onshore sediments. The implications of this geologic/paleoseismologic study on the development of the hypothetical tsunami scenarios are discussed later in the report.

LANDSLIDE-GENERATED TSUNAMI HAZARDS IN SAND POINT

Alaska has a long recorded history of tsunamis generated by submarine and subaerial landslides, avalanches, and rockfalls (Kulikov and others, 1998). An essential prerequisite for the occurrence of submarine slumps or landslides is the accumulation of sediments on underwater slopes and the consequent oversteepening of unconsolidated deposits. The sediment accumulation typically occurs at the mouths of glacier-fed rivers, creeks, streams, and artificial fills. The ground shaking and presence of elevated pore pressure in sediments appear to be the key factors responsible for the triggering of landslides (Keefer, 1984; Kulikov and others, 1998; Masson and others, 2006). The absence of substantial glacial creeks near the city of Sand Point reduces a potential for catastrophic submarine mass failures near Sand Point. Moreover, the relatively shallow bathymetry in Humboldt Harbor will probably impede hypothetical slides from reaching large velocities and causing sudden and significant displacement of the water column. Therefore, we assume that the potential for catastrophic local submarine landslides in Humboldt Harbor is probably low.

A number of potential locations for submarine slump failures on the continental shelf are shown in figure 6. Unfortunately, little is known about the extent, volume, and locations of these potential landslides and even less is

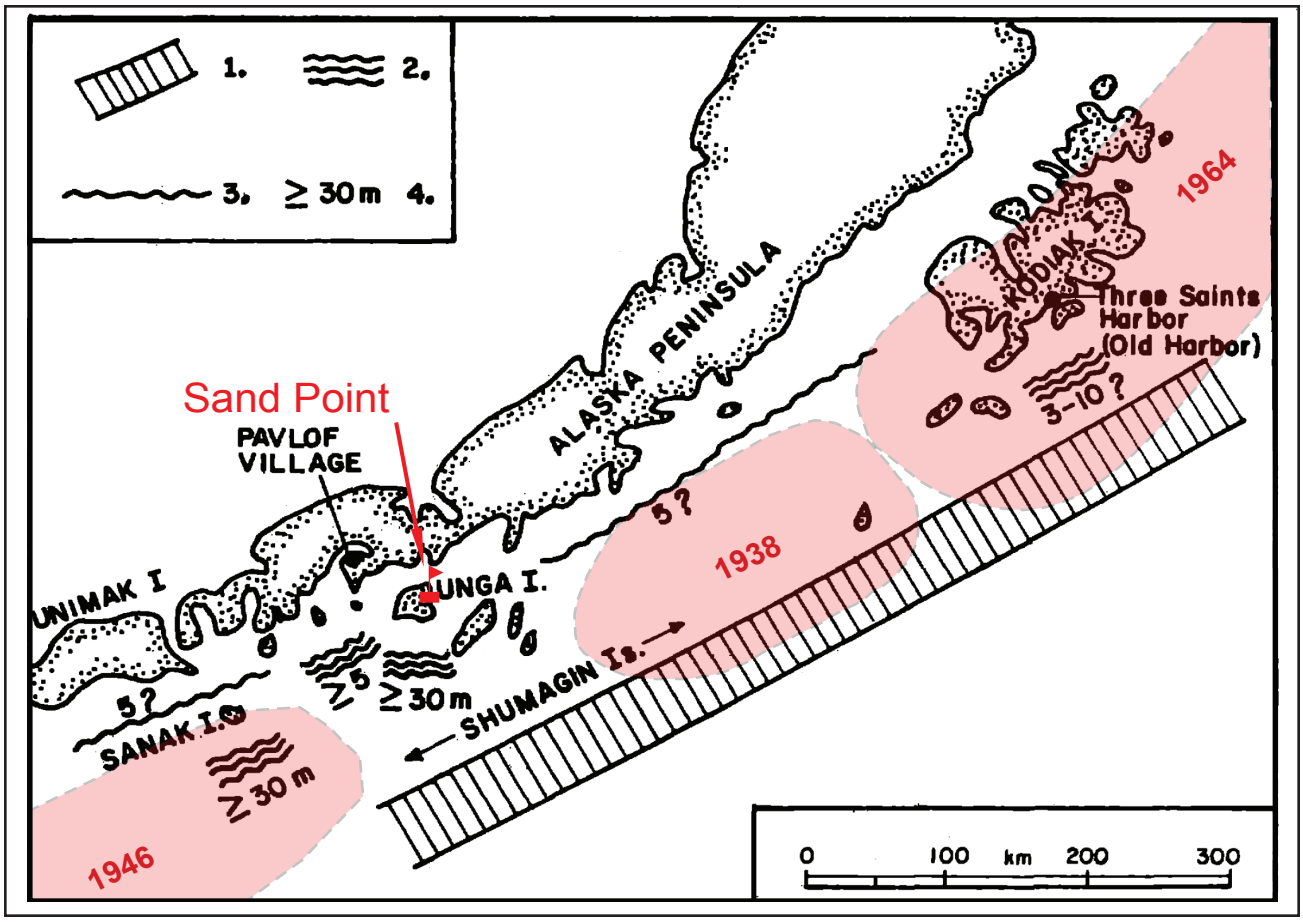

Figure 4. Source region and observations of the 1788 tsunami according to Soloviev (1968, fig. 1). Legend symbols: 1. Presumed location of earthquake rupture zone; 2. Sites where tsunami was actually observed; 3. Possible sites where tsunami was observed; 4. Approximate tsunami heights (in meters). Locations of significant historical ruptures are outlined by transparent red shapes.

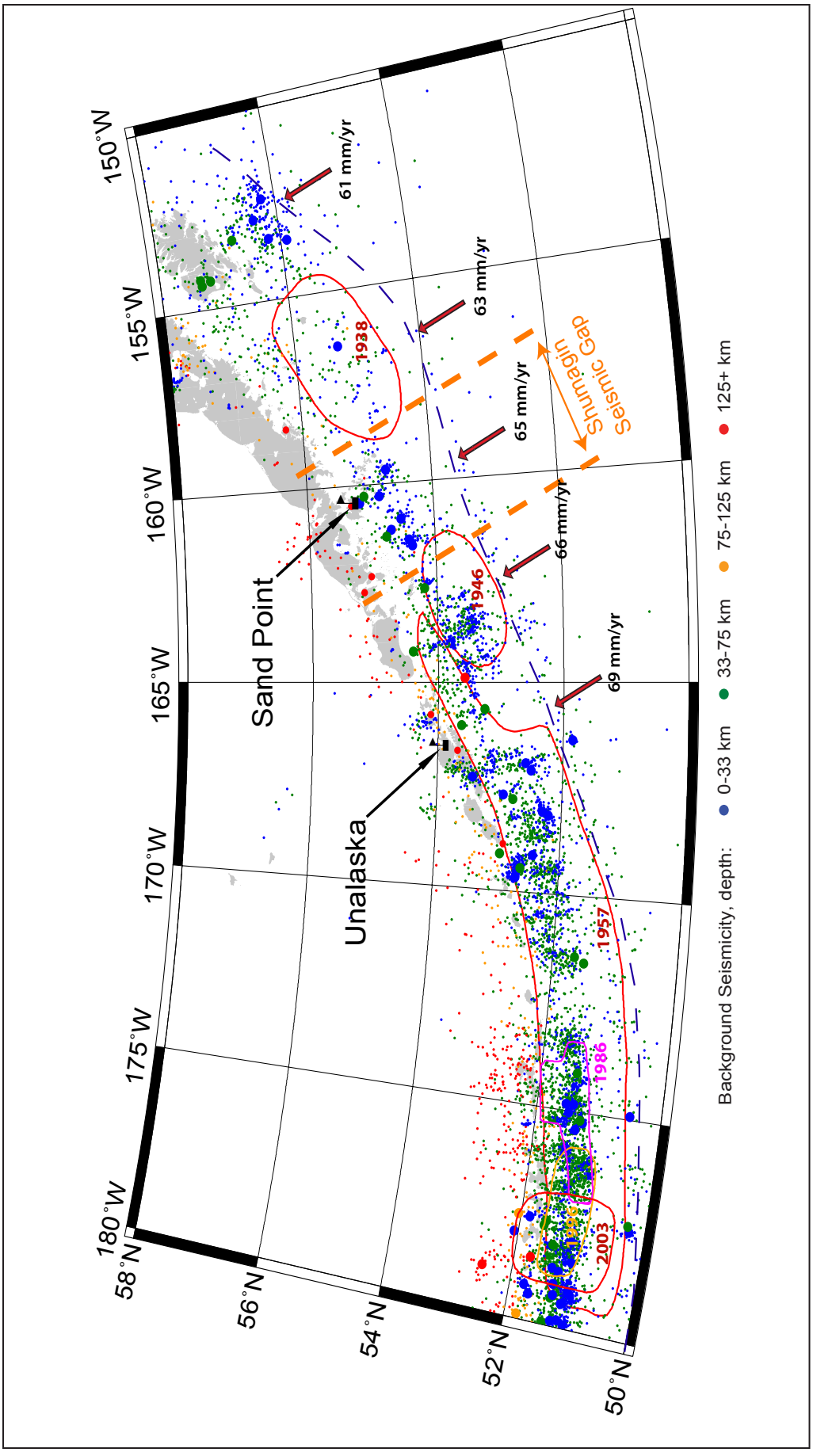

Figure 5. Earthquakes along the Alaska Peninsula and Aleutian Islands, from the Alaska Earthquake Center catalog. Small dots correspond to earthquakes of magnitude less than 5; large dots mark earthquakes of magnitude 5 or greater. Red/orange/magenta contours mark locations of previous rupture zones, determined by aftershocks recorded in the catalog. Red arrows indicate varying rates of convergence between the Pacific and North American plates. The trench is marked by dashed blue line. Location of the Shumagin seismic gap is noted by heavy orange dashed lines.

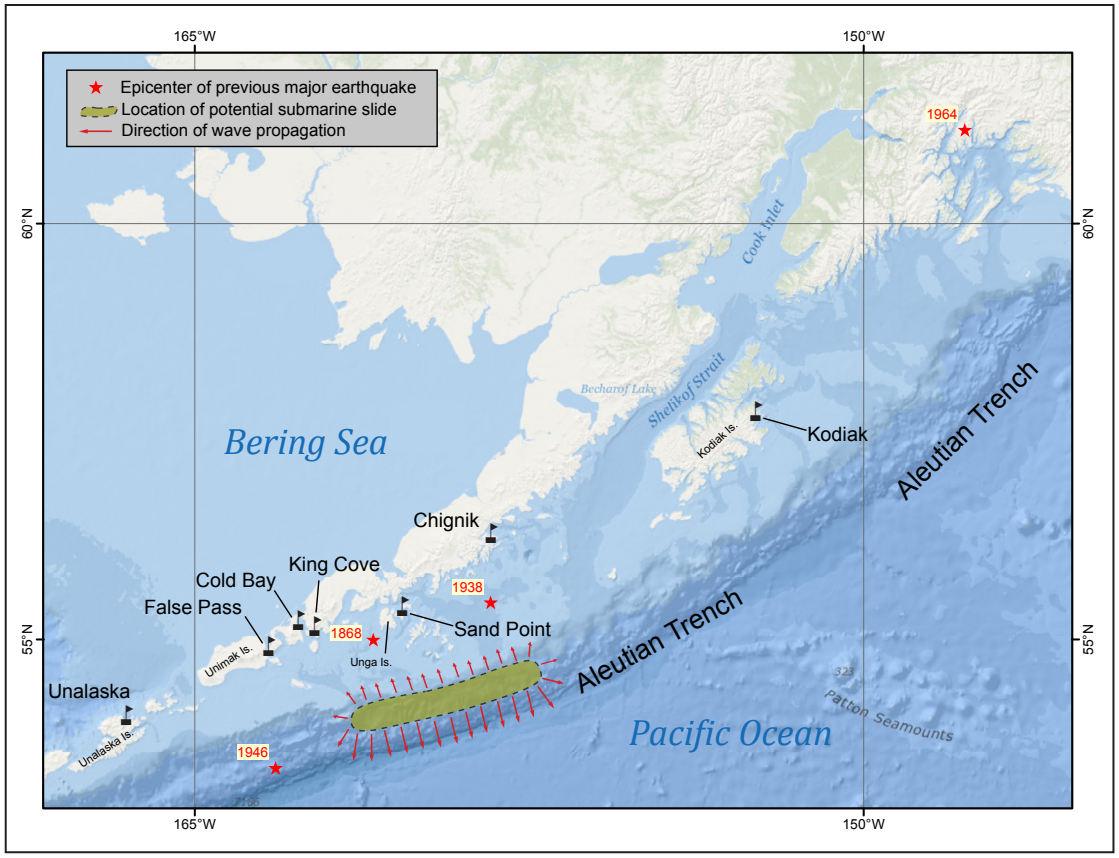

Figure 6. Map of the northern Pacific Ocean; red stars show epicenters of major earthquakes associated with water disturbances observed in Sand Point. Gold shaded area marks location of potential submarine landslides near the Aleutian Trench; red arrows indicate directions of potential landslide-generated waves.

known about the slope stability in these areas. Nevertheless, it is known that massive landslides along continental slopes can cause great tsunamis. The Storegga submarine landslide (Bryn and others, 2005) and the Grand Banks submarine landslide (Fine and others, 2005) generated catastrophic tsunamis along the coastlines of Norway and Canada, respectively. While the Grand Banks failure had a seismogenic trigger, there is still a debate regarding the trigger for the Storegga slope failure (Kvalstad and others, 2005; Atakan and Ojeda, 2005). Similarly, Grilli and others (2013) discuss the simultaneous generation of the 2011 Tohoku-oki tsunami by both tectonic processes and submarine mass failures. In Alaska high-resolution seismic profiles were used to determine the location of the submarine landslide that may have caused the 35 m (115 ft) wave runup at Unimak Island during the 1946 tsunami (Miller and others, 2014). The 1946 tsunami was probably generated by the combination of tectonic deformation and a submarine mass failure triggered by the earthquake, as earlier hypothesized by Fryer and Watts (2001). Schwab and others (1993) provide a valuable discussion of submarine mass wasting in Alaska. Numerical simulations of potential landslide-generated tsunamis along the Aleutian Arc are possible (for example, Waythomas and others, 2009), but plausible determination of the landslide location, thickness, and volume is a challenging task. For example, our preliminary modeling of a potential 200 km3 mass failure at Umnak Plateau in the Bering Sea (slide volume is estimated from the GLORIA images by Carlson and others [1991], p 44) shows that a simulated wave in Unalaska/Dutch Harbor could be similar in height to a tsunami generated by a local M_w 9.1 earthquake. However, these simulations as well as others for Sand Point require more scientific research to further constrain potential slide locations and their volumes before wave inundations can be estimated with any certainty.

In addition to underwater submarine slumps and landslides, subaerial slope failures are also known for their destructive power to generate tsunamis. In light of recent field observations in western Passage Canal, a steep-walled glacial fjord in south-central Alaska, we augmented the tsunami modeling and mapping report for the city of Whittier and western Passage Canal with an additional hypothetical rockfall-generated tsunami scenario (Nicolsky and others, 2011b). Similar steep mountain slopes are present along the coastlines of Popof and Unga islands, which are thus susceptible to avalanches, debris flows, and rockfalls. However, these potential failures are not close to the community and thus would not necessarily generate a significant local tsunami in Sand Point. Finally, we emphasize that our ability to model the effects of potential rapid subaerial mass failures and the subsequent impact of the resulting tsunami on the community depends on our knowledge of the type and geometry of the mass movement, local bedrock geology, and location. Landslide assessments on Popof and Unga islands are limited and the location and geometry of these potential

mass failures are currently unknown. While numerical simulations of potential rockfall/landslide/avalanche-generated tsunamis are possible, more field data and scientific research are necessary to constrain the landslide sources before meaningful results can be generated.

In this report we do not model tsunamis generated by mass failures due to insufficient data on the locations and volumes of these potential hazards[4].

METHODOLOGY AND DATA

GRID DEVELOPMENT AND DATA SOURCES

One of the challenges in tsunami modeling is that the governing equations for water dynamics are continuous. In this work, we discretize the shallow-water equations in spherical coordinates on the Arakawa C-grid using a finite difference method. To resolve water dynamics around the certain topographic/bathymetric feature, the grid must be fine enough, with at least four points to parameterize its spatial dimensions; more points are often necessary to achieve satisfactory results in practice. To compute a detailed map of potential tsunami inundation triggered by local and distant earthquakes we employ a series of nested computational grids. A nested grid allows for higher resolution in areas where it is needed without expending computer resources in areas where it is not. The bathymetric and topographic relief in each nested grid are based on digital elevation models (DEMs) developed at the National Geophysical Data Center (NGDC) of the National Oceanic & Atmospheric Administration (NOAA). The extent of each grid used for the Sand Point mapping is shown in figure 7 and listed in table 1. The coarsest grid, with 2-arc-minute (approximately 2 km) resolution, spans the central and northern Pacific Ocean. The highest-resolution grid for Sand Point covers a part of Popof and Unga islands as well as the strait between these two islands. The spatial resolution of the high-resolution grid cells, with about 16 × 16 m (53 × 53 ft) dimensions, satisfies NOAA minimum recommended requirements for computation of tsunami inundation (National Tsunami Hazard Mapping Program [NTHMP], 2010).

The bathymetric data for the 2-arc-minute-resolution grid is extracted from the ETOPO2 dataset (NGDC/NOAA). To develop 8/3-, 8- and 24-arc-second-resolution grids, shoreline, bathymetric, and topographic digital datasets were obtained from the following U.S. federal and academic agencies: NOAA's National Ocean Service (NOS), Office of Coast Survey, and National Geophysical Data Center (NGDC); and the U.S. Army Corps of Engineers (USACE). All data were shifted to World Geodetic System 1984 (WGS 84) horizontal and Mean Higher High Water (MHHW) vertical datums. Bathymetric datasets used in the compilation of the Sand Point DEMs included NOS hydrographic surveys, a recent USACE harbor survey, NOAA Electronic Navigational Charts, multi-beam swath sonar surveys, and NGDC trackline surveys. The topographic dataset was obtained from the 1-arc-second NASA Space Shuttle Radar Topography Mission (SRTM). The data sources and methodology used to develop high-resolution, 8/3-, 8-, and 24-arc-second DEMs are described in detail by Love and others (2012). According to Love and others (2012), the vertical accuracy of the high-resolution DEM is highly dependent on the source datasets contributing to DEM cell values. The SRTM dataset with vertical accuracy of 10–15 m (Caldwell and others, 2009; Love and others, 2012). Topographic National Elevation Database (NED) data have an estimated accuracy of 7–20 m. Bathymetric areas have an estimated accuracy of between 0.1 m (3.9 in) and 5 percent of water depth.

Because the high-resolution topography in the NOAA DEMs can have large vertical errors near the shoreline, prediction of potential tsunami inundation can be invalid. Hence, this topographic dataset is augmented with a real-time kinematic (RTK) GPS survey in the harbor areas and along nearshore areas in Sand Point. The survey in Sand Point was conducted September 7–9, 2011. Locations of the GPS measurements are shown in figure 8. The collected GPS measurements had 0.03–0.05 m (1.2–2 in) lateral and vertical accuracy with respect to the base station (Leica Geosystems AG, 2002). Therefore, to achieve sub-meter accuracy for all GPS measurements related to the MHHW datum, the base station datum must be known with respect to the MHHW datum with sub-meter accuracy. Such base station accuracy can be achieved if the base station is set up at a well-known benchmark or monument. We could not find a conveniently located benchmark in Sand Point during the survey, so we used the technique described below to convert the collected GPS measurements into the MHHW datum.

During the survey we took GPS measurements of the sea surface height at some partially enclosed locations where the water was relatively still (for example, in the harbor), as shown by the red arrow in figure 9-I. Sea level was measured at low and high tides as well as at some intermediate tide stages. Therefore, the measured tide level, denoted by H_2, is known relative to the base station datum at some instance of time, t_k, with an accuracy of several centimeters. Here, k stands for the k–th measurement of the sea level.

The tide level, $H_1(t)$, with respect to the MHHW datum is observed every 6 minutes at the NOAA tide stations in Sand Point. We calculated the vertical shift between the MHHW datum and the base station datum by finding a difference (in the least square sense) between the GPS-measured sea level, H_2, and the NOAA-observed sea level, H_1, at the instances t_k. The results of the least square fitting for Sand Point are shown in figure 9-II. Once the vertical shift is calculated, we apply the same shift to all collected GPS measurements and convert the entire survey to the MHHW datum.

[4]Guidelines and best practices for tsunami inundation modeling for evacuation planning state that the modeling should add value to mapping products (National Tsunami Hazard Mapping Program [NTHMP], 2010).

We check the accuracy of our conversion of the GPS data to the MHHW level by estimating the height of the NOAA tidal station disk '1293-1 1984' in Sand Point. According to the "NOAA Tides & Currents" website (http://tidesandcurrents.noaa.gov/), the disk is set 1.592 m (5.22 ft) above the MHW, or 1.376 m (4.51 ft) above the MHHW. After measuring the height of this disk during the GPS survey and converting to the MHHW datum, we estimate that the disk is 1.368 m (4.49 ft) above the MHHW. The difference of 0.008 m (0.026 ft) between the NOAA stamping and our estimates demonstrates that the conversion of the GPS measurements to the MHHW level provides sub-meter accuracy in Sand Point. Finally, we note that the collected GPS measurements have the WGS84 horizontal datum, with a horizontal accuracy of approximately 3–5 m (10–16 ft) (Leica Geosystems AG, 2002). The converted GPS survey has been provided to the NGDC, where the high-resolution DEM of Sand Point and adjacent areas were developed. The DEM verification against the GPS measurements, as well as some adjustments, are completed by the authors at the Geophysical Institute, University of Alaska Fairbanks.

NUMERICAL MODEL OF TSUNAMI PROPAGATION AND RUNUP

The numerical model currently used by the Alaska Earthquake Center (AEC) for tsunami inundation mapping has been validated through a set of analytical benchmarks and tested against laboratory and field data (Nicolsky and others, 2011a; Nicolsky, 2012). Refer to Synolakis and others (2007) and NTHMP (2012) for further details. Additional description of the employed numerical model is provided in Nicolsky and others (2015). We conducted all model runs using bathymetric data that correspond to the MHHW tide level in Sand Point.

MODELING OF THE MARCH 11, 2011, TOHOKU TSUNAMI

As part of this project, we present a model verification study of the Tohoku tsunami of March 11, 2011. We emphasize that among the many reasons for distant tsunami event model verification listed in Synolakis and others (2007), it is most important to check the consistency of the DEM nesting.

After the 2011 Tohoku earthquake, several deformation models were published to represent the slip distribution; we apply the finite fault model III by Shao and others (2011). For each fault, we calculate the corresponding vertical coseismic deformation using Okada's (1985) formulas. The resulting vertical deformation is illustrated in figure 10. Figure 11 shows a comparison between the observed wave dynamics at several DART (Deep-ocean Assessment and Reporting of Tsunamis) buoys along the central and eastern Aleutian Islands. The computed and measured water-level dynamics agree relatively well for the first two to three hours after the wave arrival at the buoy. After this interval, waves reflected from the shore started to arrive at the buoys and the computed wave is not in phase with the observed tsunami dynamics. Similar to Tang and others (2012), we observe a time delay between the computed and observed waves. The computed wave arrives at the DART buoys δT = 7–8 minutes sooner than the observed one.

Additionally, we compare the computed and measured water-level dynamics at the Sand Point tidal station (fig. 11-IV). The catastrophic Tohoku tsunami produced a 0.61 m (2 ft) wave in Sand Point (NOAA/WDS Global Historical Tsunami Database), whereas the simulation predicts a 0.4 m (1.3 ft) wave. The wave with the maximum height arrived at Sand Point 15 hours after the first wave and was probably caused by a superposition of incident, reflected, and trapped waves around the Shumagin Islands archipelago. We infer that the employed numerical code does not accurately model the reflected and trapped waves of the 2011 tsunami because the resolution of the DEM is coarse in the vicinity of Sand

Table 1. Nested grids used to compute the propagation of tsunami waves generated in the Pacific Ocean to the community of Sand Point. The high-resolution grids are used to compute the inundation. Note that the grid resolution in meters is non uniform and is used to illustrate grid fineness near Shumagin Islands archipelago. The first dimension is the longitudinal grid resolution; the second is the latitudinal resolution.

Grid name	Resolution		West–East boundaries	South-North boundaries
	arc-seconds	meters (near Shumagin Islands)		
Level 0, Northern Pacific	120 × 120	≈ 1,850 × 3,700	120°00'E – 100°00'W	10°00'N – 65°00'N
Level 1, Eastern Aleutians	24 × 24	≈ 430 × 740	171°58'W – 157°02'W	52°00'N – 57°28'N
Level 2, Coarse-resolution Shumagin Islands	8 × 8	≈ 140 × 250	161°30'W – 157°30'W	54°36'N – 56°36'N
Level 3, Fine-resolution Shumagin Islands	8/3 × 8/3	≈ 47 × 82	160°54'W – 159°48'W	54°43'N – 55°37'N
Level 4, High-resolution Sand Point	8/9 × 8/15	≈ 16 × 16	160°33'W – 160°27'W	55°16'N – 55°22'N

Point and the model is affected by the accumulation of wave dispersion effects over time. We also note that the time delay between computed and measured water-level dynamics is increased to $\delta T = 10$ minutes. A similar time lag is observed by Tang and others (2012). The probable cause of this increase is errors in the bathymetry and some dispersion effects.

The far-field Tohoku tsunami did not result in a significant wave at Sand Point because of the long distance from the source area to the Shumagin Islands archipelago and directivity patterns of the energy propagation. However, other distant events might produce greater wave heights in Sand Point and cannot be dismissed without a proper evaluation.

The numerical modeling of this historical tsunami demonstrates that the employed numerical model of tsunami propagation and runup generates tsunami waveforms that are in good agreement with the observed arrival times and wave phases. The model also provides a good approximation to the recorded tsunami amplitudes in Humboldt Harbor, at least for the first few hours after the arrival of the tsunami, which indicates that the proposed coseismic deformation model adequately describes the coseismic slip distribution, and the DEM nesting is selected appropriately. The long oscillatory pattern of the waves in Humboldt Harbor makes it necessary to consider computation of the potential tsunamis for at least 18 hours after initial arrival.

TSUNAMI SOURCES

It is believed that all of the devastating great events along the Alaska–Aleutian arc occurred on the megathrust—the contact surface between the subducting Pacific plate and the North American plate. Along the Alaska Peninsula, the Pacific plate subducts underneath the North American plate at a relative convergence rate of about 60–70 mm/yr (2.36–2.76 in/yr) (DeMets and others, 1990; Page and others, 1991; Argus and others, 2010). Because of friction on the megathrust, the two converging tectonic plates generally cohere to each other at depths shallower than 25–40 km (16–25 mi), and thus shear stress builds up inside the plates along the megathrust. The shear stress is typically released instantaneously during an earthquake, and the seismic energy propagates through the ground, causing strong ground shaking. The shear stress is accumulated in the seismically coupled regions of the megathrust (Scholz, 1998; Wang and Dixon, 2004). In creeping regions, where the converging plates manage to slip relative to each other, a lesser amount of shear stress accumulates, and hence the seismic energy released during earthquakes can be small. Therefore, before discussing hypothetical tsunamigenic earthquakes near the Shumagin Islands archipelago, we review some aspects of the regional plate tectonics and locations of the seismically coupled and creeping zones along the Aleutian megathrust. We exploit limits of the seismically coupled regions near Sand Point to parameterize spatial extents of hypothetical ruptures. A consecutive sensitivity study helps us to analyze waves arriving at each community by varying a location of the idealized rupture in the seismically coupled region. Results of the sensitivity study are then applied to construct maximum credible scenarios.

Delineating Earthquake Rupture Zones in the Shumagin Islands

Extensive research has been conducted to find seismically coupled regions in various subduction zones (Uyeda, 1982; Pacheco and others, 1993; Tichelaar and Ruff, 1993; Uchida and others, 2009; Scholz and Campos, 2012). Most of the research is focused on determining the spatial extent of the seismically coupled zone, and its updip and downdip limits (fig. 12). It is thought that the coupled regions can be determined by locating rupture zones of previous great earthquakes (Kelleher and others, 1973; Kato and Seno, 2003). The rupture zone of any significant earthquake is typically delineated by the pattern of aftershocks. The aftershocks region is thought to extend down to the boundary between the seismically coupled and uncoupled regions of the megathrust (Tichelaar and Ruff, 1993).

There has not been a great earthquake rupture along the megathrust beneath the Shumagin Islands archipelago in historical time. The last significant earthquake, Ms 7.5, occurred in the study area in 1948, before the deployment of the World Wide Standardized Seismograph Network. Sykes (1971) located two aftershocks, on May 15 and 17, at depths of 48 and 44 km (30 and 27.3 mi), respectively. Thus, the 1948 event probably involved rupture at depths below 40 km (25 mi) (Davies and others, 1981). Detailed analyses of this event are reported in Davies and others (1981) and in the seismic recordings captured by the Shumagin Islands Network in the 1970s. Additional analysis of other significant thrust earthquakes along the Alaska Peninsula can be found in Tichelaar and Ruff (1993).

Historical earthquake events, such as those in 1938, 1946, 1957, and 1964, can be used to divide the subduction zone into along-strike seismic segments. Segment boundaries can be estimated by the distribution of aftershocks related to these great historical earthquakes. The Alaska–Aleutian plate interface has been divided into ten segments from the western Aleutians eastward to Prince William Sound (Nishenko and Jacob, 1990). The boundaries between the segments might be 'barriers', which could survive through many earthquakes (Aki, 1984). It is possible that during future events, segments might rupture separately or together (Sykes and others, 1981; Aki, 1984), hence a thorough study of worst-case scenarios is necessary for development of tsunami inundation maps for Sand Point.

Defining Updip and Downdip limits of the hypothetical rupture

From the seismologic point of view, earthquakes tend to occur in the brittle part of Earth's lithosphere (Byrne and others, 1988). Thus, in addition to analyzing previous great earthquakes, Tichelaar and Ruff (1993) proposed to map thrust earthquakes with a magnitude larger than 5.5 along the subduction zone. The seismically coupled region is thought to be capable of generating thrust earthquakes, and mapping their locations could help to find the downdip limit of the coupled zone. Locations of these earthquake epicenters and earthquake slip patches along the Alaska Peninsula are

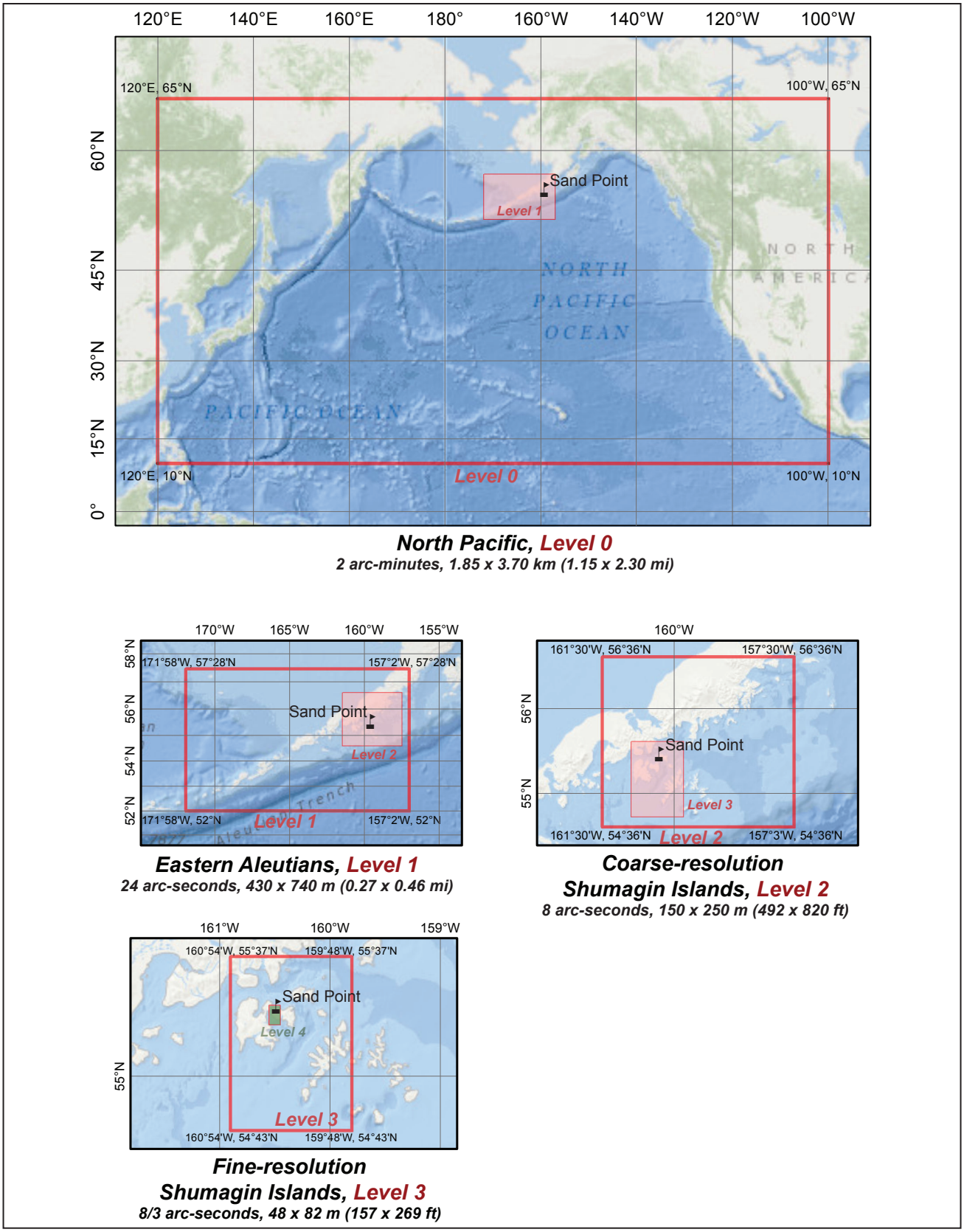

Figure 7. Nesting of bathymetry/topography grids for numerical modeling of tsunami propagation and runup. The coarsest grid, Level 0, covers the central and northern Pacific Ocean area. Location of each subsequent embedded grid is marked by a red rectangle. Maps of the high-resolution grids, Level 4, are not shown because these grids do not nest any other grids. The red semi-transparent rectangles mark areas of the grid refinement.

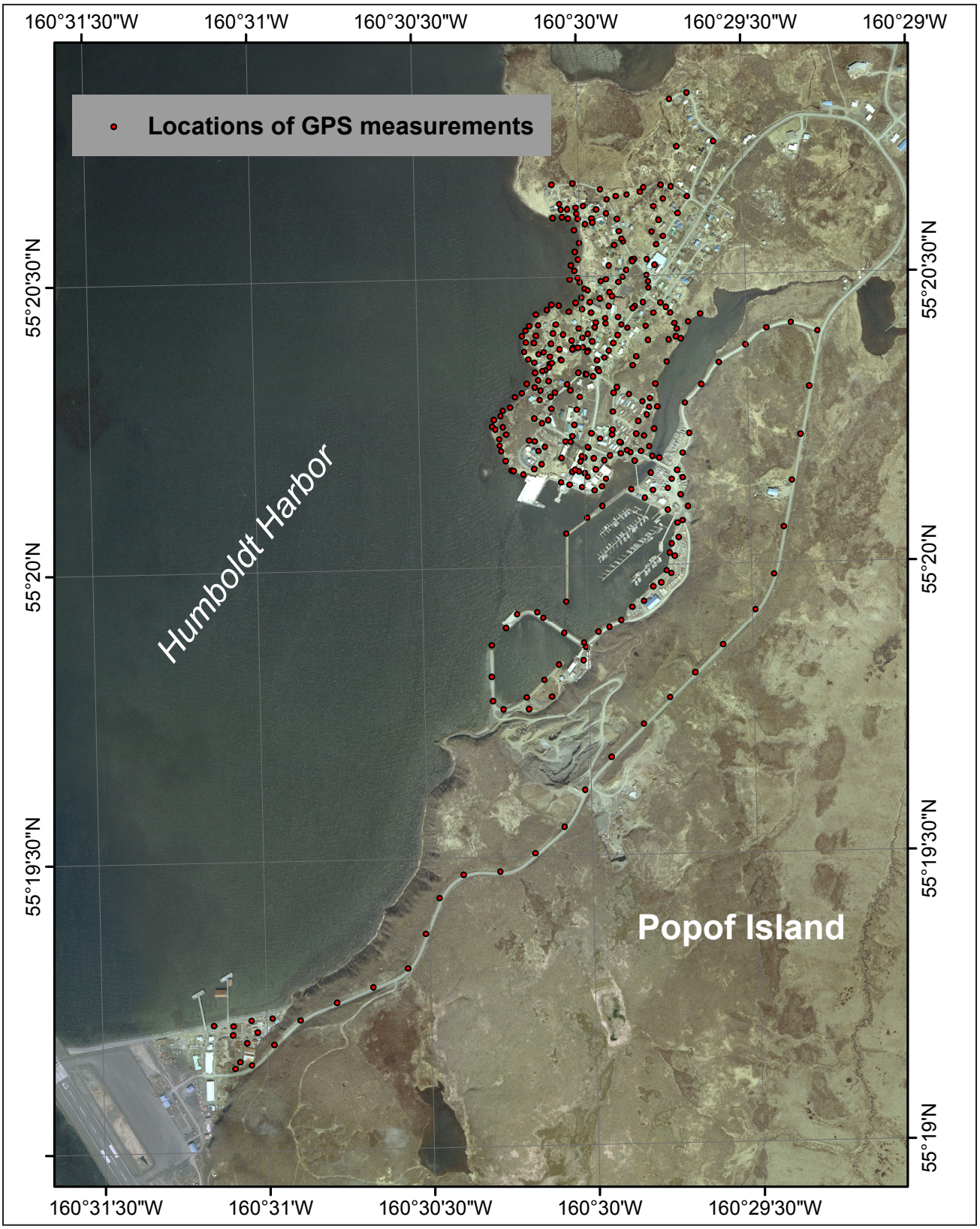

Figure 8. Locations of real-time kinetic global positioning system (RTK GPS) measurements at Sand Point.

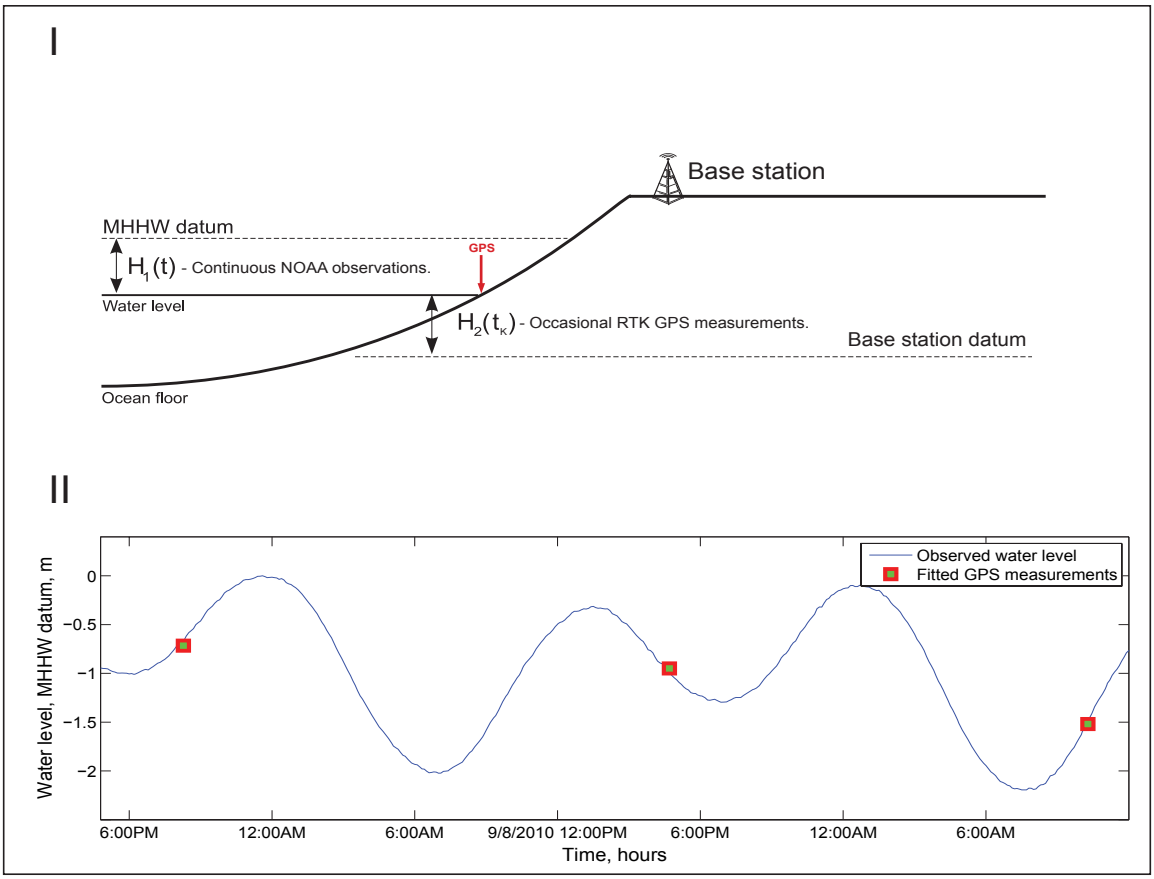

Figure 9. (I) Measurement of sea level in MHHW datum and relation of base station datum to MHHW datum. (II) Predicted water-level dynamics in Sand Point and fitted GPS measurements of water level in MHHW datum.

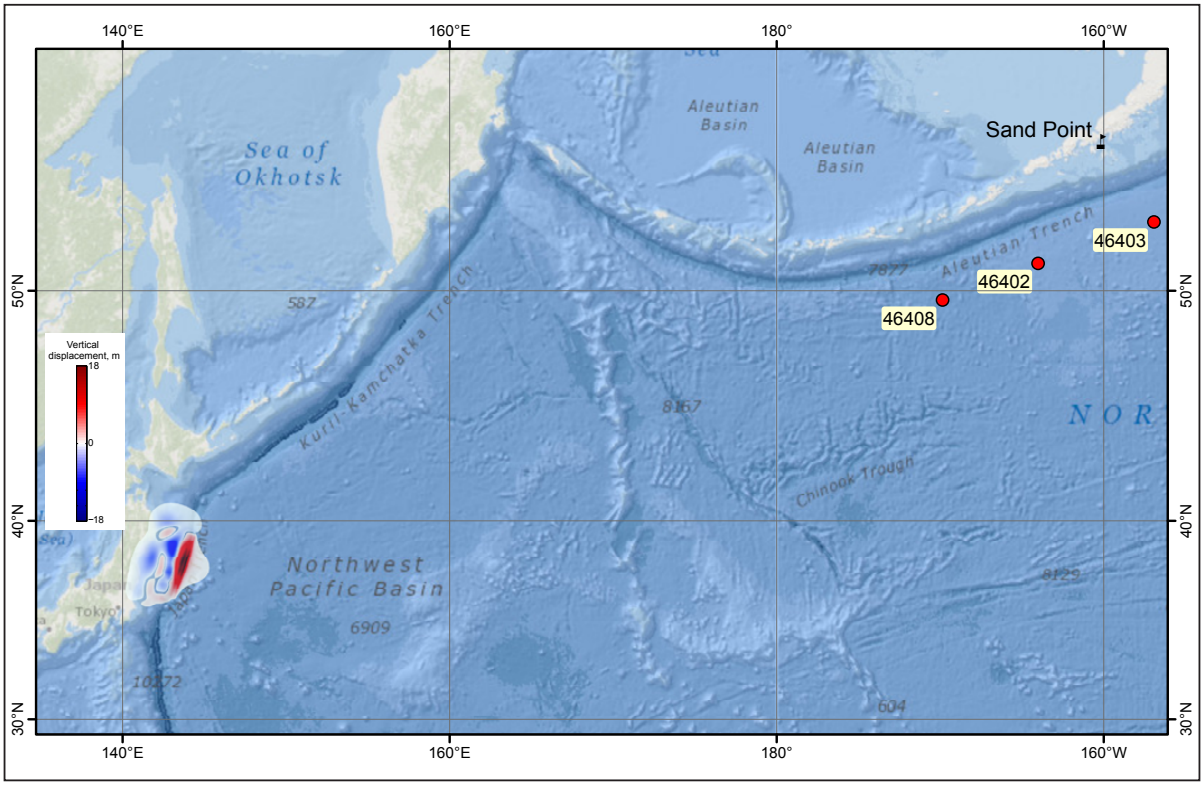

Figure 10. Vertical deformations of the ocean floor and adjacent coastal region (in meters) corresponding to Japan's March 11, 2011, Tohoku earthquake, based on finite fault model III by Shao and others (2011). Red indicates uplift; blue indicates subsidence. Red circles denote locations of numbered DART buoys near Unalaska.

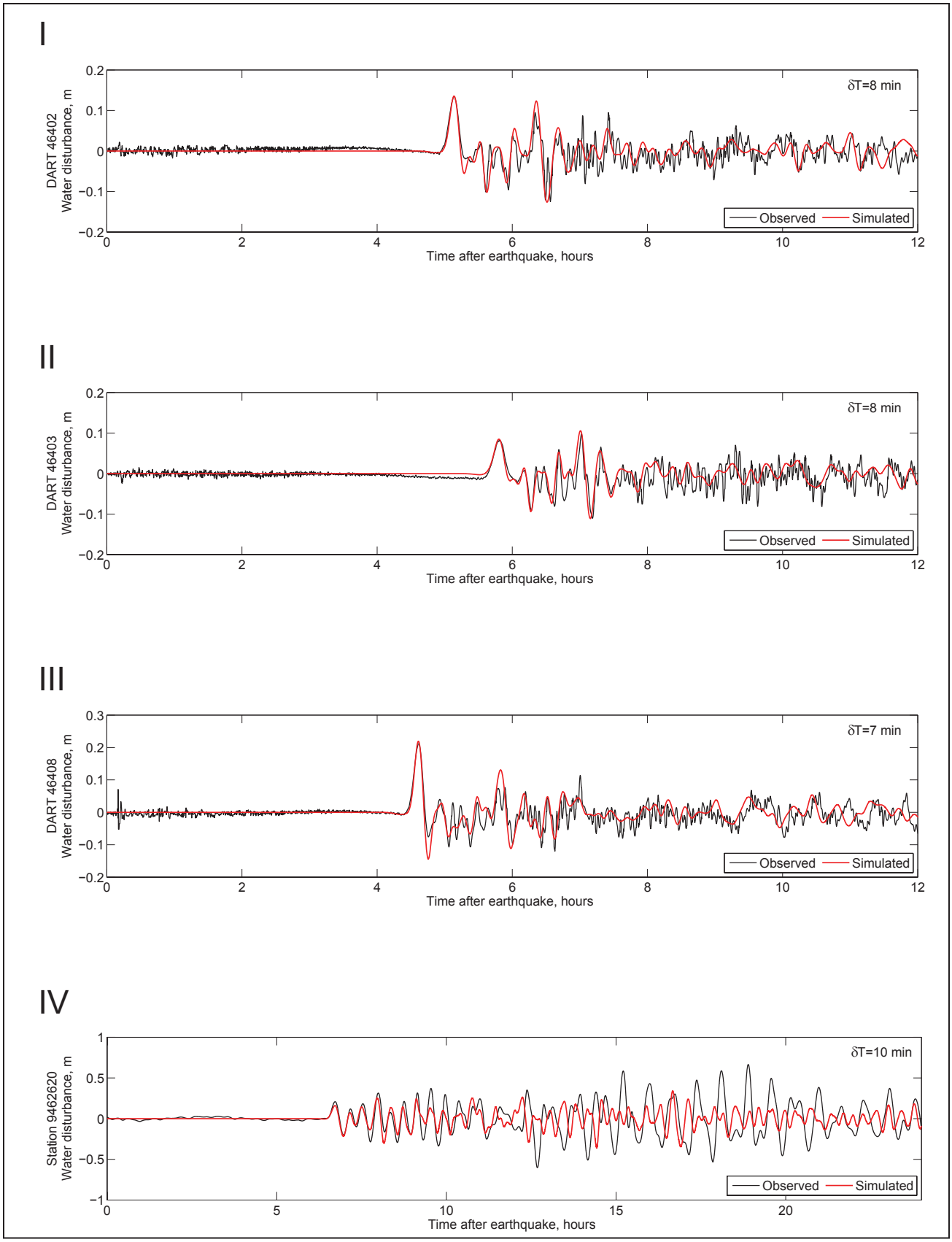

Figure 11. Modeled water-level dynamics at DART buoys 46402 (I), 46403 (II), and 46408 (III), and the tide station 9462620 in Sand Point (IV) during the March 11, 2011, tsunami.

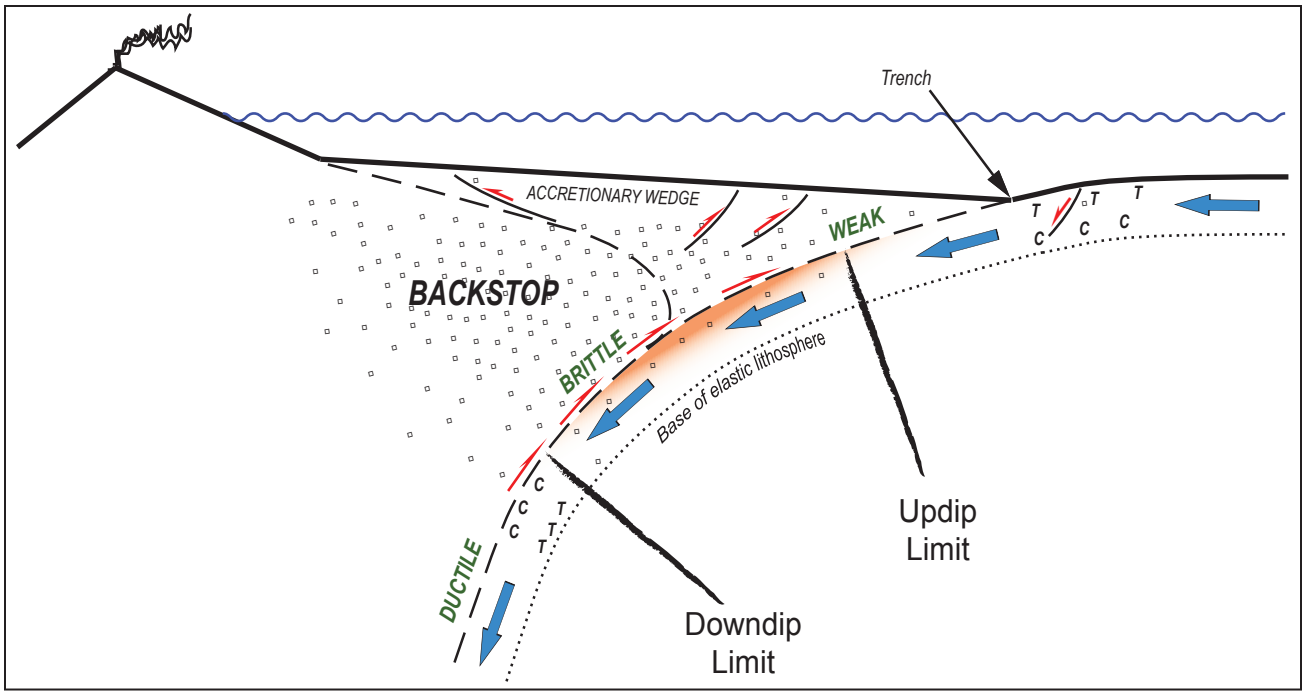

Figure 12. Conceptual model illustrating forearc morphological elements and locations of active faults. Upper plate seismicity is shown by small squares, extending down to the limit of the brittle region. Approximate locations of updip and downdip limits of the locked zones are shown by thick black lines. Locations of intraplate bending-related normal (tensional) and thrust (compressional) events are shown by letters T and C, respectively. The locked region is marked by orange shading. Modified after Byrne and others (1988).

shown in figure 13. It is consequently inferred that seismic coupling along the Aleutians extends down to a depth of 37–41 km (23–25.5 mi). See Tichelaar and Ruff (1993) for further details.

With the availability of new data and techniques, assessment of the downdip limit of the seismogenic zone can be completed by analyzing upper plate seismicity (Ruff and Kanamori, 1983; Tichelaar and Ruff, 1993); modeling the thermal regime of the plates (Chen and Molnar, 1983; Hyndman and others, 1995); and by analyzing the electrical resistivity (Heise and others, 2013), gravity (Song and Simons, 2003), and magnetic anomalies (Blakely and others, 2005). Refer to Tichelaar and Ruff (1993) and Kaye (2003) for further details.

Ground temperature and pressure are thought to be the primary factors controlling for the downdip limit of the coupled region. For example, as temperature and pressure increase with depth, the mechanical properties of subaerial materials change, and rocks constituting Earth's lithosphere become more plastic. It is thus theorized that great earthquakes probably only occur in regions where certain temperature, pressure, and structural conditions prevail (Oleskevich and others, 1999). Unfortunately, no single physical process alone can explain the observed downdip extent of thrust earthquakes. The modeling techniques typically incorporate many assumptions and uncertainties regarding the mechanical and thermal properties of subaerial materials and can only provide first-order approximations of the seismogenic zone.

A more accurate method to determine locations of seismically coupled regions is the analysis of crustal deformation using the elastic dislocation theory following the approach of Savage (1983). Fletcher and others (2001), Zweck and others (2002), and Cross and Freymueller (2008) use geodetic observations of strain accumulation to assess active deformation along the Aleutian subduction zone. The locations of strongly seismically coupled segments derived from geodetic data are in agreement with gravity modeling studies by Song and Simons (2003).

Modeling results for the Fox Island region are presented in Cross and Freymueller (2008). The interface between the Pacific and North American plates along the Alaska Peninsula and Shumagin Islands is divided into several rectangular, planar segments (fig. 14). The seismic coupling coefficient—the ratio between the observed seismic moment release rate and the rate calculated from plate tectonic velocities—is estimated for each plane by inverting available geodetic data. According to Scholz and Campos (2012) the geodetic estimate of seismic coupling is free of most of the uncertainties related to calculation of the seismic moment releases from scarce observations, which mainly involve problems of sampling rare events. In the geodetic inversions, the zero coupling (being unlocked) is assigned to a plane where the tectonic plates are creeping or freely slipping between great earthquakes, while a 100 percent value of coupling (being fully locked) is associated with the plane that exhibits no slip in the interval between great earthquakes and slipping uniformly at the time of a great earthquake. The modeling results by Cross and Freymueller (2008) reveal that the tec-

tonic plates near Plane 2 are neither fully locked nor creeping, and indicate that some shear stress might be accumulating. The plate coupling coefficient for each plane is marked by percentage values shown by red values in figure 14. Note that most of the magnitude 6+ earthquakes recorded by the AEC from 1980 to 2013 are near the Shumagin Islands at the downdip end of Plane 2, around 37 km (23 mi) in depth. The estimated downdip extent of seismic coupling quantitatively agrees with the analysis of upper plate seismicity by Tichelaar and Ruff (1993). Tichelaar and Ruff (1993) predict the downdip limit of the locked region to be at 37–41 km (23–25.5 mi) depth, which is in agreement with the geodetic inversions.

Determining the location of the updip limit of the locked zone is hindered by the lack of geodetic data close to the Aleutian trench. For example, the indicated zero coupling at Plane 1 has large modeling uncertainty. Recent studies by Ryan and others (2012) and Kirby and others (2013), who compared the Alaska and Tohoku margins, imply that a hypothetical rupture might propagate to shallow depths, similar to the M_w 9.0 Tohoku earthquake. The occurrence of a Tohoku-type earthquake in the Shumagin Islands region is partially supported by gravity data (Song and Simons, 2003). These authors show that a predominantly negative trench-parallel gravity anomaly (TPGA) persists west of the Shumagin Islands, and that the negative TPGA coincides with regions where previous great earthquakes (such as the 1960, 1964, 1957, and 1965) have occurred. Unfortunately, as we mentioned earlier, there is no single study that can resolve whether a certain region of plate interface is capable of producing large coseismic displacements, and hence for the sake of finding the plausible worst-case scenario we assume that the tectonic plates near the trench might be coupled.

In the rest of this section we develop several hypothetical tsunamigenic earthquake models based on the assessment of locked regions near the Shumagin Islands. In particular we conduct a sensitivity study to determine the location along the plate interface where an earthquake could trigger a damaging tsunami in Sand Point. We focus on the Shumagin seismic gap as one of the locations for a potential earthquake (Davies and others, 1981). For each modeled hypothetical slip distribution on the plate interface, we simulate an impact of the potential tsunami in Sand Point. Consequently, we incorporate the paleoseismic findings of Witter and others (2014) and conduct an additional sensitivity analysis. Finally, as other potential tsunami sources we consider a rupture of the Cascadia subduction zone involving the Juan de Fuca plate from mid Vancouver Island in British Columbia to northern California, and a Tohoku-type earthquake in the Shumagin Islands region.

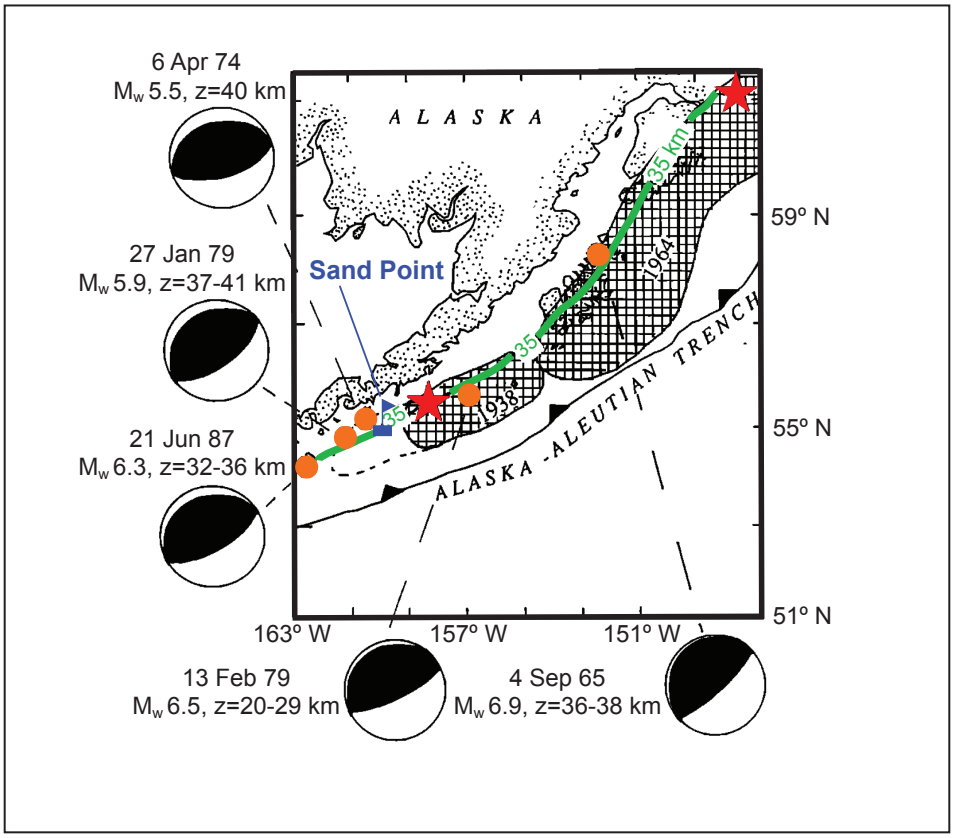

Figure 13. Epicenters (solid orange dots) of underthrusting earthquakes north of the trench and their associated depths and focal mechanisms (fig. 9 of Tichelaar and Ruff, 1993). Epicenters (red stars) and aftershock regions (crosshatched) of the 1964 and 1938 earthquakes are also shown. The 35 km (21.7 mi) depth contour of the plate interface, inferred from the earthquake depths, is shown by a solid green line. Seismic coupling extends down to 37–41 km (23–25.5 mi).

Sensitivity Study

We conducted a sensitivity study to assess what distribution of slip on the Aleutian megathrust would create the largest tsunami at Sand Point. For the Simeonof segment, east of Sand Point, the potential slip distributions are significantly constrained as there have been no sudden coseismic vertical land-level changes greater than 0.3 m (1 ft) produced by great earthquakes at Simeonof Island (Witter and others, 2014). This observation means that if there have been great earthquakes rupturing that segment of the megathrust, Simeonof Island must lie very close to the hingeline—the line of zero vertical displacement that separates the region of uplift near the updip end of the rupture from the region of subsidence near the downdip end of the rupture. However, for the segment to the west of Sand Point, no paleoseismic constraints are available and a wider range of slip distributions is geologically plausible. We evaluated the tsunamis generated by ruptures at different depths on the megathrust, both alone and in combination, finally determining a geologically plausible worst-case scenario.

To simulate potential earthquakes on the Aleutian megathrust we employ a model of the Alaska–Aleutian plate interface between the subducting and overriding plates. The plate interface model by Hayes and others (2012) is discretized into a number of rectangles ranging from 3 to 6 km (1.8–3.7 mi) in the along-strike direction of the plate interface. The upper and lower edges of each rectangle coincide with 1 km (0.62 mi) depth contours of the reconstructed plate interface (fig. 15). The rectangles, called subfaults, are later used to compute coseismic ground deformation (Okada, 1985). We simulate tsunami sources on the finite fault model by first prescribing a general pattern of slip distribution along the plate interface, then computing the slip at the center of each subfault using seismic moment as a constraint.

In plots I–V of figure 16, we show five slip distribution scenarios for M_w 7.5 earthquakes in the Shumagin seismic gap—the most sensitive region for Sand Point. In figure 16-VI we show a slip distribution for a larger event near Simeonof Island that satisfies the constraints of Witter and others (2014), discussed later in this report. Employing a method similar to Geist and Dmowska (1999) and Sobolev and others (2007), we use slip distribution formulas by Freund and Barnett (1976) to model our slip distributions. The distributions are color coded and some values of the slip (in meters) are shown in violet; depth contours of the plate interface model are in kilometers. The location of Sand Point is marked by a black rectangle topped with a flag. Note that the shapes of slip distribution for all five cases are similar, but the depth changes. This slip distribution of a larger earthquake can be approximated by a linear combination of these sources.

The most important parameters in the Freund and Barnett (1976) formulas are the upper and lower boundaries of the hypothetical rupture in the local downdip direction. Between any two consecutive cases, the hypothetical rupture is offset by about 10 km (6.2 mi) in the downdip direction. Case A corresponds to a rupture at 50 km (31 mi) depth, case B corresponds to a rupture at 40 km (25 mi) depth, up to case E at 10 km (6.2 mi) depth. The vertical deformation associated with each case is shown in figure 17. Blue shading indicates ground subsidence, while red shading marks areas of uplift.

While there are geologic/paleoseismologic constraints (that is, no coseismic vertical land-level changes greater than 0.3 m [1 ft]) on the modeled ground subsidence or uplift near Simeonof Island (Witter and others, 2014), we assume for this sensitivity study that all cases are geologically plausible for the western part of the Shumagin Islands. Later in this report we impose the above-mentioned constraint on the tsunami scenarios. Thus for each case, A–E, we model the tsunami propagation and record the simulated water-level dynamics near the waterfront in Sand Point. The simulated water level for each case is shown in figure 18. We observe that waves arriving at Sand Point are typically out of phase with each other, that is, crests and troughs arrive at Sand Point at the same time. Hence tsunamis initiated independently by each downdip section (cases A–E) can destructively interfere with each other and cause a mutual cancellation of the waves. However, some downdip sections generate waves, the crests of which could arrive almost at the same time and thus could constructively interfere with each other to produce a larger wave. Therefore, a combination of several cases might provide a foundation for the development of the maximum credible scenario. We hypothesize that in the time interval between 1.75 and 2 hours after the earthquake, marked by a purple-shaded rectangle in figure 18, the individual components (cases A–D) do not cancel, but constructively interfere with each other. To test this claim we examine the following optimization problem.

We consider an earthquake rupture scenario that is a linear combination of the five slip patterns A–E. The weight of the i-th slip pattern is denoted by αi. For each linear combination it is possible to model the coseismic ground displacement and then simulate the water dynamics in Sand Point. For the maximum possible combination that causes the most extensive flooding in Sand Point, the values of (αA, αB, … , αE) are unknown and must be calculated. One of the restrictions on the weights αk is that the slip of the weighted combination cannot exceed a certain limit—the assumed maximum coseismic slip. Using the geodetic data to invert the coseismic slip for the 1960 Chile earthquake, Moreno and others (2009) revealed large regions where the coseismic slip was more than 40 m (131 ft) on the Chilean subduction zone. In a recent publication, Butler (2014) considered several hypothetical events along the Alaska–Aleutian subduction zone with a 35 m (115 ft) displacement on the megathrust and up to a 50 m (164 ft) displacement near the trench. At the same time Nicolsky and others (2015) used a maximum slip of 37 m (121 ft) near the Fox Islands region. In a similar tsunami hazard assessment study for communities along the Cascadia subduction zone, Witter and others (2011) assumed 40-44 m (131–144 ft) of displacement on the plate interface. In this report we follow the previous findings and assume that the maximum coseismic slip is about 40 m (131 ft).

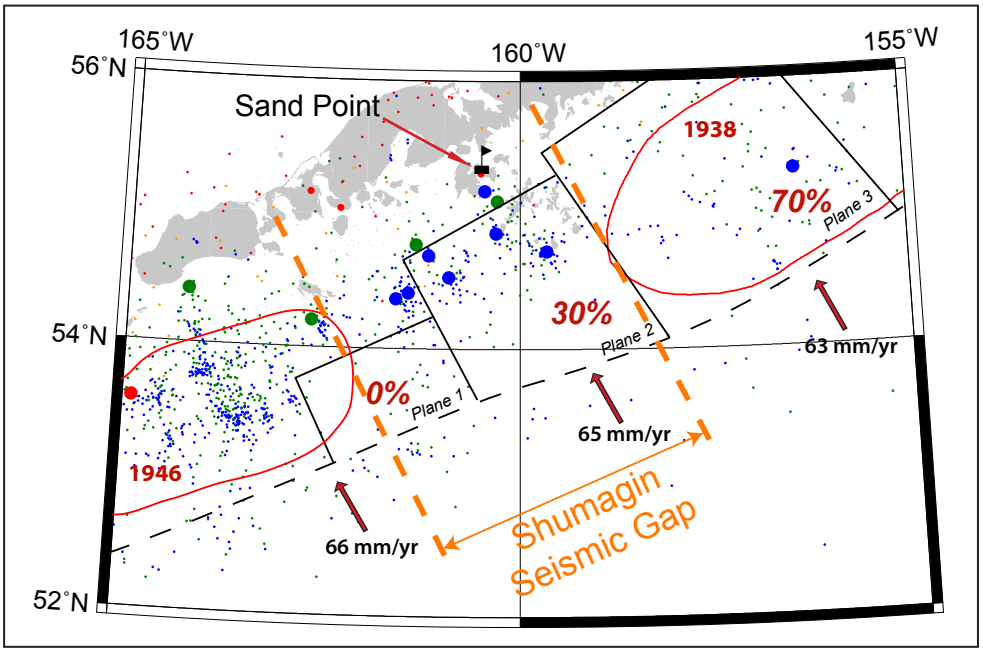

Figure 14. Earthquakes near the Shumagin Islands, from the Alaska Earthquake Center catalog. Small dots correspond to earthquakes of magnitude less than 5; large dots are related to earthquakes of magnitude 5 or greater. The trench is marked by the dashed black line. Black rectangles mark locations of the fault planes, for which the percent of unit coupling is estimated by Cross and Freymueller (2008). Depth to the top of each set of fault planes is 5 km (3.1 mi). Location of the Shumagin seismic gap is marked by dashed orange lines. Parts of the rupture patches associated with the 1946 and 1938 earthquakes are shown by red lines. Red arrows show annual movement of plates along the trench.

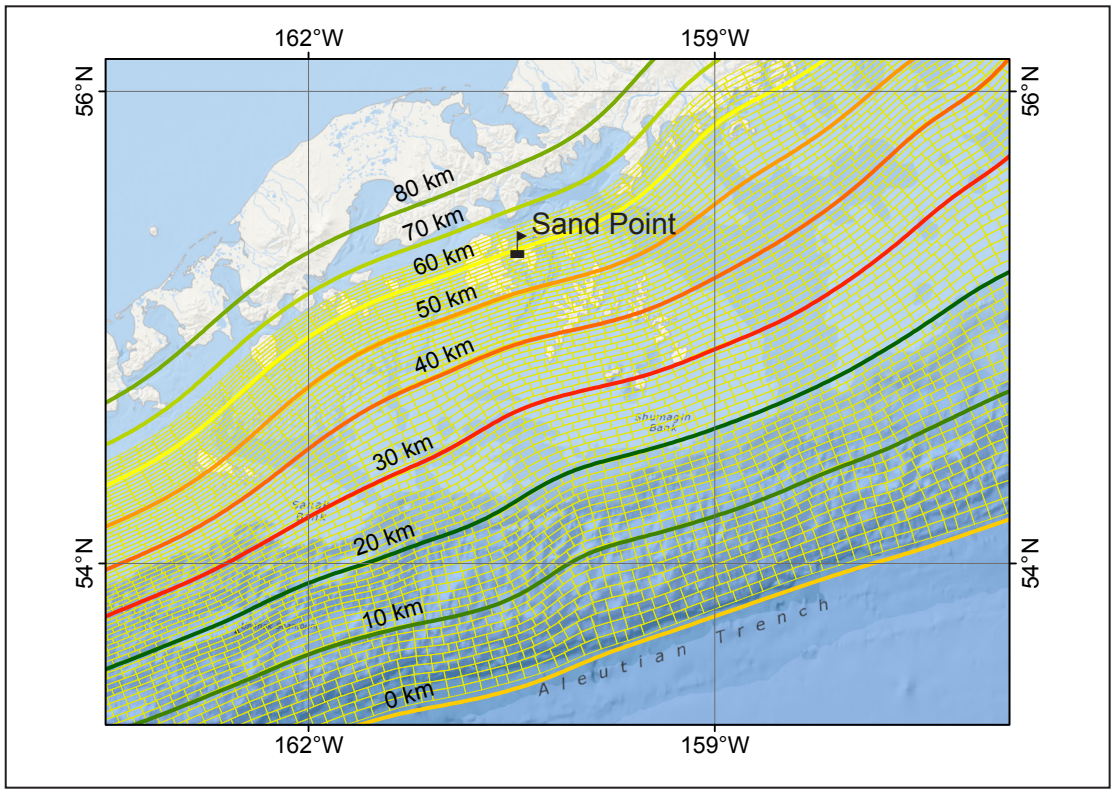

Figure 15. Discretization of the plate interface model into a set of rectangles used to compute the coseismic vertical displacement using formulas developed by Okada (1985). Colored lines mark depth contours (in kilometers) of the reconstructed plate interface.

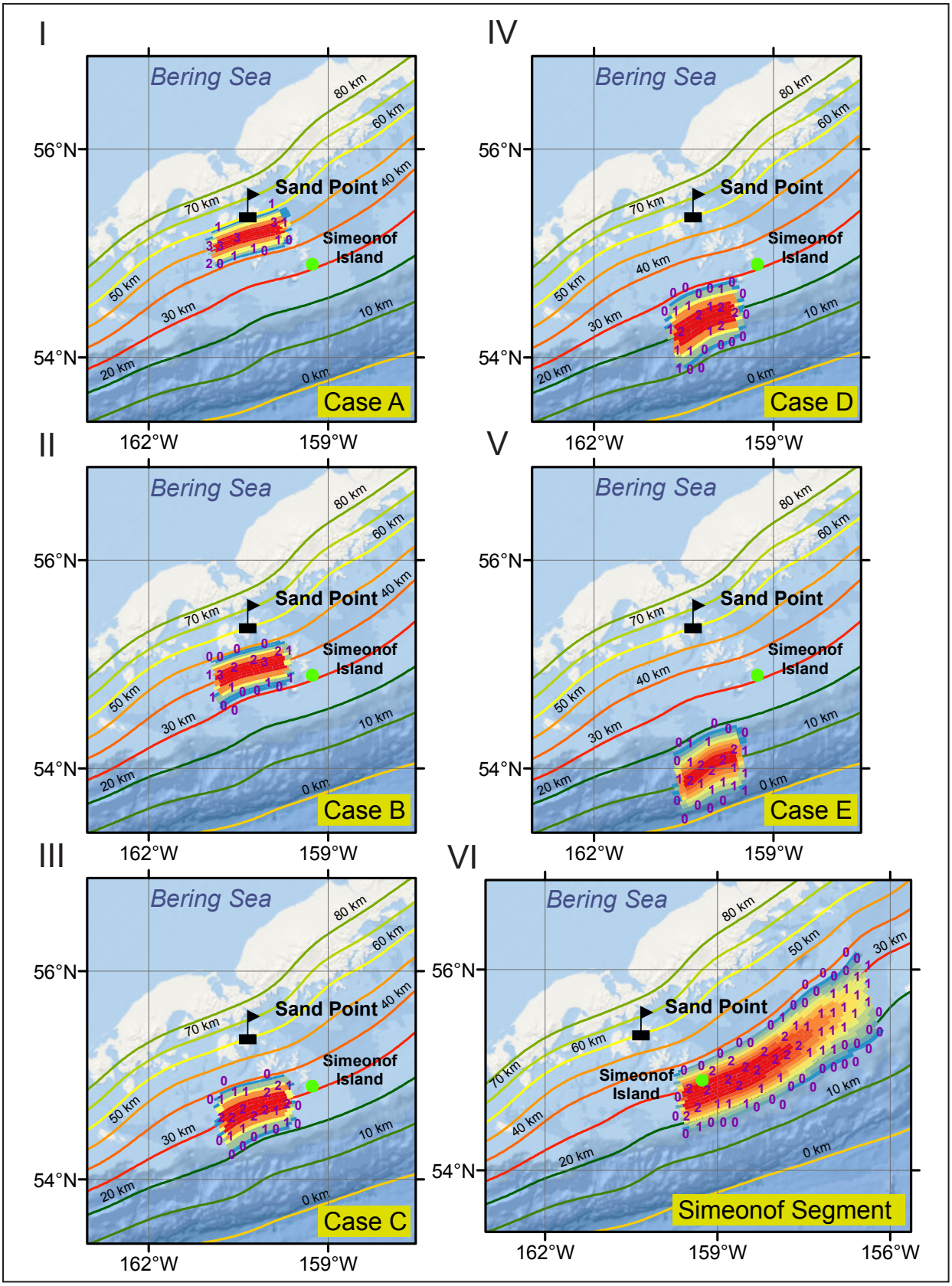

Figure 16. Assumed slip distribution along the plate interface for cases A through E (panels I–V, respectively), modeling a M_w 7.5 rupture near the Shumagin Islands. Slip location varies in the downdip direction of the plate interface while preserving the same patch configuration in the along-strike direction. Panel VI shows slip distribution for the Simeonof Island segment; updip and downdip boundaries are selected such that Simeonof Island is located at the point of near-zero coseismic deformation. The parameterization of slip in the along-dip direction is based on the analytical approximation by Freund and Barnett (1976). Colored lines show depth contours (in kilometers).

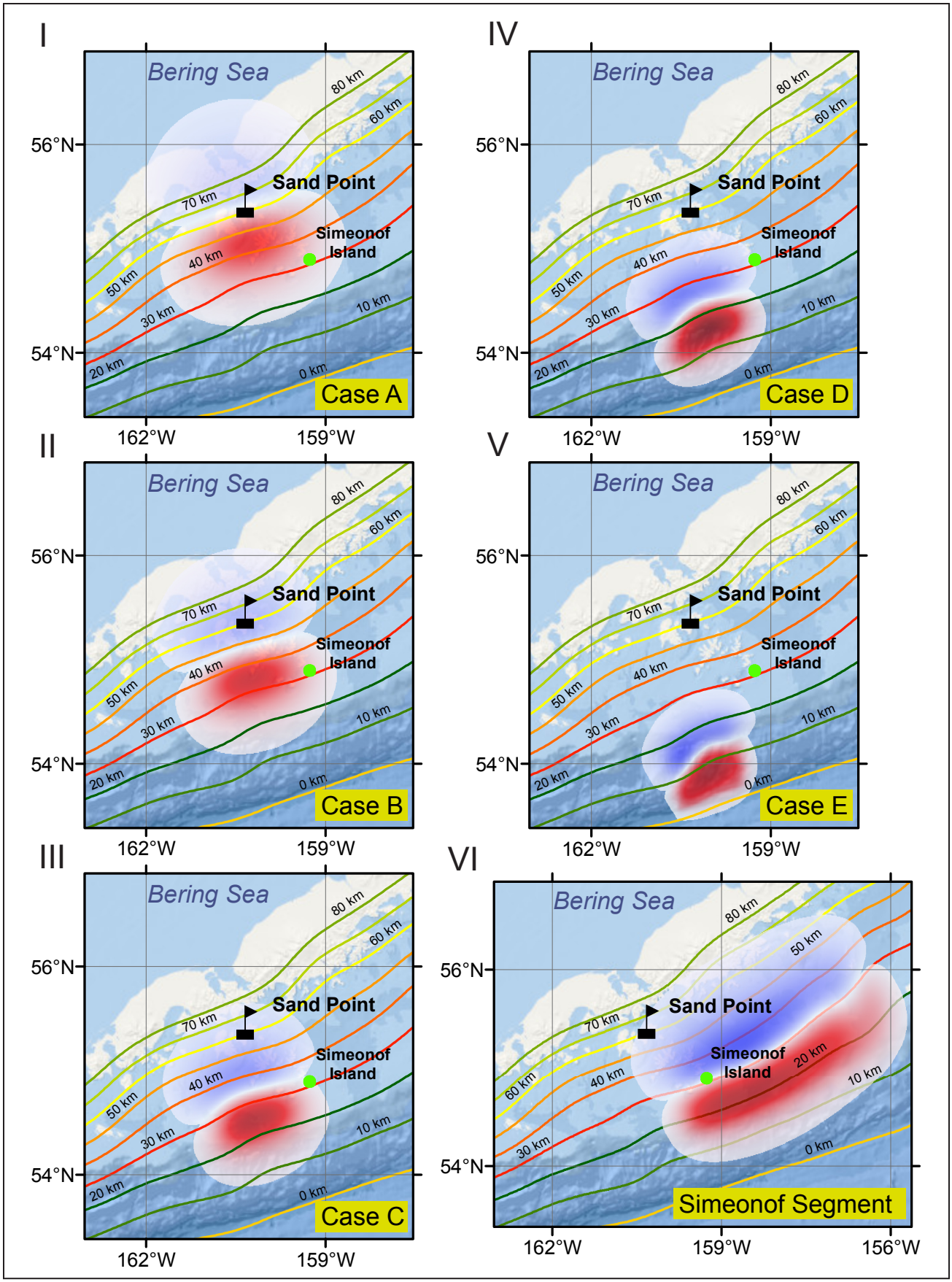

Figure 17. Computed vertical ground surface deformation related to cases A through E (panels I–V, respectively). Vertical deformation for the Simeonof segment is shown in panel VI. Coseismic ground subsidence is indicated by blue shading; areas of uplift are shown in red.

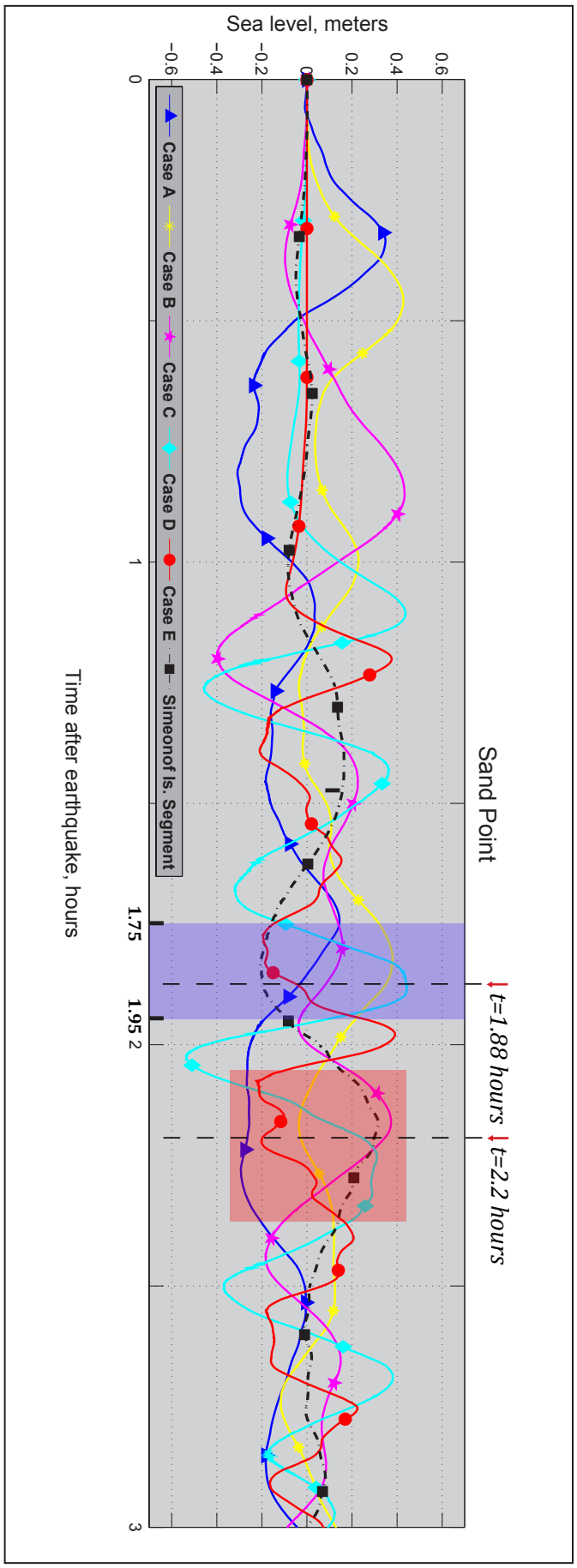

Figure 18. Modeled water-level dynamics in Sand Point for six ground-surface deformations related to cases A–E and the Simeonof segment as shown in figure 17. The purple-shaded area indicates the time period when waves in cases A–D arrive in phase with each other and may constructively interfere with each other; the red-shaded area shows the same for cases C, D, and the Simeonof Island segment.

Obtaining an exact solution to this optimization problem requires finding a ground surface deformation for numerous combinations of weights (αA, αB, … , αE), and then solving non-linear shallow-water equations for each deformation. Therefore, a conclusion of the sensitivity study is that maximization of the slip related to cases B, C, and D, 40 m (131 ft), results in the maximum wave in Sand Point, and hence a combination of cases B, C, and D may constitute a basis for the development of credible tsunami scenarios.

We find an approximate solution to the optimization problem. Because the harbor is connected to the deep ocean by channels 15–20 m (49–66 ft) deep, we assume that nonlinear effects in the tsunami propagation from its source to the Sand Point harbor are rather small. Second we assume the ground surface deformation linearly depends on the slip. Therefore, for a hypothetical rupture specified by (αA, αB, … , αE), the ground surface deformation is the linear combination of vertical deformations, shown in figure 18, with the same weights (αA, αB, … , αE). Consequently, the water-level dynamics in Sand Point can be represented by a linear combination of the time series related to cases A–E, where a time series for the k-th case is weighted by αk. The time series for all cases are shown in figure 18. A maximum value of the combination of these time series represents the highest wave that can arrive at Sand Point according to the choice of (αA, αB, … , αE).

Thus, from the mathematical point of view, we need to find a set of (αA, αB, … , αE) for which the linear combination of the time series is maximum, while assuming that the maximum slip of the weighted combination is limited, for example, by 40 m (131 ft). While the optimization problem is already greatly simplified, one of the obstacles to obtaining a solution is the existence of multiple local maxima. A maximum of the function (in our case, the maximum value of the linear combination of time series) is called local if a function attains its maximum in a small neighborhood (in our case, near a certain combination of weights), but a larger value of the function might be lying somewhere else. The difficulty, therefore, is that a solution found to solve the optimization problem might be a local maximum, whereas the global maximum might be related to another combination(s) of (αA, αB, … , αE). To address this, we start the optimization algorithm from multiple random combinations of weights. Figure 19 illustrates several typical outputs/solutions of the optimization algorithm, such as a linear combination of the time series that results in the maximum water level in Sand Point. We emphasize that each panel in figure 19 depicts a local solution to the optimization problem. The weights (αA, αB, … , αE) at which the local maximum is attained are listed in the gray rectangle. The maximum slip (MaxSlipk) at the k-th slip pattern, corresponding to the weight αk, is also listed in the gray rectangle. According to the results in panels I, II, III, IV, and V in figure 19 the maximum wave in Sand Point may be between 10 and 15 m (33–49 ft). We emphasize that these are preliminary results that: (a) do not take into account, for example, geologic constraints on Simeonof Island, and (b) are obtained under the assumption of linear water wave propagation.

Further analysis of the obtained results in panels I–V reveals that MaxSlipB, MaxSlipC, and MaxSlipD—the maximum slip for the slip patterns related to cases B, C, and D—is equal to its maximum allowed value of 40 m (131 ft) and that the maximum wave arrives about 1.8 to 1.9 hours after the earthquake. The red arrow indicates the time when the maximum wave arrives at Sand Point. Similarly, we note that according to results displayed in panel IV, the maximum wave arrives about 1.88 hours after the earthquake, and that MaxSlipB and MaxSlipD likewise attain the maximum allowed value. At the same time, weights αA and αE, as well as the corresponding MaxSlipA and MaxSlipB, vary significantly across all outputs/solutions. An explanation to the wide range of αA and αE is that about 1.75 to 1.95 hours after the earthquake the water-level dynamics related to cases A and E are near zero or even negative (see plots at the purple rectangle in figure 18). The only moment of time when case E might significantly contribute to the maximum wave is between 1.95 and 2 hours, but this potential contribution is weakened by case D showing a strong negative signal at the same time. Therefore, the contributions of cases A and E to the maximum wave height are not significant compared to the corresponding contributions of cases B and D. Moreover, by comparing the water levels related to cases A and C in figure 18, we observe that the water level related to case C stays positive between 1.75 and 1.95 hours after the earthquake while the one related to case A is almost zero. We consequently infer that the contribution of case C to the optimization results is greater than that of case A.

Paleoseismic Constraints

One of the major findings in the paleoseismic study by Witter and others (2014) is that there are no sudden coseismic vertical land-level changes greater than 0.3 m (1 ft) produced by great earthquakes at Simeonof Island over the past 3,400 years. Witter and others (2014) also documented the lack of marine strand lines and terraces, as well as uniform Holocene soil development at all elevations, providing additional support for the lack of long-term uplift. Thus, large land level changes due to earthquakes might not have occurred on Simeonof Island since deglaciation in the latest Pleistocene. One interpretation of their results would be that if a great earthquake has occurred in this region, the island must have been near the hingeline—a line of no vertical change separating the uplift and subsidence zones. Surface displacements for each case and the island location are shown in figure 17. For cases A and B the island lies in the uplift region of the ground surface deformation, whereas the displacement at Simeonof for cases C, D, and E is small. Because we are focused on development of M_w 8.5–9.2 earthquake scenarios (while exploiting a combination of cases B, C, and D as the basis), some scenarios may contradict the available geologic records if the vertical displacement for the scenario is significant near Simeonof Island. Therefore, one needs to ensure a near zero displacement at the island while developing credible scenarios.

We propose to model a slip distribution in direct proximity to Simeonof Island to be able to align the island with the

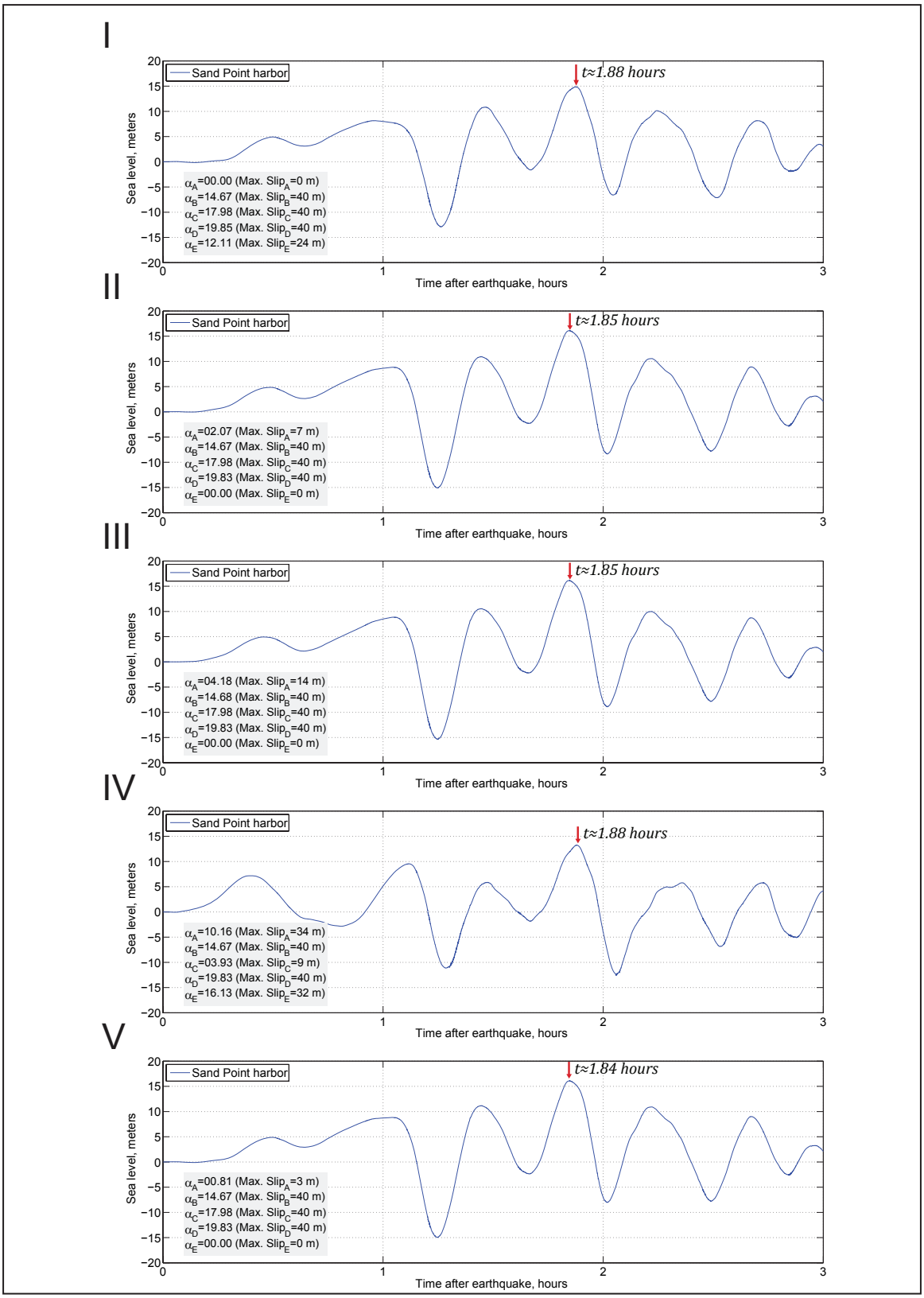

Figure 19. Results of the optimization algorithm that maximizes the linear combination of water dynamics related to cases A–E. Panels I–V show the optimized water-level dynamics in Sand Point for various starting combinations of weights (αA, αB, … , αE). The optimization algorithm finishes when a local maximum is attained. The resultant values of αA, αB, … , αE, which are associated with the derived local maximum, along with the related maximum value of slip (Max. Slip) for each slip pattern, are listed in the gray rectangle. The red arrow indicates the time when the maximum is achieved.

hingeline. The proposed slip distribution and the associated ground deformation are shown in figures 16-VI and 17-VI, respectively. We refer to this additional possible rupture as the Simeonof segment. As we did earlier, we use slip distribution formulas by Freund and Barnett (1976) to model its slip distribution. The slip for the Simeonof segment is chosen such that its maximum slip is about the same as the slip for segments related to cases A–E. The modeled water-level dynamics in Sand Point related to a hypothetical rupture of the Simeonof segment are shown in figure 18 by a black dash-dotted line. Note that in the interval between 1.45 and 2 hours after the earthquake, marked in figure 18 by a blue rectangle, the water level related to the Simeonof segment is out of phase with the water-level dynamics related to case B, C, and D. Consequently, results of the above sensitivity study must be adjusted.

We therefore consider an additional optimization problem, in which the Simeonof segment is added to the linear combination of the five cases, A–E. In this optimization problem the weights (αA, αB, …, αE) defining the slip for cases A–E can vary arbitrarily, whereas the weight of the Simeonof segment relative to the potential rupture is fixed such that its maximum slip is 35 m (115 ft), which is close to the maximum considered slip in this report. We now seek a solution that maximizes the linear combination of the time series (representing the water-level dynamics in Sand Point), both for the five cases and for the Simeonof segment. We similarly constrain the maximum slip for cases A–E to 40 m (131 ft).

Typical results of the optimization problem for various starting points are shown in figure 20. The set of derived optimal weights (αA, αB, … , αE) along with the maximum slip for the related slip patterns are listed in gray rectangles. According to plots I, III, and IV, the maximum wave arrives about 2.2 hours after the earthquake. Note that the computed water level related to case B is near zero around 2.2 hours after the earthquake (compare plots inside the red rectangle in fig. 18), and thus the contribution of case B is insignificant in comparison to cases C and D. Moreover, case B produces a somewhat noticeable uplift near Simeonof Island if its slip pattern is included in the hypothetical scenario with a considerable weight. We also note that the optimization algorithm typically weights case A near zero, except for the last outcome/solution of the optimization algorithm, as shown in panel V (fig. 20). According to the latter, a wave may arrive at Sand Point in less than an hour; however, its maximum height is smaller compared to the other plotted outcomes. Additionally, this combination of slip patterns also results in a significant uplift of Simeonof Island and may not be directly employed to construct maximum credible scenarios (because according to Witter and others [2014] there are no sudden coseismic vertical land-level changes greater than 0.3 m [1 ft] produced by great earthquakes at Simeonof Island over the past 3,400 years). We also note that the optimization algorithm for case E results in a weight of zero as well, since its contribution to the water level around 2 to 2.2 hours is negative (see the red line in fig. 18).

We finally conclude that if we include the Simeonof segment in the optimization algorithm, then the maximum wave in Sand Point is derived by maximizing the slip of cases C and D to the maximum allowed value of 40 m (131 ft), as shown in plots I, III, and IV. Hence a rupture of the combination of cases C and D, as well as the Simeonof segment, might produce a reasonable approximation of the maximum credible scenario, which does not cause a noticeable vertical deformation at Simeonof Island. Inclusion of case B might produce some uplift, but its magnitude would be within the uncertainty level of Witter and others (2014). We construct maximum credible scenario for Sand Point as follows.

Scenario 1. M_w 8.8 earthquake in the Shumagin Island region, based on hypothetical cases C and D and the Simeonof segment

This event considers a M_w 8.8 earthquake that ruptures the Aleutian megathrust with maximum slip in the Shumagin seismic gap region between the 1938 and 1946 rupture zones. The slip is distributed between 10 and 40 km (6.2–24.9 mi) depth across the Shumagin Islands archipelago, and between 17 and 28 km (10.6–17.4 mi) depth east of the archipelago. The maximum 37–38 m (121.4–124.7 ft) slip is between 20 and 30 km (12.4–18.6 mi) depth along the archipelago. The proposed slip distribution is shown in figure 21-I; vertical coseismic deformations for this scenario are shown in figure 22-I.

Although the above sensitivity study implies that scenario 1 might result in the maximum wave height in Sand Point, we assume some important simplifications that could reduce the accuracy of the sensitivity study. We assume that the nonlinear effects in the water dynamics can be omitted. Therefore, to ensure that we do not unintentionally omit other relevant scenarios, we supplement scenario 1 with similar scenarios 2 through 6. Table 2 lists all considered variations of maximum credible scenarios in this study.

Scenario 2. M_w 8.85 earthquake in the Shumagin Island region, based on hypothetical cases B, C, and D, and the Simeonof segment

This event is a hypothetical M_w 8.85 earthquake that ruptures the Aleutian megathrust, with maximum slip in the Shumagin seismic gap region between the 1938 and 1946 rupture zones. The slip is distributed between 10 and 50 km (6.2–31.1 mi) depth of the plate interface across the Shumagin Islands archipelago, and between 17 and 28 km (10.6–17.4 mi) depth east of the archipelago. The maximum 37–38 m (121.4–124.7 ft) slip is between 20 and 40 km (12.4–24.9 mi) depth along the archipelago. The proposed slip distribution is shown in figure 21-II; vertical coseismic deformations for this scenario are shown in figure 22-II.

Scenario 3. M_W 8.85 earthquake in the Shumagin Islands region, based on hypothetical cases C, D, and E, and the Simeonof segment

This event is a hypothetical M_W 8.85 earthquake that ruptures the Aleutian megathrust, with maximum slip in the Shumagin seismic gap region between the 1938 and 1946 rupture zones. The slip is distributed between 7 and 40 km (4.3–24.9 mi) depth of the plate interface across the Shumagin Islands archipelago, and between 17 and 28 km (10.6–17.4 mi) depth east of the archipelago. The maximum 37–38 m (121.4–124.7 ft) slip is between 10 and 30 km (6.2–18.6 mi) depth along the archipelago. The proposed slip distribution is shown in figure 21-III; vertical coseismic deformations for this scenario are shown in figure 22-III.

Scenario 4. M_W 8.9 earthquake in the Shumagin Island region, based on hypothetical cases B, C, D, and E, and the Simeonof segment

This event is a hypothetical M_W 8.9 earthquake that ruptures the Aleutian megathrust, with maximum slip in the Shumagin seismic gap region between the 1938 and 1946 rupture zones. The slip is distributed between 7 and 50 km (4.3–31.1 mi) depth of the plate interface across the Shumagin Islands archipelago, and between 17 and 28 km (10.6–17.4 mi) depth east of the archipelago. The maximum 37–38 m (121.4–124.7 ft) slip is between 10 and 40 km (6.2–24.9 mi) depth along the archipelago. The proposed slip distribution is shown in figure 21-IV; vertical coseismic deformations for this scenario are shown in figure 22-IV.

In view of the recent M_W 9.0 earthquake off the Pacific coast of Tohoku in 2011, we considered similar events along the Aleutian megathrust (David Scholl, USGS, oral commun., 2013). During the Tohoku earthquake a large amount of slip occurred between the subducting and overriding plates near the Japan trench (Fujii and others, 2011; Shao and others, 2011).

Scenario 5. M_W 8.9 earthquake in the Shumagin Island region, based on hypothetical cases C, D, and E, as well as the Simeonof segment and a near-Trench segment from Shumagin Islands to Sanak Island

This event is a hypothetical M_W 8.85 earthquake that ruptures the Aleutian megathrust with maximum slip in the Shumagin seismic gap region between the 1938 and 1946 rupture zones. The slip is distributed between 7 and 40 km |(4.3–24.9 mi) depth of the plate interface across the Shumagin Islands archipelago, between 17 and 28 km (10.6–17.4 mi) depth east of the archipelago, and between 7 and 20 km (4.3–12.4 mi) depth along the Aleutian trench between the archipelago and Sanak Island. The maximum 37–38 m (121.4–124.7 ft) slip is between 10 and 30 km (6.2–18.6 mi) depth along the archipelago, and the slip along the trench is assumed to be about 30 m (98 ft). The proposed slip distribution is shown in figure 21-V; vertical coseismic deformations for this scenario are shown in figure 22-V.

Scenario 6. M_W 8.95 earthquake in the Shumagin Island region, based on hypothetical cases B, C, D, and E, as well as the Simeonof segment and a near-Trench segment from Shumagin Islands to Sanak Island

This event is a hypothetical M_W 8.95 earthquake that ruptures the Aleutian megathrust, with maximum slip in the Shumagin seismic gap region between the 1938 and 1946 rupture zones. The slip is distributed between 7 and 50 km (4.3–31.1 mi) depth of the plate interface across the Shumagin Islands archipelago, between 17 and 28 km (10.6–17.4 mi) depth east of the archipelago, and between 7 and 20 km (4.3–12.4 mi) depth along the Aleutian trench between the archipelago and Sanak Island. The maximum 37–38 m (121.4–124.7 ft) slip is between 10 and 40 km (6.2–24.9 mi) depth along the archipelago, and the slip along the trench is assumed to be about 30 m (98 ft). The proposed slip distribution is shown in figure 21-VI; vertical coseismic deformations for this scenario are shown in figure 22-VI.

The USGS Science Application for Risk Reduction (SAFRR) project, in collaboration with NOAA and State of California agencies, has developed a plausible hypothetical tsunami scenario (Kirby and others, 2013) to describe the impacts of a tsunami generated by an earthquake in the Alaska Peninsula region (Ross and others, 2013).

Scenario 7. The M_W 9.0 earthquake according to the SAFRR project

The USGS Tsunami Source Working Group defined the scenario source as a M 9.0 earthquake similar to the Tohoku 2011 event, but between the Shumagin Islands and Kodiak Island. The rupture area, represented by 56 subfaults, is about 350 x 200 km (217.5 x 124.3 mi), with an average slip of 15.7 m (51.51 ft) and a maximum slip of 75 m (246.1 ft). Larger values of slip are located near the trench as for the Tohoku earthquake. The coseismic deformations for this scenario are shown in figure 23-I.

Paleoseismic records in the Pacific Northwest region of the western U.S. reveal that great tsunamigenic earthquakes occur repeatedly in the Cascadia subduction zone over irregular intervals averaging about 500 years (Atwater, 1987), and are often accompanied by tsunamis. The latest trans-Pacific tsunami generated by an earthquake at Cascadia occurred in January 1700 (Satake and others, 1996; Atwater and others, 2005). The impact of this tsunami on Alaska coastal communities was not documented, likely because of low population density along the Alaska coast at that time. Multiple models of Cascadia subduction zone ruptures are suggested by Satake and others (2003) and Priest and others (2009) and in references therein. These models describe hypothetical coseismic displacement fields with various levels of detail. A Cascadia subduction zone earthquake is considered to be a medium-field tsunami source to the southeastern Alaska coast, thus a relatively simple “worst case but credible” rupture of the Cascadia subduction zone is used in this report.

Scenario 8. Rupture of the Cascadia zone, including the entire megathrust between British Columbia and northern California

Wang and others (2003) concluded that the downdip limit of the rupture in the 1700 Cascadia earthquake couldn't be constrained using the tsunami heights in Japanese historical records. The authors suggested a conservative approach for Cascadia coseismic deformations assuming that full coseismic rupture takes place over the entire locked zone and the slip decreases linearly downdip halfway into the present effective transition zone. The most recently updated and probably more reasonable model assumes that the slip distribution in the downdip direction is bell-shaped (Witter and others, 2011), which is different from what was used to model the coseismic deformation shown in Wang and others (2003; figure 14). In this report, the assumed M_w 9 rupture recovers 1,200 years of plate convergence with about 36 m (118.1 ft) of maximum slip (Witter and others, 2011). The vertical coseismic displacement for this scenario is shown in figure 23-II.

Outer-rise earthquakes are known to occur in the subducting plate in the vicinity of the oceanic trench and can be subdivided into two groups: tensional (normal) and compressional (thrust) events (Stauder, 1968b; Byrne and others, 1988). Great tensional outer-rise events occurred near Japan on March 2, 1933 (the M_w 8.4 Sanriku-oki earthquake [Kanamori, 1971]) and near Indonesia on August 19, 1977 (the M_w 8.3 Sumba earthquake [Gusman and others, 2009]). At least 24 significant outer-rise events have occurred along the Aleutian–Alaska Arc (Christensen and Ruff, 1988).

Great outer-rise earthquakes such as the March 2, 1933, Sanriku, M_w 8.4 event (Kanamori, 1971) and the March 30, 1965, Rat Islands Ms 7.5 event (Abe, 1972) are thought to be capable of rupturing through the entire oceanic lithosphere in response to the pull of the downdipping slab. As a result of this massive type of rupture, the Sanriku-oki and Sumba earthquakes each generated a significant tsunami that culminated in at least 3,000 deaths in Japan and 189 deaths in Indonesia (NGDC, 2013). The recent comparable 2009 M_w 8.0 Samoa event also generated a significant tsunami that propagated throughout the Pacific Ocean.

Table 2. All hypothetical tectonic scenarios used to model tsunami runup in Sand Point

	Tectonic Scenarios	Depth range (km)	Maximum slip depth range (km)	Maximum slip (m)	Maximum subsidence (m)	Maximum uplift (m)	Vertical displacement (m)
1	M_w 8.8 earthquake based on cases C, D, and the Simeonof segment	12–38 km	18–34 km	37–38 m	-5.13 m	14.6 m	-1.54 m
2	M_w 8.85 earthquake based on cases B, C, D, and the Simeonof segment	12–48 km	18–44 km	37–38 m	-5.13 m	15.1 m	-3.15 m
3	M_w 8.85 earthquake based on cases C, D, E, and the Simeonof segment	6–38 km	10–34 km	37–38 m	-5.14 m	17.4 m	-1.51 m
4	M_w 8.9 earthquake based on cases B, C, D, E, and the Simeonof segment	6–48 km	10–44 km	37–38 m	-5.23 m	17.8 m	-3.18 m
5	M_w 8.9 earthquake based on cases C, D, E, the Simeonof segment, and the near-Trench segment	6–38 km	10–34 km	37–38 m	-5.15 m	17.2 m	-1.51m
6	M_w 8.95 earthquake based on cases B, C, D, E, the Simeonof Segment, and the near-Trench segment	6–48 km	10–44 km	37–38 m	-5.34 m	17.9 m	-3.24 m
7	M_w 9.0 earthquake according to the SAFRR project	8–54 km	11–14 km	55–65 m	2.8 m	14.8 m	-0.16 m
8	M_w 9.0–9.1 earthquake in the Cascadia subduction zone	Wang and others (2003)	Wang and others (2003)	35–40 m	7.5 m	10.9 m	0.0 m
9	M_w 8.6 outer rise earthquake in the Shumagin Islands region	2–23 km	2–23 km	25 m	-14.3 m	2.5 m	-0.06 m

Table 3. Fault parameters for the hypothetical tensional outer-rise scenario

Latitude (°N)	Longitude (°W)	Depth	Length	Width	Strike	Dip	Rake	Slip
54°19'51.6"	155°19'04.8"	2 km	100 km	15 km	248.26°	45°	-90°	25 m
53°59'06.0"	156°44'52.8"	2 km	100 km	15 km	250.75°	45°	-90°	25 m
53°40'48.0"	158°11'06.0"	2 km	100 km	15 km	255.17°	45°	-90°	25 m
53°26'16.8"	159°38'52.8"	2 km	100 km	15 km	254.12°	45°	-90°	25 m
53°10'44.4"	161°05'09.6"	2 km	100 km	15 km	247.42°	45°	-90°	25 m

Table 4. Longitude and latitude locations of the time series points in Sand Point. The pre-earthquake onshore (S) and offshore (O) locations are specified in the third column. The maximum water level above ground is provided for onshore locations, whereas the maximum water level above the pre-earthquake MHHW is provided for offshore locations. The minimum elevation above the post-earthquake MHHW datum is provided for the onshore locations, while the minimum post-earthquake depth is provided for the offshore locations.

#	Label	S / O	Longitude (°W)	Latitude (°N)	Minimum Elevation/ Depth (m)	Maximum Water Level Above Ground/Sea Level (m)									Maximum Water Velocity (m/sec)								
						Scenario									Scenario								
						1	2	3	4	5	6	7	8	9	1	2	3	4	5	6	7	8	9
1	East Head	O	160.49028	55.35917	13.5	7.4	7.3	8.7	8.0	8.8	8.0	1.2	0.9	1.3	2.4	1.6	2.2	1.6	2.1	1.9	0.7	0.4	0.5
2	Mud Bay	O	160.49750	55.34806	0.2	11.5	8.4	12.3	9.4	12.3	9.8	2.0	1.3	2.5	5.7	3.8	7.1	4.1	6.9	4.4	1.9	1.3	2.7
3	Range Island	O	160.50694	55.35389	4.7	8.7	8.0	10.4	8.9	10.7	8.7	1.6	1.0	2.4	9.0	9.9	9.3	10.1	8.8	10.5	4.7	3.3	3.9
4	Unga Reef	O	160.52694	55.33972	5.9	10.4	10.7	10.2	11.0	10.3	11.4	2.0	1.4	1.7	9.1	8.3	9.1	8.7	9.1	8.8	3.3	3.0	3.5
5	Popof Reef	O	160.51444	55.33917	11.6	10.9	11.3	10.5	11.3	10.8	11.6	2.0	1.5	1.9	8.8	9.6	8.4	9.5	9.0	9.6	3.3	2.2	2.7
6	Karpa St.	S	160.49528	55.34639	9.4	0.0	0.0	0.9	0.0	1.2	0.0	0.0	0.0	0.0	0.0	0.0	5.3	0.0	5.3	0.0	0.0	0.0	0.0
7	End of Russian Church Rd.	S	160.50111	55.34417	4.0	4.0	4.2	3.8	4.4	4.1	4.1	0.0	0.0	0.0	3.5	3.1	4.0	3.5	3.8	3.8	0.0	0.0	0.0
8	End of Peters Rd.	S	160.50139	55.33917	4.6	3.6	3.6	3.2	3.9	3.5	3.8	0.0	0.0	0.0	5.3	2.7	11.6	6.9	10.0	6.0	0.0	0.0	0.0
9	Trident Dock	O	160.50167	55.33500	8.6	12.0	12.6	12.0	12.9	12.3	13.1	2.2	1.6	1.9	6.8	2.5	7.5	2.7	7.2	2.9	0.8	0.8	0.8
10	Trident Plant	S	160.49972	55.33556	-0.5	9.3	9.8	9.6	10.1	9.8	10.4	0.0	0.0	0.0	7.0	8.2	9.2	6.8	10.3	6.8	0.0	0.0	0.0
11	Sand Point Ave.	S	160.49778	55.33639	-1.7	10.8	11.1	11.3	11.4	11.4	11.8	0.5	0.0	0.0	4.1	3.1	3.8	3.5	4.0	3.5	0.5	0.0	0.0
12	Sand Point Ave., bridge	S	160.49639	55.33611	-2.8	11.9	12.2	12.4	12.6	12.6	12.9	1.5	0.7	0.9	6.0	5.2	6.5	6.0	6.2	5.9	2.5	2.3	2.7
13	The Lagoon	O	160.49528	55.33833	1.6	13.8	12.9	13.8	13.2	14.3	13.8	2.3	1.3	1.3	8.7	7.8	8.7	8.1	7.9	8.0	0.9	0.7	1.2
14	Harbor Access Rd.	S	160.49472	55.33750	-2.3	12.3	11.8	12.5	12.2	12.8	12.6	1.1	0.2	0.2	7.2	5.9	7.0	6.8	6.9	6.7	0.8	0.0	0.0
15	Small Boat Harbor Storage	S	160.49528	55.33639	-2.3	11.6	11.7	12.1	12.1	12.3	12.4	1.1	0.2	0.2	5.9	5.6	6.1	5.8	5.6	5.7	1.9	0.0	0.0
16	Harbor Facilities	S	160.49639	55.33528	-1.9	10.8	11.2	11.3	11.6	11.5	11.8	0.5	0.1	0.0	4.8	4.8	6.0	5.5	6.0	5.3	1.5	0.0	0.0
17	Small Boat Harbor	O	160.49833	55.33361	13.2	12.2	12.6	12.3	12.9	12.5	13.2	2.2	1.6	1.5	1.9	1.5	1.7	1.7	1.8	1.6	0.3	0.2	0.5
18	Boat Harbor Rd.	S	160.49528	55.33278	2.6	6.4	6.7	6.5	7.1	6.8	7.4	0.0	0.0	0.0	2.3	4.0	2.3	10.8	3.4	13.6	0.0	0.0	0.0
19	New Boat Harbor	O	160.50306	55.33056	7.5	12.1	12.6	11.7	12.9	11.8	12.9	2.2	1.6	1.6	1.9	1.5	2.7	1.5	2.1	1.4	0.6	0.4	1.1
20	New Boat Harbor Storage	S	160.50194	55.32944	-1.2	9.9	10.4	9.6	10.8	9.6	10.7	0.0	0.0	0.0	3.2	5.2	2.1	3.1	1.7	2.8	0.0	0.0	0.0
21	Sand Point Rd.	S	160.52139	55.31833	-1.9	9.1	10.3	9.1	10.3	9.6	10.6	0.8	0.0	0.0	5.6	5.6	6.9	6.0	6.4	7.1	1.7	0.0	0.0
22	Airport Facilities	S	160.51861	55.31944	-1.5	8.9	9.8	8.9	9.9	9.4	10.2	0.4	0.0	0.0	5.1	3.1	5.6	3.9	5.0	3.8	1.0	0.0	0.0
23	Airport Docks	O	160.51944	55.32167	17.0	10.9	11.5	10.8	11.5	11.0	11.8	2.3	1.5	1.5	5.7	4.3	5.0	3.5	5.1	3.5	0.8	0.7	0.8
24	Airport Runway, north	S	160.52722	55.31917	0.6	6.6	6.5	6.5	6.5	6.2	6.7	0.0	0.0	0.0	6.8	8.4	6.8	8.6	7.1	8.6	0.0	0.0	0.0
25	Airport Runway, middle	S	160.52111	55.31333	1.2	5.8	6.5	5.7	6.6	5.7	6.9	0.0	0.0	0.0	7.1	6.8	8.5	9.4	5.8	7.5	0.0	0.0	0.0
26	Aiport Runway, south	S	160.51556	55.30806	2.0	4.3	5.4	3.9	5.1	4.1	5.3	0.0	0.0	0.0	4.5	4.0	4.1	4.3	3.5	4.6	0.0	0.0	0.0
27	Popof Strait	O	160.53111	55.29861	60.3	9.8	11.2	9.6	11.1	9.5	11.4	2.2	1.2	0.9	2.5	2.5	2.7	2.9	2.5	2.8	0.4	0.4	0.5
28	Humboldt Harbor	O	160.51472	55.33083	18.2	11.1	12.3	11.0	12.2	10.9	12.4	2.1	1.5	1.5	8.2	5.6	8.0	5.4	7.5	5.5	1.3	1.2	1.2
29	Egg Island	O	160.50972	55.27694	40.9	8.5	10.3	8.9	10.8	9.0	11.2	1.9	1.1	0.8	4.0	3.8	3.8	4.0	3.2	3.6	0.6	0.4	0.5
30	Northern Shore	O	160.47083	55.35778	3.2	6.0	7.1	6.9	7.8	6.8	8.0	1.4	0.9	1.0	4.5	3.3	4.8	3.4	4.6	3.2	0.8	0.5	1.1

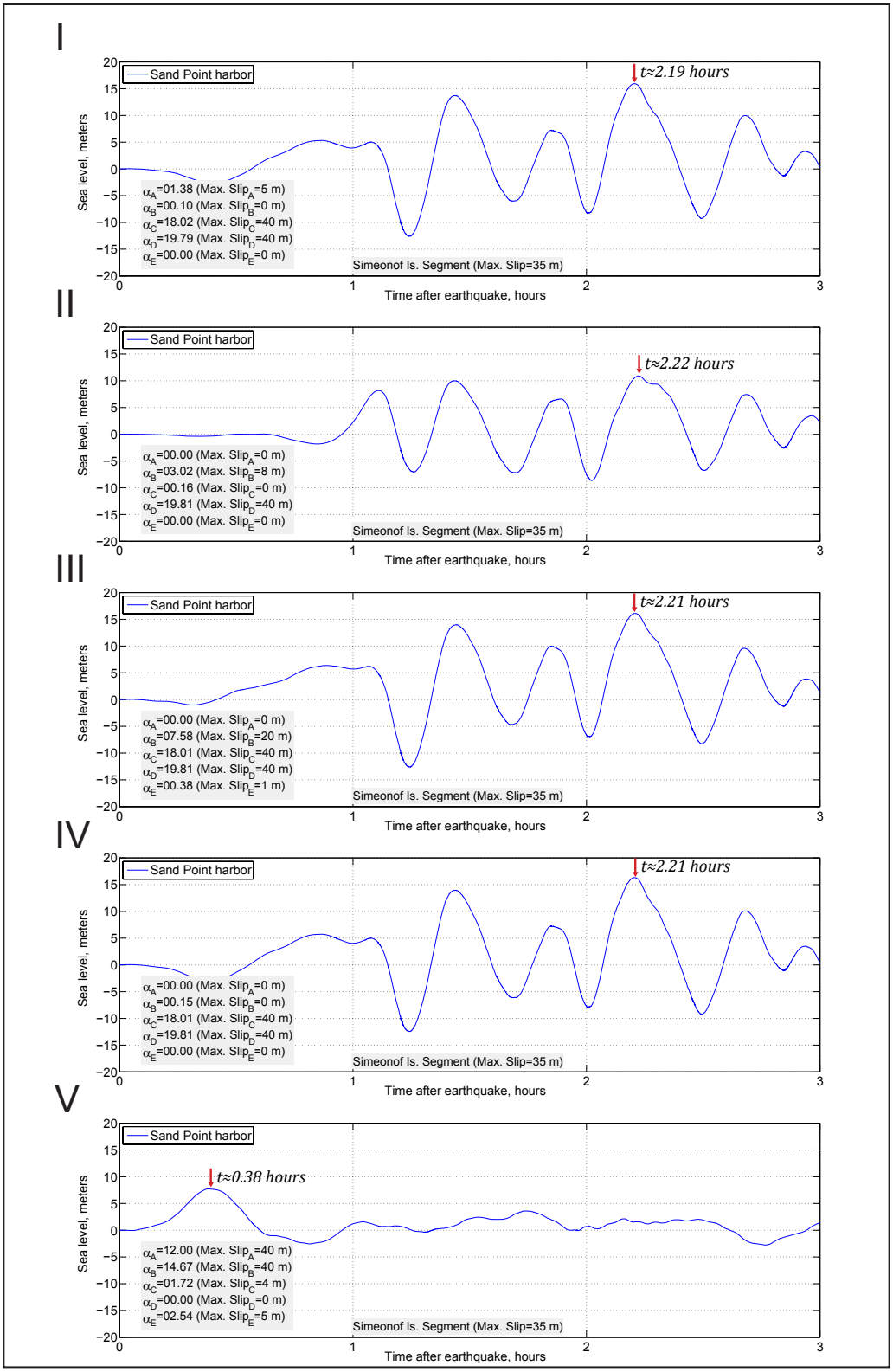

Figure 20. Results of the optimization algorithm that maximizes the linear combination of water dynamics related to cases A–E and to the Simeonof segment. The weights (αA, αB, … , αE) associated with cases A–E are allowed to vary, while the contribution of the Simeonof segment is fixed such that the maximum slip at the Simeonof segment is equal to 35 m (114.8 ft). Panels I–V show the optimized water-level dynamics in Sand Point for various starting combinations of weights (αA, αB, … , αE). The optimization algorithm finishes when a local maximum is attained. The resultant values of αA, αB, … , αE, which are associated with the derived local maximum, along with the related maximum value of slip (Max. Slip) for each slip pattern are recorded in the gray rectangle. The red arrow indicates time when the maximum is achieved.

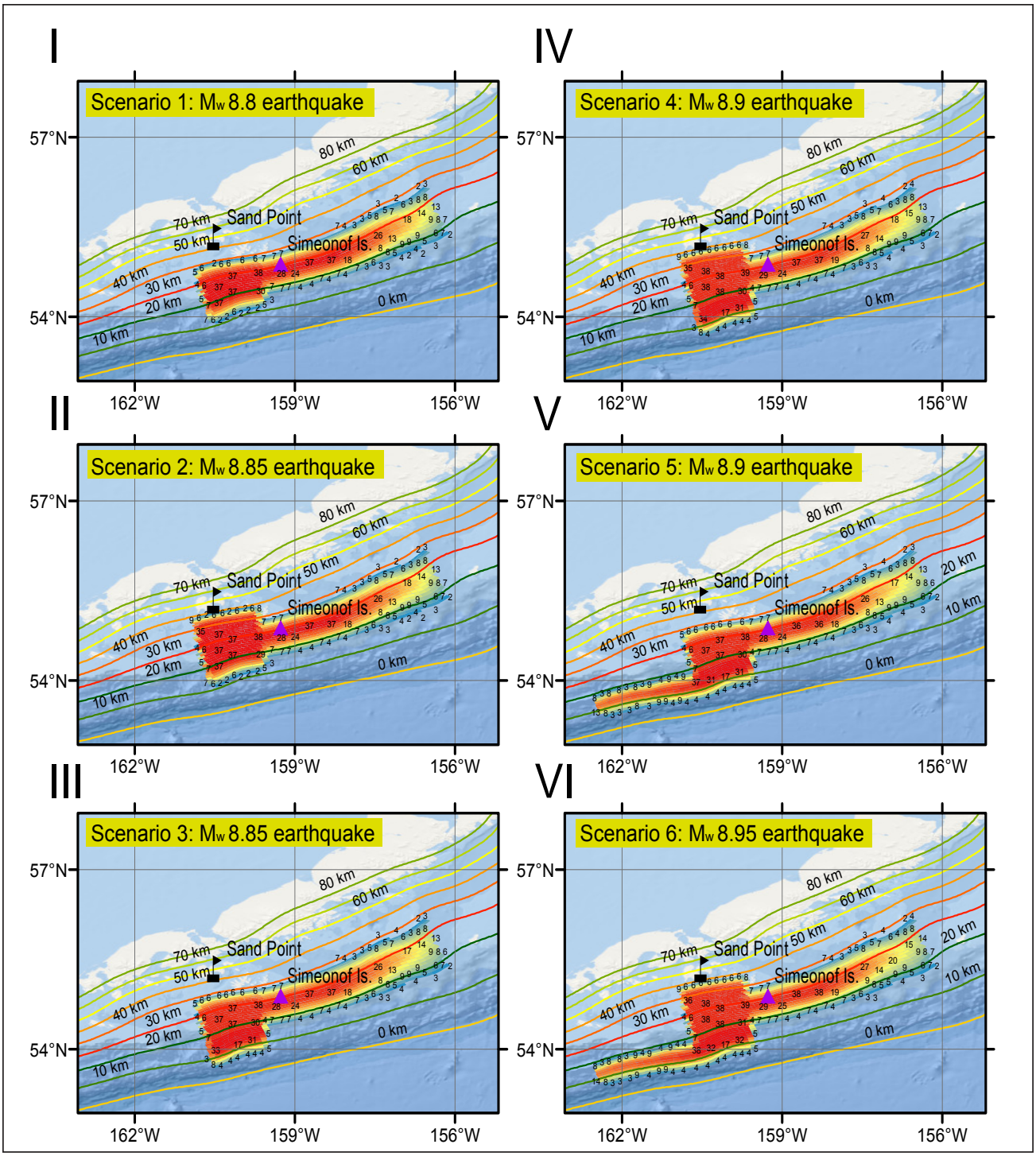

Figure 21. Proposed slip distribution along the plate interface for hypothetical M_w 8.8–8.95 earthquakes related to scenarios 1–6. Slip values (in meters) are labeled with small black numbers. Depth contours (in kilometers) of the Aleutian interface are shown by colored lines.

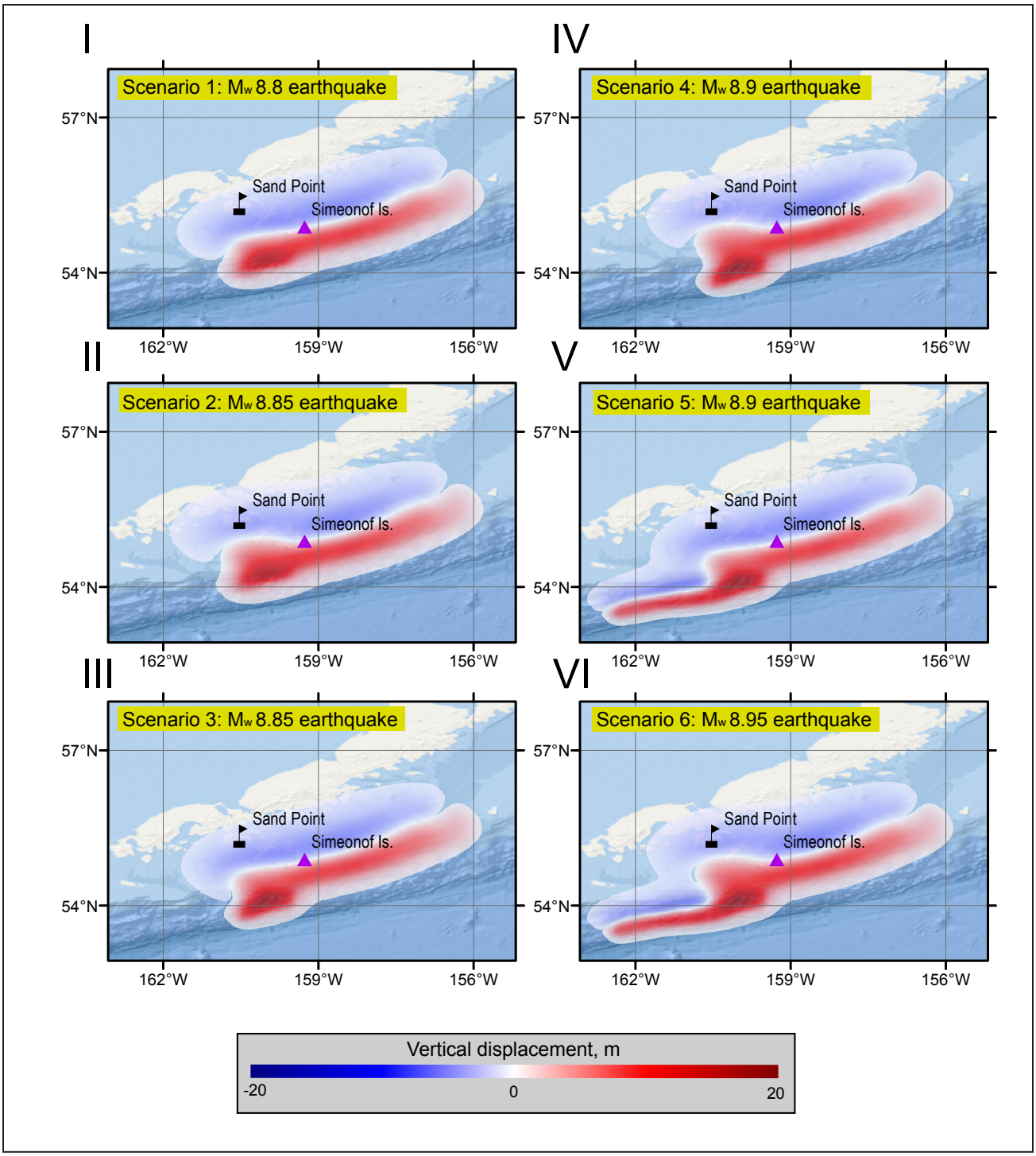

Figure 22. Computed vertical ground surface deformation related to the proposed slip distributions shown in figure 21. Coseismic ground subsidence is indicated by blue shading; areas of uplift are shown in red.

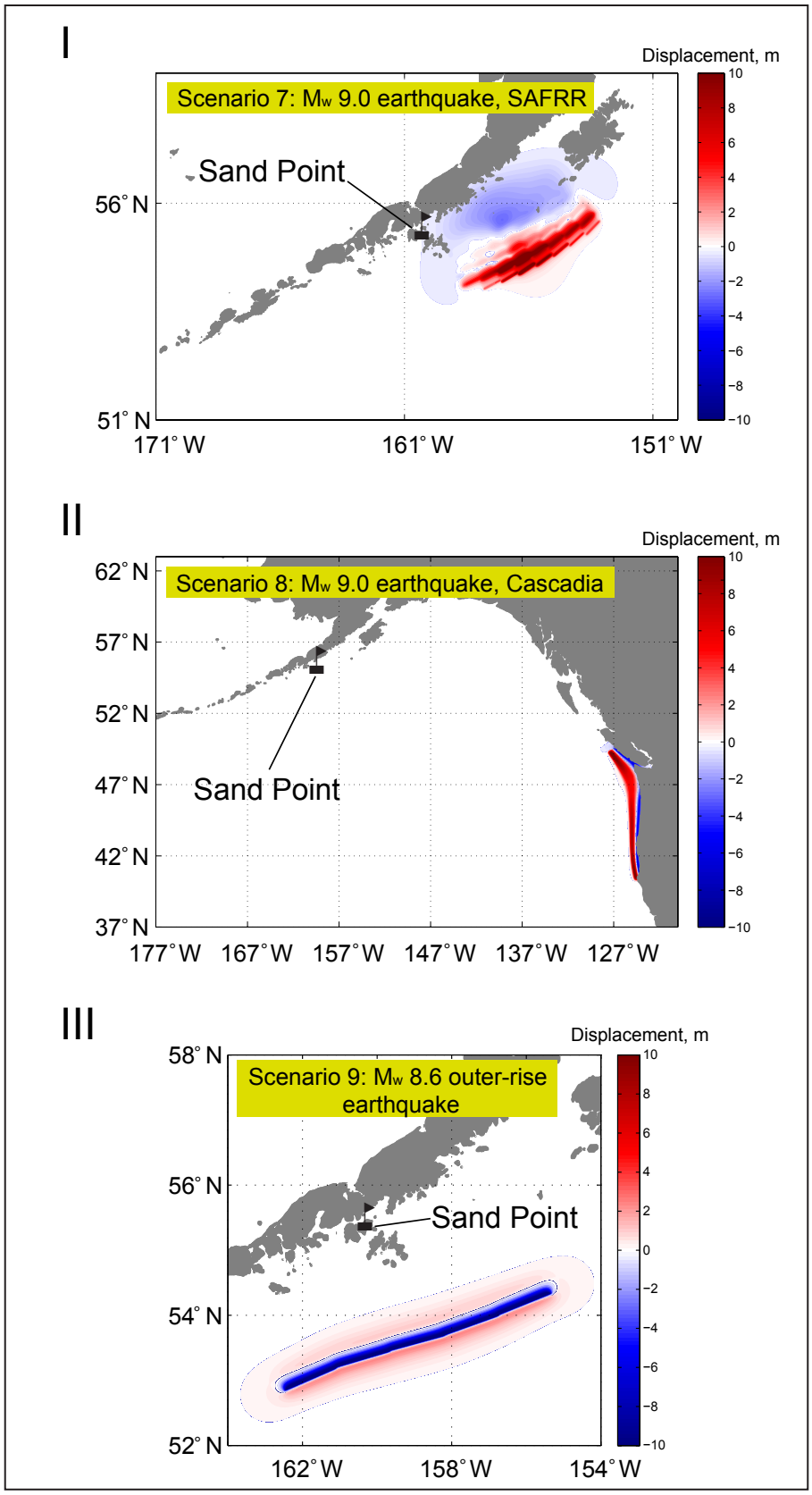

Figure 23. Computed vertical ground surface deformation related to (I) the M_w 9.0 hypothetical SAFRR project earthquake, (II) the M_w 9.0 hypothetical earthquake in the Cascadia region, and (III) the M_w 8.6 outer-rise earthquake along the Shumagin Islands. Coseismic ground subsidence is indicated by blue shading; areas of uplift are shown in red.

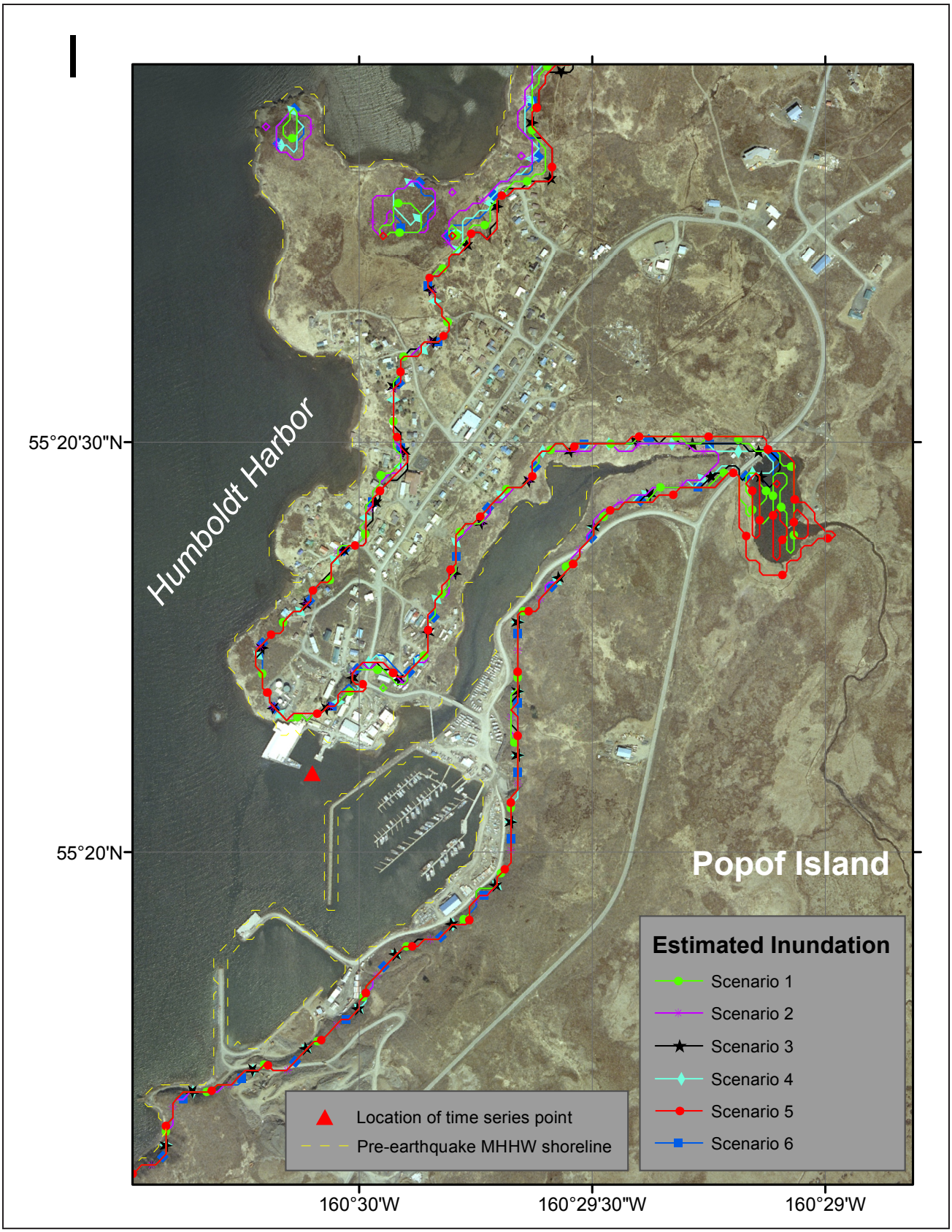

Figure 24. Modeled potential inundation near the Sand Point harbor for (I) scenarios 1–6. The DEM corresponds to the present-day MHHW datum. Due to the steep topography, inundation areas for several tsunami scenarios share a common boundary, and the plotted extents of the inundation areas may overlie each other. Maximum estimated inundation from all scenarios is shown by the bold red line. The location with the recorded water level dynamics in Humboldt Harbor is marked by a red triangle in panels I and II.

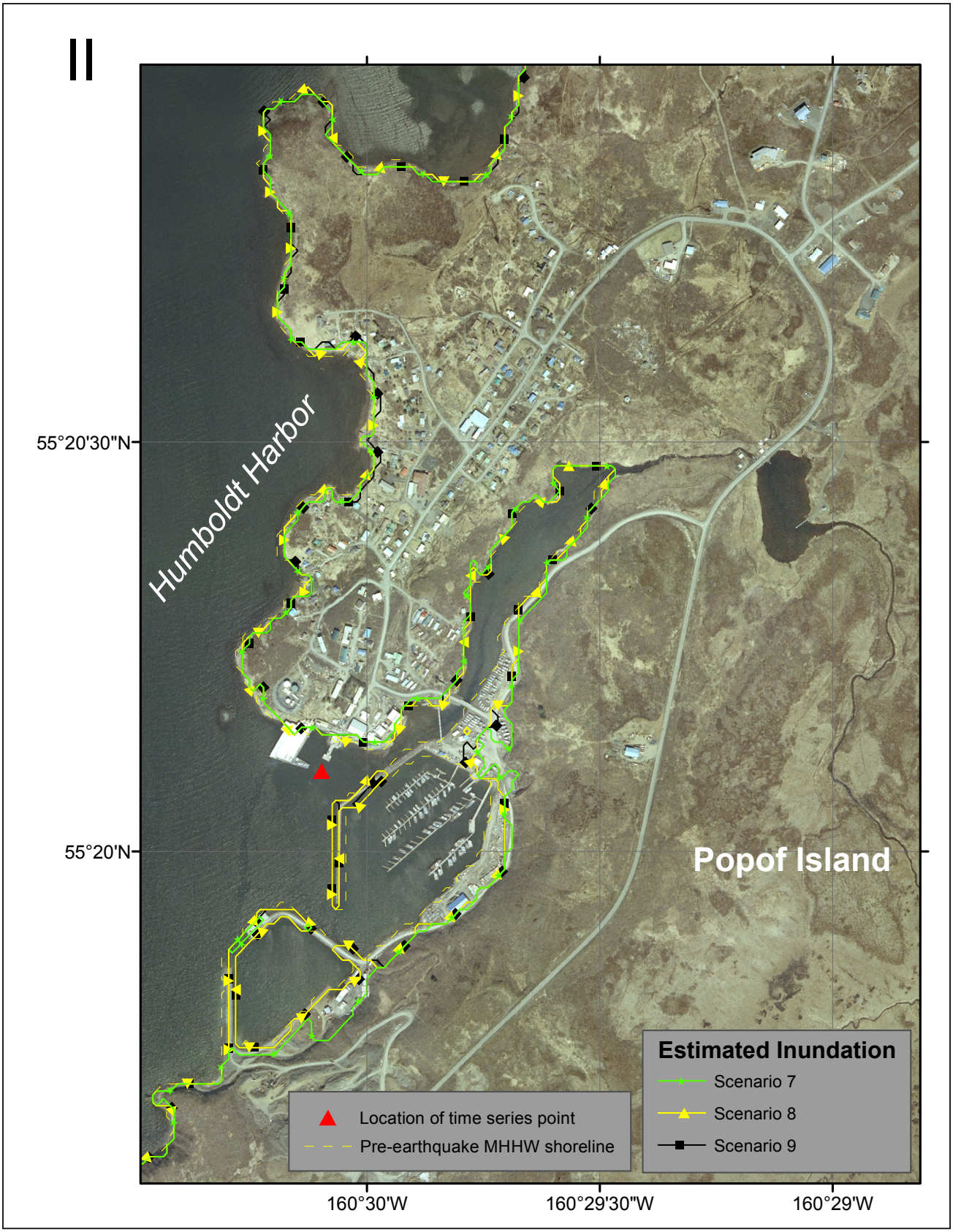

Figure 24, continued. Modeled potential inundation near the Sand Point harbor for (II) scenarios 7–9. The DEM corresponds to the present-day MHHW datum. Due to the steep topography, inundation areas for several tsunami scenarios share a common boundary, and the plotted extents of the inundation areas may overlie each other. Maximum estimated inundation from all scenarios is shown by the bold red line. The location with the recorded water level dynamics in Humboldt Harbor is marked by a red triangle in panels I and II.

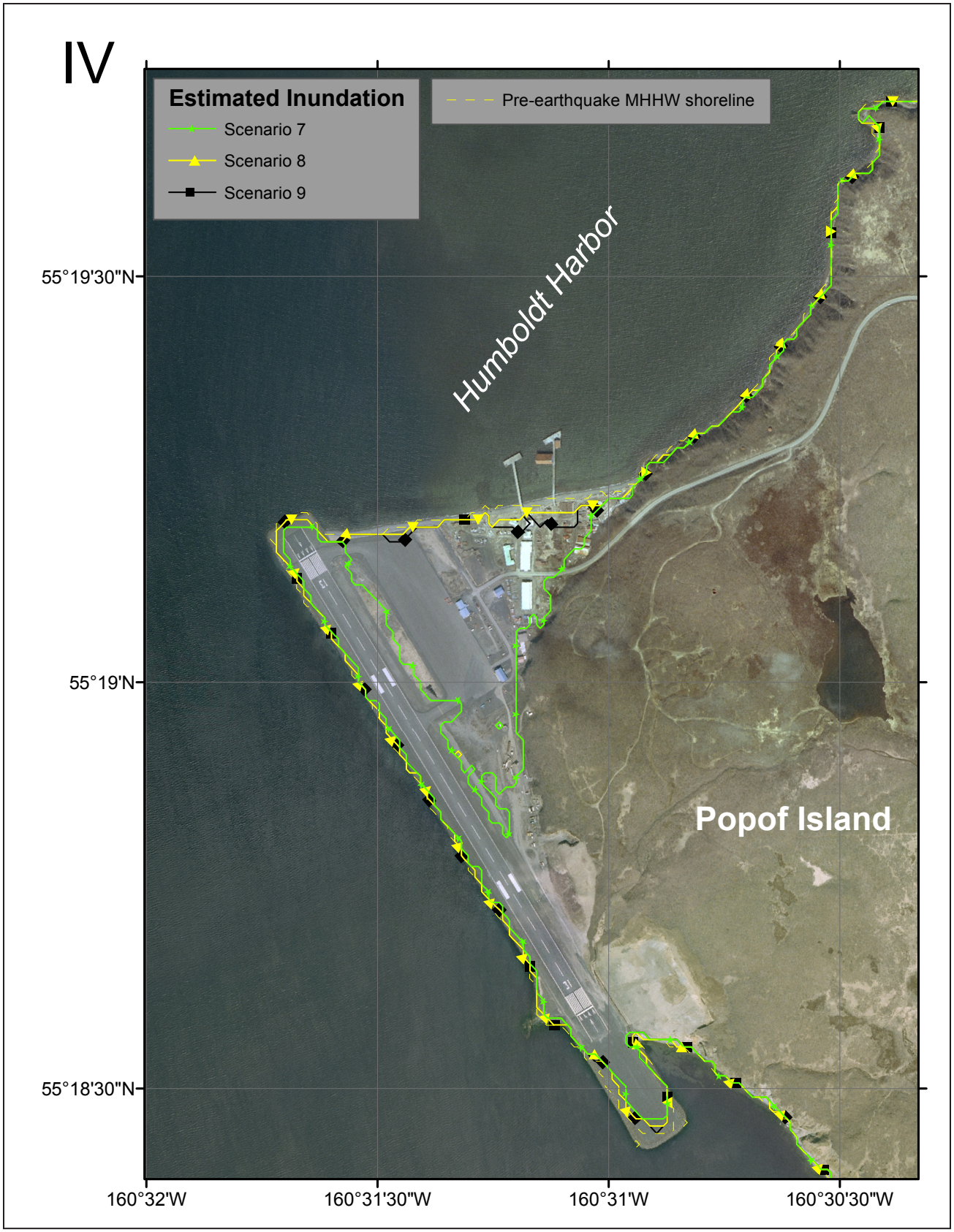

Figure 24, continued. Modeled potential inundation around the Sand Point airport for (IV) scenarios 7–9. The DEM corresponds to the present-day MHHW datum. Due to the steep topography, inundation areas for several tsunami scenarios share a common boundary, and the plotted extents of the inundation areas may overlie each other. Maximum estimated inundation from all scenarios is shown by the bold red line. The location with the recorded water level dynamics in Humboldt Harbor is marked by a red triangle in panels I and II..

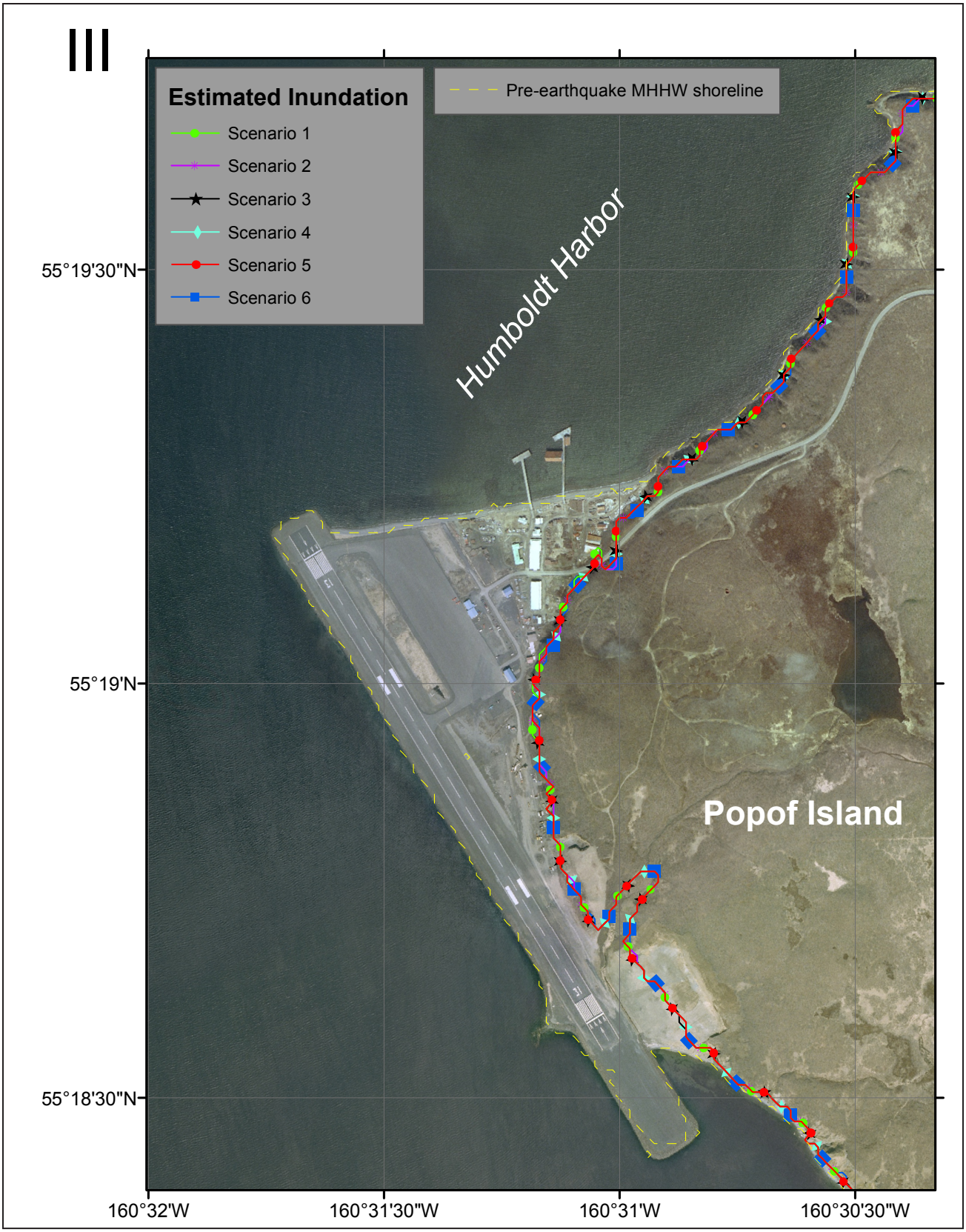

Figure 24, continued. Modeled potential inundation around the Sand Point airport for (III) scenarios 1–6. The DEM corresponds to the present-day MHHW datum. Due to the steep topography, inundation areas for several tsunami scenarios share a common boundary, and the plotted extents of the inundation areas may overlie each other. Maximum estimated inundation from all scenarios is shown by the bold red line. The location with the recorded water level dynamics in Humboldt Harbor is marked by a red triangle in panels I and II..

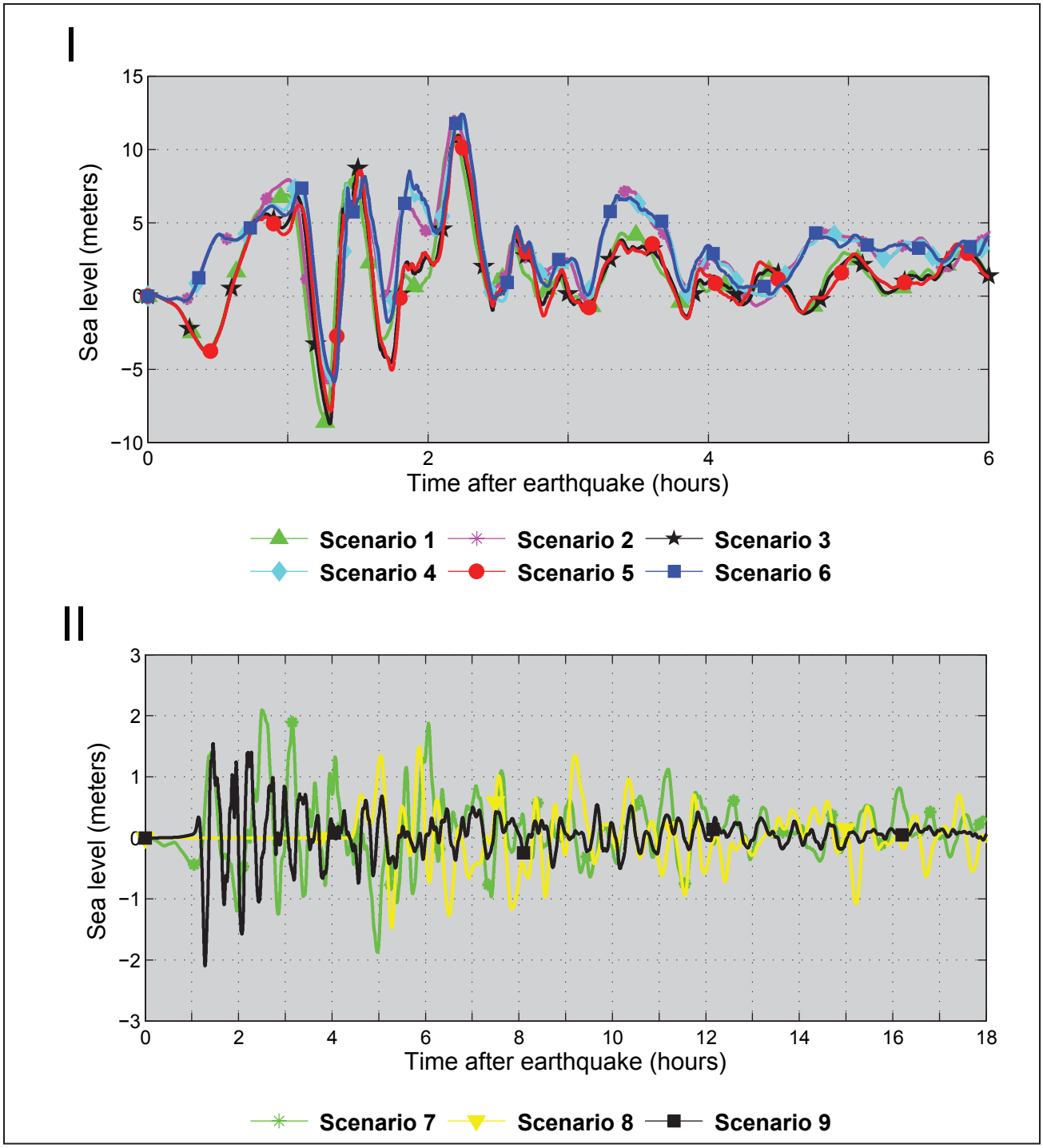

Figure 25. Time series of water level near the Sand Point harbor for (I) scenarios 1–6 and (II) scenarios 7–9. The vertical datum is selected such that zero corresponds to the pre-earthquake sea level.

Scenario 9. Rupture of the tensional outer-rise part of the subduction plate south of the trench in the Shumagin Islands area

We consider a hypothetical outer-rise event parallel to the Shumagin Islands and parameterize it with five subfaults, listed in table 3. The fault parameters required to compute seafloor deformation are the epicenter location, area, dip, rake, strike, and amount of slip on the fault. We use the equations of Okada (1985) to calculate distribution of coseismic uplift and subsidence resulting from this slip distribution. The dip of each subfault is in a range reported by Stauder (1968a) and we assume that the hypothetical earthquake ruptures through the entire slab. Vertical coseismic deformations for this scenario are shown in figure 23-III.

MODELING RESULTS

We performed numerical calculations for all nine scenarios listed in table 2. The water-level dynamics are modeled in each grid (table 1), but the extent of inundatio is only computed in the high-resolution grid. The simulated extents of inundation in the Sand Point harbor and airport area for all considered scenarios are shown in figure 24-I, 24-II, 24-III, and 24-IV. The maximum water level and velocity for all considered scenarios are listed in table 4.

We begin discussion of our modeling results by noting that scenario 1 (a hypothetical M_w 8.8 earthquake based on the combination of cases C and D) predicts an 11 m (36 ft) wave in Humboldt Harbor (fig. 25-I). The station location in the bay is marked by the red triangle in figures 24-I and 24-II. The numerical simulations also predict that the highest wave might arrive shortly more than 2 hours after the earthquake, preceded by some notable sea-level oscillations. We emphasize that the numerical results according to scenario 1 agree with the above-mentioned optimization outcomes shown in figures 20-I, 20-II, and 20-III. However, the wave height according to scenario 1 is smaller than the wave heights predicted by the optimization outcomes. One reason for this difference is that the maximum slip in scenario 1 is 37 m (121.4 ft), whereas the maximum slip in the optimization experiments was assumed to be 40 m (131.2 ft).

Similar modeling results were obtained for scenarios 2–4, where the maximum wave arrives at Humboldt Harbor shortly more than 2 hours after the earthquake and its height is about 11–13 m (36–43 ft) (fig. 25-I). The slightly higher wave, compared to scenario 1, is probably due to the inclusion of slip patterns associated with cases B and E in the earthquake scenario. Cases B and E do not significantly increase the wave height shortly more than 2 hours after the earthquake (see plots in red rectangle, fig. 18).

Scenarios 5 and 6 result in similar waves, about 11–13 m (36–43 ft) in height, that also arrive about 2 hours after the earthquake (fig. 25-I). Scenarios 5 and 6 simulate hypothetical earthquakes similar to scenarios 3 and 4, but also include a rupture of the near-trench segment. Addition of the near-trench segment does not produce a significant increase in the modeled tsunami height, probably because waves generated near the trench in the Shumagin seismic gap dissipate before arriving at Sand Point.

In scenario 7, a M_w 9.0 earthquake between Shumagin Islands and Kodiak Island produces a 2 m (6.6 ft) wave in Humboldt Harbor (fig. 25-II) that significantly inundates the harbor area. Scenarios 8 and 9, which model a rupture of the Cascadia subduction zone and an outer-rise event along the Shumagin Islands, respectively, result in 1.5 m (4.9 ft) waves in Humboldt Harbor (fig. 25-II) and flood only low-lying areas along the shoreline. Similarly, estimated flow depths related to each of the considered scenarios are shown in figures 26-I and 26-II.

Finally, we conclude that from the emergency management perspective in nearly all scenarios (fig. 25-I) waves arriving in the 1 to 1.5 hour timeframe are nearly as large as waves within the 2 hour timeframe and should be responded to just as seriously. The evacuation threshold is thus less than one hour, after which the waves continues to increase in magnitude for another hour and a half.

TIME SERIES AND OTHER NUMERICAL RESULTS

To help emergency managers assess the tsunami hazard in Sand Point we supplement the inundation map with the time series of the modeled water-level and velocity dynamics at certain locations around the community. The locations are identified by numbers in figure A-1. Detailed maps of the Sand Point harbor and Sand Point airport area with community location numbers are shown as figures A-2a and A-2b, respectively. For each numbered locality, we plot the sea level and water velocity predicted from scenarios 1–6 in figure A-3 and from scenarios 7–9 in figure A-4. Zero time corresponds to the time that the earthquake occurs. Elevations of onshore locations correspond to the post-earthquake MHHW datum. To show the height of arriving tsunamis for offshore locations, we use a vertical datum where zero corresponds to the pre-earthquake sea level (pre-EQ MHHW). Dashed lines show water levels after the tsunami. Velocity magnitude is calculated as water flux divided by water depth; thus the velocity value can have large uncertainties when the water depth is small. In the plots provided, the velocity is computed only where the water depth is greater than 0.3 m (1 ft).

Analysis of the time series plot shows that a hypothetical local M_w 8.8–8.95 earthquake (scenarios 1, 5, and 6) can create a wave that penetrates deep into the interior of the city of Sand Point and floods beyond a bridge on Sand Point Avenue (fig. 26-I). Uncertainties in the digital elevation model (DEM) at the head of the lagoon impede development of accurate inundation estimates near the near the bridge and around the pond.

In addition to the time series of the modeled water level and velocity dynamics, we added a supplemental appendix to this report that includes a map of the potential maximum subsidence in Sand Point (appendix B). According to scenario 6, the maximum subsidence in Sand Point could be about 3.2 m (10.5 ft). Most low-lying areas could be permanently flooded as a result of the hypothetical earthquake.

SOURCES OF ERRORS AND UNCERTAINTIES

The hydrodynamic model that we used to calculate propagation and runup of tsunami waves is a nonlinear, flux-formulated, shallow-water model (Nicolsky and others, 2011a). This model has passed the validation and verification tests required for models used in production of tsunami inundation maps (Synolakis and others, 2007; NTHMP, 2012). In the model benchmarking process, the tsunami inundation model had to demonstrate its capability to predict the inundation in most geophysical conditions. However, the local extreme runup, such as in the narrow gullies, is sensitive to the nearshore bathymetry/topography and could be underestimated by the numerical model (Nicolsky and others, 2011a). We do not take into account the tsunami–tide interactions in our model because the scientific research community has not yet reached a full understanding of possible interactions between tsunami and tides in shallow inlets. While the current model is validated to simulate the hypothetical inundation, it does not take into account the wave dispersion and cannot explicitly model origination and development of bore-like waves. Moreover, a hypothetical rupture of normal faults in concert with a subduction earthquake might produce some additional short-period waves that might also contribute to formation of bore-like waves. Therefore, the numerical modeling results can be used only as a guideline for predicting an actual inundation event.

The simulation of the 2011 Tohoku tsunami in Sand Point shows that the numerical code used does not accurately model the reflected and trapped waves of the 2011 tsunami because the resolution of the DEM is coarse in the vicinity of Sand Point and the model is affected by the accumulation of wave dispersion effects over time. The scenarios considered in this report could be affected by similar trapped waves that might not be captured by the numerical code; therefore, the predicted wave heights five hours or more after the tsunami's arrival at Sand Point might be underestimated by a factor of three (compare the modeled versus observed 2011 tsunami five hours after its arrival at Sand Point).

Because the initial condition for the modeling is determined by the displacement of the ocean bottom, the largest source of uncertainty in validating the results is the earthquake model. While constructing hypothetical maximum credible scenarios, we rely on current knowledge of the subduction processes and about regions where coseismic displacement might occur. When a tsunami is generated in the vicinity of the coast, the direction of the incoming waves, their amplitudes, and arrival times are determined by the initial displacements of the ocean floor in the source area, as the distance to the shore is too small for the waves to dissipate. Therefore, near-field inundation modeling results are sensitive to the structure of the tsunami source that is largely unknown in the first hours after the earthquake.

During development of tsunami inundation maps, we use a spatially averaged ground subsidence/uplift model. However, during a potential earthquake, soil compaction might occur in areas of unconsolidated deposits in the coastal zone and the tsunami inundation could extend farther landward. Our model does not address this source of uncertainty. Finally, the horizontal resolution of the grid used for inundation modeling is about 16 m (52.5 ft). This resolution is high enough to describe major relief features, but small topographic features, buildings, and other facilities cannot be resolved accurately by the existing model.

SUMMARY

This report presents results of numerical modeling for local and distant earthquake-generated tsunamis for Sand Point, Alaska. Hypothetical scenarios 1, 5, and 6 (a M_w 8.8–8.95 earthquake along the Shumagin Islands part of the subduction zone) result in the "worst case" tsunami inundation hazards for Sand Point. The magnitudes of the considered earthquake scenarios exceed the range of magnitudes (7–8) for the Shumagin segment in the USGS Probabilistic Seismic Hazard Assessment for Alaska (Wesson and others, 2007, 2008). However, we emphasize that each of the scenarios considered are geologically reasonable and present potential hazards to the community.

The maps showing the results of our modeling have been completed using the best information available and are believed to be accurate; however, their preparation required many assumptions. We considered several tectonic scenarios and provide an estimate of maximum credible tsunami inundation from each scenario. Actual conditions during a tsunami event may vary from those considered, contributing to the epistemic uncertainty of our results. The limits of inundation shown should be used only as a guideline for emergency planning and response action. Actual areas inundated will depend on specifics of the ground and seafloor deformation, land construction, and tide level, and could differ from the inundation areas shown on these maps. The information on these maps is intended to assist state and local agencies in planning emergency evacuation and tsunami response actions in the event of a major tsunamigenic earthquake. These results are not intended for land-use regulation or for building-code development.

ACKNOWLEDGMENTS

This project was supported by the National Oceanic and Atmospheric Administration (NOAA) under Reimbursable Services Agreement ADN 0931000 with the State of Alaska's Division of Homeland Security and Emergency Management (a division of the Department of Military and Veterans Affairs). Some of the research in this publication is sponsored by the Cooperative Institute for Alaska Research with funds from NOAA under cooperative agreement NA08OAR4320751 with the University of Alaska Fairbanks. Numerical calculations for this work were supported by a grant of High Performance Computing (HPC) resources from the Arctic Region Supercomputing Center (ARSC) at the University of Alaska Fairbanks. We thank Zebulon Maharrey for his help with the RTK GPS survey in Sand Point. We also express our gratitude to Douglas Christensen, Michael West, and Natasha Ruppert for their help in assessing

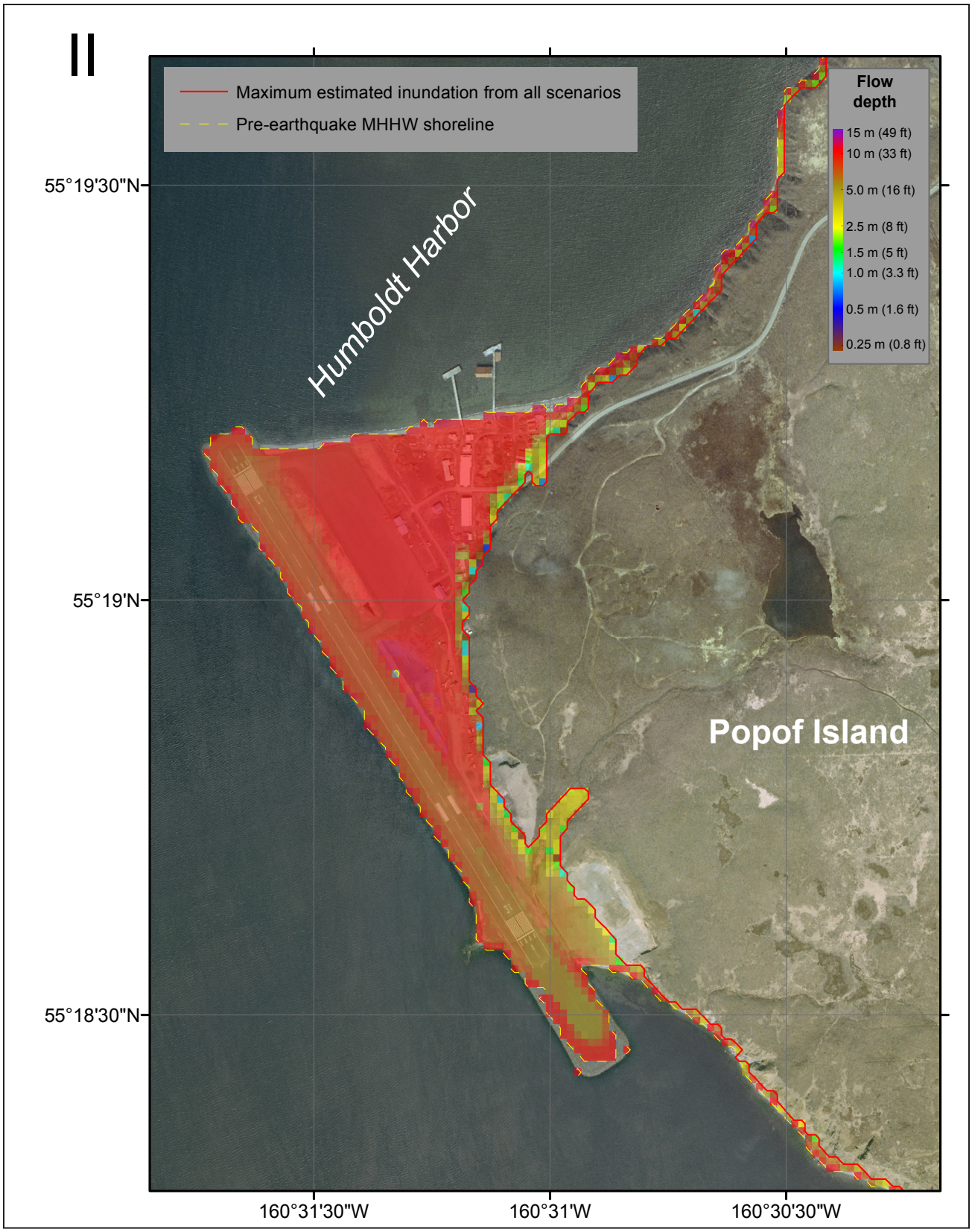

Figure 26, continued. Maximum composite potential inundation extent near the airport, and maximum composite flow depths over dry land. The DEM corresponds to the present-day MHHW datum.

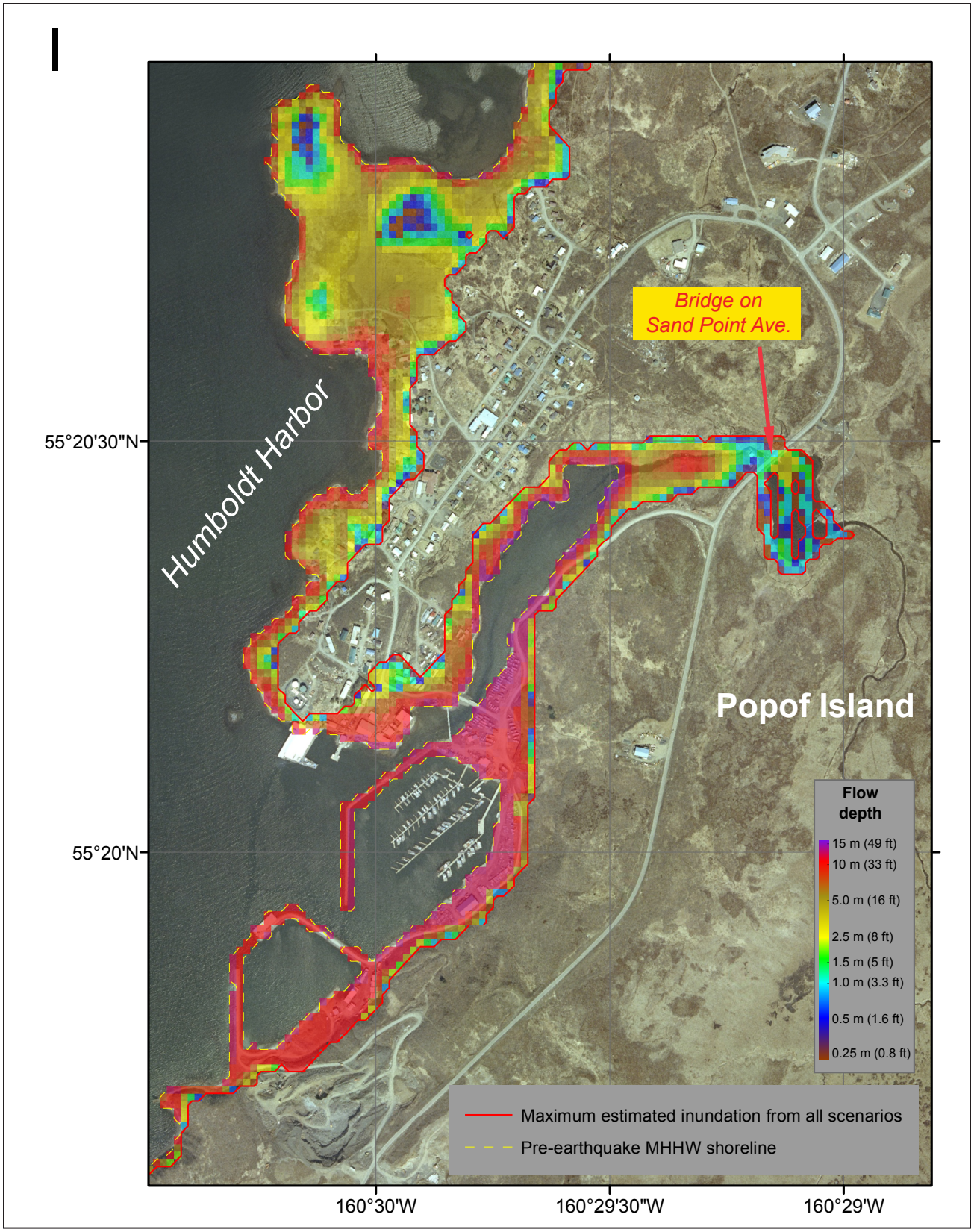

Figure 26. Maximum composite potential inundation extent (I) near the Sand Point harbor and maximum composite flow depths over dry land. The DEM corresponds to the present-day MHHW datum.

potential earthquakes along the Alaska Peninsula and the Aleutian Islands, and for sharing the data with us. Rob Witter provided valuable contributions to discussions on subduction-type tsunamigenic earthquakes along the Shumagin Islands. Reviews by Jason Patton and an anonymous reviewer improved the report and maps.

REFERENCES

Abe, Katsuyuki, 1972, Lithospheric normal faulting beneath the Aleutian Trench: Physics of the Earth and Planetary Interiors, v. 5, no. 3, p. 190–198.

Aki, Keiiti, 1984, Asperities, barriers, characteristic earthquakes and strong motion prediction: Journal of Geophysical Research, v. 89, no. B7, p. 5,867–5,872. http://dx.doi.org/10.1029/JB089iB07p05867

Alaska Department of Labor and Workforce Development (DLWD), 2013, Census and geographic information: State of Alaska, Department of Labor and Workforce Development. http://labor.alaska.gov/research/census/

Alaska Division of Community and Regional Affairs (DCRA), 2013, Community database online: State of Alaska, Department of Commerce, Community & Regional Affairs, Division of Community and Regional Affairs, http://commerce.alaska.gov/dnn/dcra/

Argus, D.F., Gordon, R.G., Heflin, M.B., Ma, Chopo, Eanes, R.J., Willis, Pascal, Peltier, W.R., and Owen, S.E., 2010, The angular velocities of the plates and the velocity of the Earth's centre from space geodesy: Geophysics Journal International, v. 180, no. 3, p. 913–960. http://dx.doi.org/10.1111/j.1365-246X.2009.04463.x

Don Argus kindly provided us with the GEODVEL NNR angular velocities.

Atakan, Kuwet, and Ojeda, Anibal, 2005, Stress transfer in the Storegga area, offshore mid-Norway: Marine and Petroleum Geology, v. 22, no. 1–2, p. 161–170. http://dx.doi.org/10.1016/j.marpetgeo.2004.10.005

Atwater, B.F., 1987, Evidence for great Holocene earthquakes along the outer coast of Washington state: Science, v. 236, p. 942–944.

Atwater, B.F., Musumi-Rokkaku, Satoku, Satake, Kenji, Tsuji, Yoshinobu, Ueda, Kazue, and Yamaguchi, D.K., 2005, The orphan tsunami of 1700—Japanese clues to a parent earthquake in North America: U.S. Geological Survey Professional Paper 1707 (prepared in cooperation with the Geological Survey of Japan, the University of Tokyo, and the University of Washington, and published in association with University of Washington Press), 133 p.

Blakely, R.J., Brocher, T.M., and Wells, R.E., 2005, Subduction-zone magnetic anomalies and implications for hydrated forearc mantle: Geology, v. 33, no. 6, p. 445–448.

Butler, Rhett, 2014, Great Aleutian tsunamis: Honolulu, HI, University of Hawai'i at Manoa, Hawai'i Institute of Geophysics & Planetology, Peer-Reviewed Report HIGP- 2014-1, 170 p. www.higp.hawaii.edu/reports/2014

Bryn, Petter, Berg, Kjell, Forsberg, C.F., Solheim, Anders, and Kvalstad, T.J., 2005, Explaining the Storegga slide: Marine and Petroleum Geology, v. 22, no. 1-2, p. 11–19. http://dx.doi.org/10.1016/j.marpetgeo.2004.12.003

Byrne, D.E., Davis, D.M., and Sykes, L.R., 1988, Loci and maximum size of thrust earthquakes and the mechanics of the shallow region of subduction zones: Tectonics, v. 7, no. 4, p. 833–857.

Caldwell, R.J., Eakins, B.W., and Lim, E., 2009, Digital elevation models of Prince William Sound, Alaska—Procedures, data sources, and analysis: Boulder, CO, National Geophysical Data Center, NOAA, 43 p. www.ngdc.noaa.gov/dem/report/download/1305

Carlson, P.R., Karl, H.A., and Edwards, B.D., 1991, Mass sediment failure and transport features revealed by acoustic techniques, Beringian margin, Bering Sea, Alaska: Marine Geotechnology, v. 10, no. 1-2, p. 33–51. http://dx.doi.org/10.1080/10641199109379881

Chen, Wang-Ping, and Molnar, Peter, 1983, Focal depths of intracontinental and intraplate earthquakes and their implications for the thermal and mechanical properties of the lithosphere: Journal of Geophysical Research, v. 88, no. B5, p. 4,183–4,214. http://dx.doi.org/10.1029/JB088iB05p04183

Christensen, D.H., and Ruff, L.J., 1988, Seismic coupling and outer rise earthquakes: Journal of Geophysical Research, v. 93, no. B11, p. 13,421–13,444, http://dx.doi.org/10.1029/JB093iB11p13421

Cox, D.C., and Morgan, Joseph, 1977, Local tsunamis and possible local tsunamis in Hawaii: Hawaii Institute of Geophysics, v. 77, no. 14, 118 p.

Cross, R.S., and Freymueller, J.T., 2008, Evidence for and implications of a Bering plate based on geodetic measurements from the Aleutians and western Alaska [abst.]: Journal of Geophysical Research, v. 113, no. B7, p. 405. http://dx.doi.org/10.1029/2007JB005136

Davies, J.N., Sykes, L.R., House, L.S., and Jacob, K.H., 1981, Shumagin seismic gap, Alaska Peninsula—History of great earthquakes, tectonic setting, and evidence for high seismic potential: Journal of Geophysical Research, v. 86, no. B5 p. 3,821–3,855. http://dx.doi.org/10.1029/JB086iB05p03821

DeMets, Charles, Gordon, R.C., Argus, D.F., and Stein, Seth, 1990, Current plate motions: Geophysical Journal International, v. 101, no. 2, p. 425–478. http://dx.doi.org/10.1111/j.1365-246X.1990.tb06579.x

Doroshin, Peter, 1870 [translated by J.B. Kisslinger, 1983], Some volcanoes, volcanic eruption, and earthquakes in the former Russian America—Peter Doroshin's 1870 account of volcanic activity and earthquakes between 1840 and 1866: Pacific Northwest Quarterly, v. 74, no. 2, p. 59–68.

Dunbar, P.K., and Weaver, C.S., 2008, U.S. states and territories national tsunami hazard assessment—Historical record and sources for waves: U.S. Geological Survey National Tsunami Hazard Mitigation Program, joint technical report with NOAA, 59 p. http://nws.weather.gov/nthmp/documents/Tsunami_Assessment_Final.pdf

Estabrook, C.H., and Boyd, T.M., 1992, The Shumagin Islands, Alaska earthquake of 31 May 1917: Bulletin of the Seismological Society of America, v. 82, p. 755–773.

Estabrook, C.H., Jacob, K.H., and Sykes, L.R., 1994, Body wave and surface wave analysis of large and great earthquakes along the eastern Aleutian arc, 1923–1993—Implications for future events: Journal of Geophysical Research, v. 99, no. B6, p. 11,643–11,662. http://dx.doi.org/10.1029/93JB03124

Fine, I.V., Rabinovich, A.B., Bornhold, B.D., Thompson, R.E., and Kulikov, E.A., 2005, The Grand Banks landslide-generated tsunami of November 18, 1929—Preliminary analysis and numerical modeling: Marine Geology, v. 215, no. 1-2, p. 45–57. http://dx.doi.org/10.1016/j.margeo.2004.11.007

Fletcher, H.J., Beavan, John, Freymueller, J.T., and Gilbert, Lewis, 2001, High interseismic coupling of the Alaska subduction zone SW of Kodiak Island inferred from GPS data: Geophysical Research Letters, v. 28, no. 3, p. 443–446, http://dx.doi.org/10.1029/2000GL012258

Foster, Evelyn, 1946, "Tidal Wave": Unga, Alaska, The Alaska Pen, Unga High School newspaper, p. 6.

Freund, L.B., and Barnett, D.M., 1976, A two-dimensional analysis of surface deformation due to dip-slip faulting: Bulletin of the Seismological Society of America, v. 66, no. 3, p. 667–675.

Fryer, G.J., and Watts, P., 2001, Motion of the Ugamak slide, probable source of the tsunami of 1 April 1946: Proceedings of the International Tsunami Symposium 2001, Session 6, NOAA PMEL, p. 683–694.

Fujii, Yushiro, Satake, Kenji, Sakai, Shin'ichi, Shinohara, Masanao, and Kanazawa, Toshihiko, 2011, Tsunami source of the 2011 off the Pacific coast of Tohoku earthquake: Earth Planets Space, v. 63, p. 815–820. http://www.terrapub.co.jp/journals/EPS/pdf/2011/6307/63070815.pdf

Geist, E.L., and Dmowska, Renata, 1999, Local tsunamis and distributed slip at the source: Pure and Applied Geophysics, v. 154, no. 3-4, p. 485–512, http://link.springer.de/link/service/journals/00024/index.htm

Grilli, S.T., Harris, J.C., Kirby, J.T., Shi, F., Ma, G., Masterlark, T., Tappin, D.R., and Tajali-Bakhsh, T.S., 2013, Modeling of the Tohoku-Oki 2011 tsunami generation, far-field and coastal impact—A mixed co-seismic and SMF source, in Bonneton, P., ed., Proceedings of the 7th International Conference on Coastal Dynamics: Arcachon, France, June 2013, paper 68, p. 749–758.

Gusman, A.R., Tanioka, Y., Matsumoto, H., and Iwasaki, S.I., 2009, Analysis of the tsunami generated by the great 1977 Sumba earthquake that occurred in Indonesia: Bulletin of the Seismological Society of America, v. 99, no. 4, p. 2,169–2,179. http://dx.doi.org/10.1785/0120080324

Hayes, G.P., Wald, D.J., and Johnson, R.L., 2012, Slab1.0—A three-dimensional model of global subduction zone geometries: Journal of Geophysical Research, v. 117, no. B1, 1 p., http://dx.doi.org/10.1029/2011JB008524

Heise, Wiebke, Caldwell, T.G., Bertrand, E.A., Hill, G.J., Bennie, S.L., and Ogawa, Yasuo, 2013, Changes in electrical resistivity track changes in tectonic plate coupling: Geophysical Research Letters, v. 40, no. 19, p. 5,029–5,033. http://dx.doi.org/10.1002/grl.50959

Hyndman, R.D., Wang, K., and Yamano, M., 1995, Thermal constraints on the seismogenic portion of the southwestern Japan subduction thrust: Journal of Geophysical Research, v. 100, no. B8, p. 15,373–15,392. http://dx.doi.org/10.1029/95JB00153

Johnson, J.M., and Satake, Kenji, 1993, Source parameters of the 1957 Aleutian earthquake from tsunami waveforms: Geophysical Research Letters, v. 20, no. 14, p. 1,487–1,490. http://dx.doi.org/10.1029/93GL01217

Johnson, J.M., and Satake, Kenji, 1994, Rupture extent of the 1938 Alaskan earthquake as inferred from tsunami waveforms: Geophysical Research Letters, v. 21, no. 8, p. 733–736. http://dx.doi.org/10.1029/94GL00333

Kanamori, Hiroo, 1970, The Alaska earthquake of 1964—Radiation of long-period surface waves and source mechanism: Journal of Geophysical Research, v. 75, no. 26, p. 5,029–5,040. http://dx.doi.org/10.1029/JB075i026p05029

Kanamori, Hiroo, 1971, Seismological evidence for a lithospheric normal faulting—The Sanriku earthquake of 1933: Physics of the Earth and Planetary Interiors, v. 4, no. 4, p. 289–300. http://dx.doi.org/10.1016/0031-9201(71)90013-6

Kato, Naoyuki, and Seno, Tetsuzo, 2003, Hypocenter depths of large interplate earthquakes and their relation to seismic coupling: Earth and Planetary Science Letters, v. 210, no. 1-2, p. 53–63. http://dx.doi.org/10.1016/S0012-821X(03)00141-9

Kaye, David, 2003, Spatial correlation of subduction interplate coupling and forearc morpho-tectonics: Corvallis, Oregon State University, M.S. Thesis.

Keefer, D.K., 1984, Landslides caused by earthquakes: Geological Society of America Bulletin, v. 95, no. 4, p. 406–421. http://dx.doi.org/10.1130/0016-7606(1984)95<406:LCBE>2.0.CO;2

Kelleher, John, Sykes, Lynn, and Oliver, Jack, 1973, Possible criteria for predicting earthquake locations and their application to major plate boundaries of the Pacific and the Caribbean: Journal of Geophysical Research, v. 78, no. 14, p. 2,547–2,585. http://dx.doi.org/10.1029/JB078i014p02547

Kirby, Stephen, Scholl, David, von Huene, Roland, and Wells, Ray, 2013, Alaska earthquake source for the SAFRR tsunami scenario, chapter B, in Ross, S.L., and Jones, L.M., eds., The SAFRR (Science Application for Risk Reduction) Tsunami Scenario: U.S. Geological Survey Open-File Report 2013–1170, 40 p., http://pubs.usgs.gov/of/2013/1170/b/

Kowalik, Zygmunt, and Murty, T.S., 1984, Computation of tsunami amplitudes resulting from a predicted major earthquake in the Shumagin seismic gap: Geophysical Research Letters, v. 11, no. 12, p. 1,243–1,246. http://dx.doi.org/10.1029/GL011i012p01243

Kulikov, E.A., Rabinovich, A.B., Fine, I.V., Bornhold, B.D., and Thomson, R.E., 1998, Tsunami generation by landslides at the Pacific coast of North America and the role of tides: Oceanology, v. 38, no. 3, p. 323–328.

Kvalstad, T.J., Andresen, Lars, Forsberg, C.F., Berg, Kjell, Bryn, Petter, and Wangen, Magnus, 2005, The Storegga slide—Evaluation of triggering sources and slide mechanics: Marine and Petroleum Geology, v. 22, no. 1-2, p. 245–256. http://dx.doi.org/10.1016/j.marpetgeo.2004.10.019

Lander, J.F., 1996, Tsunamis affecting Alaska, 1737–1996: Boulder, CO, National Oceanic and Atmospheric Administration, National Geophysical Data Center (NGDC), Key to Geophysical Research Documentation, v. 31, 155 p.

Lander, J.F., and Lockridge, P.A., 1989, Tsunami in Alaska, chapter 3, in United States Tsunamis (including United States possessions), 1690–1988: U.S. Department of Commerce, National Oceanic and Atmospheric Administration, National Geophysical Data Center (NGDC). Publication 41-2, 265 p. http://www.ngdc.noaa.gov/hazard/data/publications/pub41-2.pdf

Leica Geosystems AG, 2002, GPS User Manual, Version 4: Leica Geosystems AG, Heerbrugg, Switzerland, 62 p.

Lopez, A.M., and Okal, E.A., 2006, A seismological reassessment of the source of the 1946 Aleutian 'tsunami' earthquake: Geophysical Journal International, v. 165, no. 3, p. 835–849. http://dx.doi.org/10.1111/j.1365-246X.2006.02899.x

Love M.R., Friday, D.Z., Grothe, P.R., Carignan, K.S., Eakins, B.W., and Taylor, L.A., 2012, Digital elevation models of Sand Point, Alaska, v2—Procedures, data sources and analysis: Boulder, CO, NOAA, PMEL, National Geophysical Data Center (NGDC). http://www.ngdc.noaa.gov/dem/squareCellGrid/download/3549

Masson, D.G., Harbitz, C.B., Wynn, R.B., Pedersen, G., and Løvholt, F., 2006, Submarine landslides—Processes, triggers and hazard prediction: Philosophical Transactions of the Royal Society A, v. 364, no. 1,845, p. 2,009–2,039. http://dx.doi.org/10.1098/rsta.2006.1810

Miller, J.J., and von Huene, R., 2013, A possible Tohoku-magnitude tsunami along the Alaska Peninsula—The 1946 Scotch Cap Tsunami [abst.]: Abstracts of the 2013 AGU Fall Meeting, abstract #T23D-2619.

Miller, J.J., von Huene, Roland, and Ryan, H., 2014, The 1946 Unimak tsunami earthquake area—Revised tectonic structure in reprocessed seismic images and a suspect near-field tsunami source: U.S. Geological Survey Open-File Report 2014–1024, 19. p. http://dx.doi.org/10.3133/ofr20141024

Moreno, M.S., Bolte, J., Klotz, J., and Melnick, D., 2009, Impact of megathrust geometry on inversion of coseismic slip from geodetic data—Application to the 1960 Chile earthquake: Geophysical Research Letters, v. 36, no. 16, L16310. http://dx.doi.org/10.1029/2009GL039276

National Earthquake Center (NEC), 2013, Earthquake Hazards Program, catalog of earthquakes: U.S. Geological Survey, ANSS Comprehensive Catalog (ComCat). http://earthquake.usgs.gov/earthquakes/search/

National Geophysical Data Center/World Data Service (NGDC/WDS), 2013, Global historical tsunami database: Boulder, CO, NOAA NGDC, technical report. http://www.ngdc.noaa.gov/hazard/tsu_db.shtml

National Tsunami Hazard Mapping Program (NTHMP), 2010, Guidelines and best practices for tsunami inundation modeling for evacuation planning: NTHMP Mapping & Modeling Subcommittee, NOAA.

———2012, Proceedings and Results of the 2011 NTHMP Model Benchmarking Workshop, Boulder: U.S. Department of Commerce/NOAA/NTHMP, NOAA Special Report, 436 p. http://nthmp.tsunami.gov

Nicolsky, D.J., 2012, Alaska tsunami model, in Proceedings and Results of the 2011 NTHMP Model Benchmarking Workshop: Boulder, CO, U.S. Department of Commerce/NOAA/NTHMP, NOAA Special Report, p. 55–87. http://nthmp.tsunami.gov

Nicolsky, D.J., Suleimani, E.N., and Hansen, R.A., 2011a, Validation and verification of a numerical model for tsunami propagation and runup: Pure and Applied Geophysics, v. 168, p. 1,199–1,222. http://dx.doi.org/10.1007/s00024-010-0231-9

Nicolsky, D.J., Suleimani, E.N., Combellick, R.A., and Hansen, R.A., 2011b, Tsunami inundation maps of Whittier and western Passage Canal, Alaska: Alaska Division of Geological & Geophysical Surveys Report of Investigation 2011-7, 65 p. http://dx.doi.org/10.14509/23244

Nicolsky, D.J., Suleimani, E.N., Freymueller, J.T., and Koehler, R.D., 2015, Tsunami inundation maps of Fox Islands communities, including Dutch Harbor and Akutan, Alaska: Alaska Division of Geological & Geophysical Surveys Report of Investigation 2015-5, 67 p., 2 sheets, scale 1:12,500. http://dx.doi.org/10.14509/29414

Nishenko, S.P., and Jacob, K.H., 1990, Seismic potential of the Queen Charlotte–Alaska–Aleutian seismic zone: Journal of Geophysical Research, v. 95, no. B3, p. 2,511–2,532. http://dx.doi.org/10.1029/JB095iB03p02511

Okada, Yoshimitsu, 1985, Surface deformation due to shear and tensile faults in a half-space: Bulletin of the Seismological Society of America, v. 75, no. 4, p. 1,135–1,154.

Oleskevich, D.A., Hyndman, R.D., and Wang, K., 1999, The updip and downdip limits to great subduction earthquakes—Thermal and structural models of Cascadia, south Alaska, SW Japan, and Chile: Journal of Geophysical Research, v. 104, no. B7, p. 14,965–14,991. http://dx.doi.org/10.1029/1999JB900060

Pacheco, J.F., Sykes, L.R., and Scholz, C.H., 1993, Nature of seismic coupling along simple plate boundaries of the subduction type: Journal of Geophysical Research, v. 98, no. B8, p. 14,133–14,159. http://dx.doi.org/10.1029/93JB00349

Page, R.A., Biswas, N.N., Lahr, J.C., and Pulpan, Hans, 1991, Seismicity of continental Alaska, in Slemmons, D.B., Engdahl, E.R., Zoback, M.D., and Blackwell, D.D., eds., Neotectonics of North America: Boulder, Colorado, Geological Society of America, Decade Map, v. 1, p. 47–68.

Perry, Alexis M., 1875, Note sur les Tremblements de Terre en 1871, avec Supplements pour les Annees Anterieures de 1843 a 1870—Memoires Courorines et Autre Metnoires: Brussels, Belgium, 1'Academie Royal des Sciences, des Lettres et des Beaux Arte de Belgique, v. XXIV, no. 8, p. 1–143.

Plafker, George, Kachadoorian, Reuben, Eckel, E.B., and Mayo, L.R., 1969, Effects of the earthquake of March 27, 1964, on various communities: U.S. Geological Survey Professional Paper 542-G, 50 p.

Priest, G.R., Goldfinger, Chris, Wang, Kelin, Witter, R.C., Zhang, Yinglong, and Baptista, A.M., 2009, Confidence levels for tsunami-inundation limits in northern Oregon inferred from a 10,000-year history of great earthquakes at the Cascadia subduction zone: Natural Hazards, v. 54, no. 1. http://dx.doi.org/10.1007/s11069-009-9453-5

Ross, S.L., Jones, L.M., Miller, Kevin, P., K.A., Wein, A., Wilson, Ri.I., Bahng, B., Barberopoulou, A., Borrero, J.C., Brosnan, D.M., Bwarie, J.T., Geist, E.L., Johnson, L.A., Kirby, S.H., Knight, W.R., Long, K., Lynett, P., Mortensen, C.E., Nicolsky, D.J., Perry, S.C., Plumlee, G.S., Real, C.R., Ryan, K., Suleimani, E., Thio, H., Titov, V.V., Whitmore, P.M., and Wood, N.J., 2013, SAFRR (Science Application for Risk Reduction) Tsunami Scenario—Chapter A, Executive Summary and Introduction, in Ross, S.L., and Jones, L.M., eds., The SAFRR Tsunami Scenario: U.S. Geological Survey Open-File Report 2013–1170, p. 1–17. http://pubs.usgs.gov/of/2013/1170/

Ruff, Larry, and Kanamori, Hiroo, 1983, Seismic coupling and uncoupling at subduction zones: Tectonophysics, v. 99, no. 2-4, p. 99–117.

Ryan, Holly, von Huene, Roland, Scholl, Dave, and Kirby, Steve, 2012, Tsunami hazards to U.S. coasts from giant earthquakes in Alaska: Eos Transactions, American Geophysical Union, v. 93, no. 19, p. 185–186. http://dx.doi.org/10.1029/2012EO190001

Satake, Kenji, Shimazaki, Kunihiko, Tsuji, Yoshinobu, and Ueda, Kazue, 1996, Time and size of a giant earthquake in Cascadia inferred from Japanese tsunami records of January 1700: Nature, v. 379, no. 6,562, p. 246–249. http://dx.doi.org/10.1038/379246a0

Satake, Kenji, Wang, Kelin, and Atwater, B.F., 2003, Fault slip and seismic moment of the 1700 Cascadia earthquake inferred from Japanese tsunami descriptions: Journal of Geophysical Research, v. 108, no. B11, p. 2,535–2,551. http://dx.doi.org/10.1029/2003JB002521

Savage, J.C., 1983, A dislocation model of strain accumulation and release at a subduction zone: Journal of Geophysical Research, v. 88, no. B6, p. 4,984–4,996. http://dx.doi.org/10.1029/JB088iB06p04984

Schwab, W.C., Lee, H.J., and Twichell, D.C., eds., 1993, Submarine landslides—Selected studies in the U.S. Exclusive Economic Zone: U.S. Geological Survey Bulletin 2002, 204 p.

Scholz, C.H., 1998, Earthquakes and friction laws: Nature, v. 391, p. 37–42. http://dx.doi.org/10.1038/34097

Scholz, C.H., and Campos, Jaime, 2012, The seismic coupling of subduction zones revisited: Journal of Geophysical Research—Solid Earth, v. 117, no. B5, p. 5,310. http://dx.doi.org/10.1029/2011JB009003

Shao, Guangfu, Li, Xiangyu, Ji, Chen, and Maeda, Takahiro, 2011, Focal mechanism and slip history of 2011 M_w 9.1 off the Pacific coast of Tohoku earthquake, constrained with teleseismic body and surface waves: Earth Planets Space, v. 63, no. 7, p. 559–564. http://dx.doi.org/10.5047/eps.2011.06.028

Sobolev, S.V., Babeyko, A.Y., Wang, Rongjiang, Hoechner, Andreas, Galas, Roman, Rothacher, Markus, Sein, D.V., Schröter, Jens, Lauterjung, Joern, and Subarya, Cecep, 2007, Tsunami early warning using GPS-shield arrays: Journal of Geophysical Research, v. 112, no. B08, p. 415. http://dx.doi.org/10.1029/2006JB004640

Soloviev, S.L., 1968, The Sanak Kodiak Island tsunami of 1788 [in Russian]: Moscow, Nauka, The Tsunami Problem, p. 232–237. [English translation in Science of Tsunami Hazards, v. 8, no. 1, p. 34–38, 1990.]

Song, Teh-Ru Alex, and Simons, Mark, 2003, Large trench-parallel gravity variations predict seismogenic behavior in subduction zones: Science, v. 301, no. 5,633, p. 630–633. http://dx.doi.org/10.1126/science.1085557

Stauder, W., 1968a, Mechanism of the Rat Island earthquake sequence of February 4, 1965, with relation to island arcs and sea floor spreading: Journal of Geophysical Research, v. 73, no. 12, p. 3,847–3,858. http://dx.doi.org/10.1029/JB073i012p03847

Stauder, W., 1968b, Tensional character of earthquake foci beneath the Aleutian Trench with relation to sea-floor spreading: Journal of Geophysical Research, v. 73, no. 24, p. 7,693–7,701. http://dx.doi.org/10.1029/JB073i024p07693

Stein, Seth, and Okal, E.A., 2007, Ultralong period seismic study of the December 2004 Indian Ocean earthquake and implications for regional tectonics and the subduction process: Bulletin of the Seismological Society of America, v. 97, no. 1A, p. S279–S295. http://dx.doi.org/10.1785/0120050617

Stover, C.W., and Coffman, J.L., 1993, Seismicity of the United States, 1568–1989: U.S. Geological Survey Professional Paper 1527, 418 p.

Sykes, L.R., 1971, Aftershock zones of great earthquakes, seismicity gaps, and earthquake prediction for Alaska and the Aleutians: Journal of Geophysical Research, v. 76, no. 32, p. 8,021–8,041. http://dx.doi.org/10.1029/JB076i032p08021

Sykes, L.R., Kisslinger, J.B., House, Leigh, Davies, J.N., and Jacob, K.H., 1981, Rupture zones and repeat times of great earthquakes along the Alaska–Aleutian Arc, 1784–1980, in Simpson, D.W., and Richards, P.G., eds., Earthquake Prediction: Washington, D.C., American Geophysical Union Maurice Ewing Series, v. 4, p. 73–80.

Synolakis, C.E., Bernard, E.N., Titov, V.V., Kânoğlu, U., and González, F.I., 2007, Standards, criteria, and procedures for NOAA evaluation of tsunami numerical models: Seattle, NOAA/Pacific Marine Environmental Laboratory, Technical Memorandum OAR PMEL-135, 55 p.

Tang, Liujuan, Titov, V.V., Bernard, E.N., Wei, Yong, Chamberlain, C.D., Newman, J.C., Mofjeld, H.O., Arcas, Diego, Eble, M.C., Moore, Christopher, Uslu, Burak, Pells, Clint, Spillane, Michael, Wright, Lindsey, and Gica, Edison, 2012, Direct energy estimation of the 2011 Japan tsunami using deep-ocean pressure measurements: Journal of Geophysical Research—Oceans, v. 117, no. C8, p. 8. http://dx.doi.org/10.1029/2011JC007635

Tarr, R.S., Martin, Lawrence, and Gilbert, G.K., 1912, The earthquakes at Yakutat Bay, Alaska, in September, 1899; with a preface by G.K. Gilbert: U.S. Geological Survey Professional Paper 69, 135 p., 3 sheets, scale 1:5,000,000.

Tichelaar, B.W., and Ruff, L.J., 1993, Depth of seismic coupling along subduction zones: Journal of Geophysical Research, v. 98, no. B2, p. 2,017–2,037. http://dx.doi.org/10.1029/92JB02045

Uchida, Naoki, Nakajima, Junichi, Hasegawa, Akira, and Matsuzawa, Toru, 2009, What controls interplate coupling?—Evidence for abrupt change in coupling across a border between two overlaying plates in the NE Japan subduction zone: Earth and Planetary Science Letters, v. 283, no. 1-4, p. 111–121. http://dx.doi.org/10.1016/j.epsl.2009.04.003

Uyeda, Seiya, 1982, Subduction zones—An introduction to comparative subductology: Tectonophysics, v. 81, no. 3-4, p. 133–159. http://dx.doi.org/10.1016/0040-1951(82)90126-3

Wang, Kelin, Wells, R.E., Mazzotti, Stephane, Hyndman, R.D., and Sagiya, Takeshi, 2003, A revised dislocation model of interseismic deformation of the Cascadia subduction zone: Journal of Geophysical Research, v. 108, no. B1, p. 2,026–2,038. http://dx.doi.org/10.1029/2001JB001227

Wang, Kelin, and Dixon, Timothy, 2004, "Coupling" semantics and science in earthquake research: Eos Transactions, American Geophysical Union, v. 85, no. 18, p. 180–181. http://dx.doi.org/10.1029/2004EO180005

Waythomas, C.F., Watts, Philip, Shi, Fengyan, and Kirby, J.T., 2009, Pacific basin tsunami hazards associated with mass flows in the Aleutian arc of Alaska: Quaternary Science Reviews, v. 28, no. 11-12, p. 1,006–1,019. http://dx.doi.org/10.1016/j.quascirev.2009.02.019

Wesson, R.L., Boyd, O.S., Mueller, C.S., Bufe, C.G., Frankel, A.D., and Petersen, M.D., 2007, Revision of time-independent probabilistic seismic hazard maps for Alaska: U.S. Geological Survey Open-File Report 2007–1043, 33 p.

Wesson, R.L., Boyd, O.S., Mueller, C.S., and Frankel, A.D., 2008, Challenges in making a seismic hazard map for Alaska and the Aleutians, in Freymueller, J.T., Haeussler, P.J., Wesson, R., and Ekström, G., eds., Active Tectonics and Seismic Potential of Alaska: Washington, D.C., American Geophysical Union, Geophysical Monograph v. 179, p. 385–397.

Winslow, M.A., and Johnson, L.L., 1989, Prehistoric human settlement patterns in a tectonically unstable environment, outer Shumagin Islands, southwestern Alaska: Geoarchaeology, v. 4, no. 4, p. 297–318. http://dx.doi.org/10.1002/gea.3340040402

Witter, R.C., Briggs, R.W., Engelhart, S.E., Gelfenbaum, G., Koehler, R.D., and Barnhart, W., 2014, Little late Holocene strain accumulation and release on the Aleutian megathrust below the Shumagin Islands, Alaska: Geophysical Research Letters, v. 41, no. 7, p. 2,359–2,367. http://dx.doi.org/10.1002/2014GL059393

Witter, R.C., Zhang, Y., Wang, K., Priest, G.R., Goldfinger, C., Stimely, L.L., English, J.T., and Ferro, P.A., 2011, Simulating tsunami inundation at Bandon, Coos County, Oregon, using hypothetical Cascadia and Alaska earthquake scenarios: Oregon Department of Geology and Mineral Industries Special Paper 43, 57 p. http://www.oregongeology.org/pubs/sp/p-SP-43.htm

Wu, F.T., and Kanamori, Hiroo, 1973, Source mechanism of February 4, 1965, Rat Island earthquake: Journal of Geophysical Research, v. 78, no. 26, p. 6,082–6,092. http://dx.doi.org/10.1029/JB078i026p06082

Zweck, Chris, Freymueller, J.T., and Cohen, S.C., 2002, Three-dimensional elastic dislocation modeling of the postseismic response to the 1964 Alaska earthquake: Journal of Geophysical Research, v. 107, no. B4, p. 2,064. http://dx.doi.org/10.1029/2001JB000409

APPENDIX A

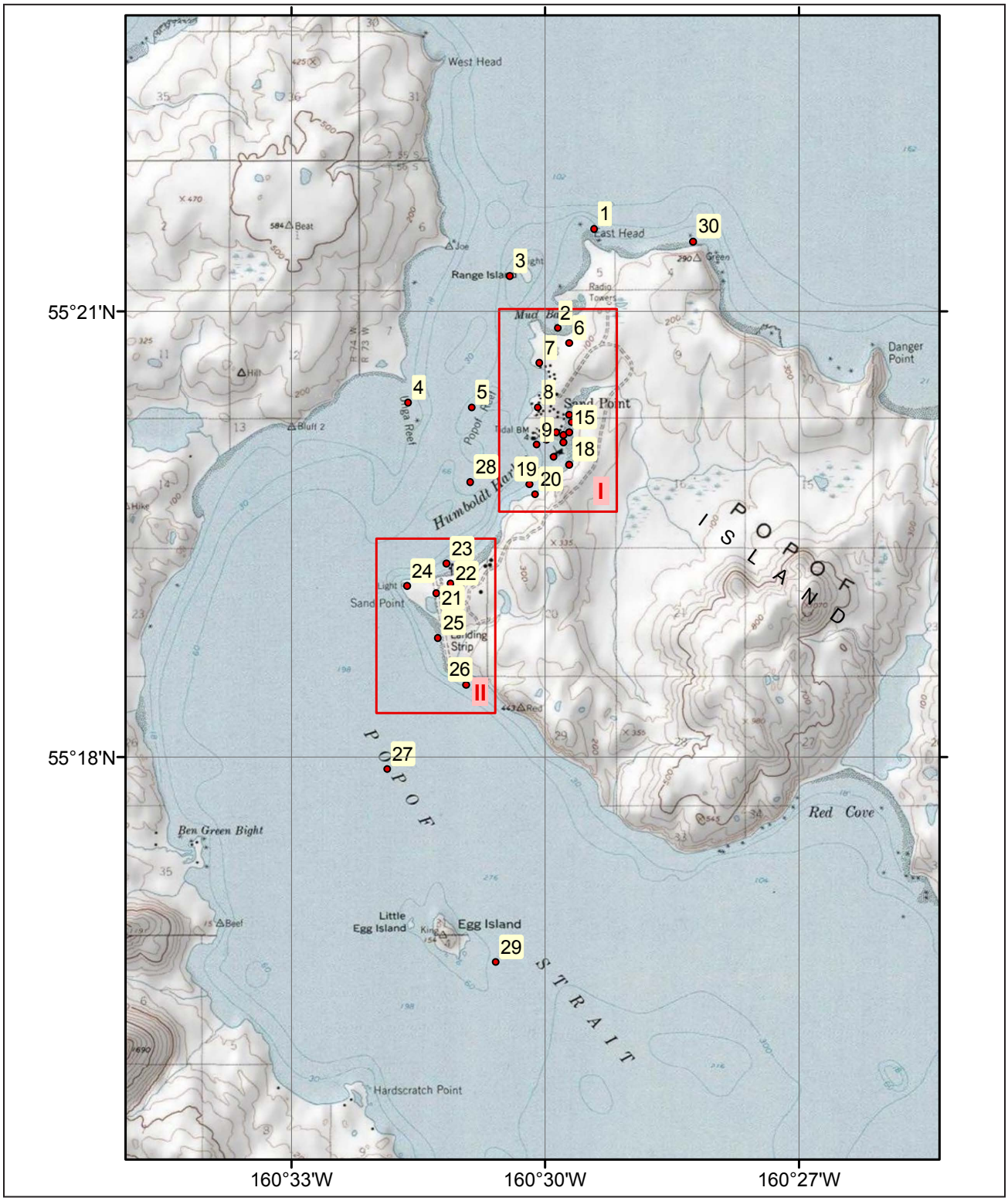

Figure A-1. Locations of time-series points around Popof Island in Popof Strait and Humboldt Harbor. Red rectangles mark areas that are enlarged in appendix A-2 (I and II). Longitude and latitude locations of time-series points are listed in table 4.

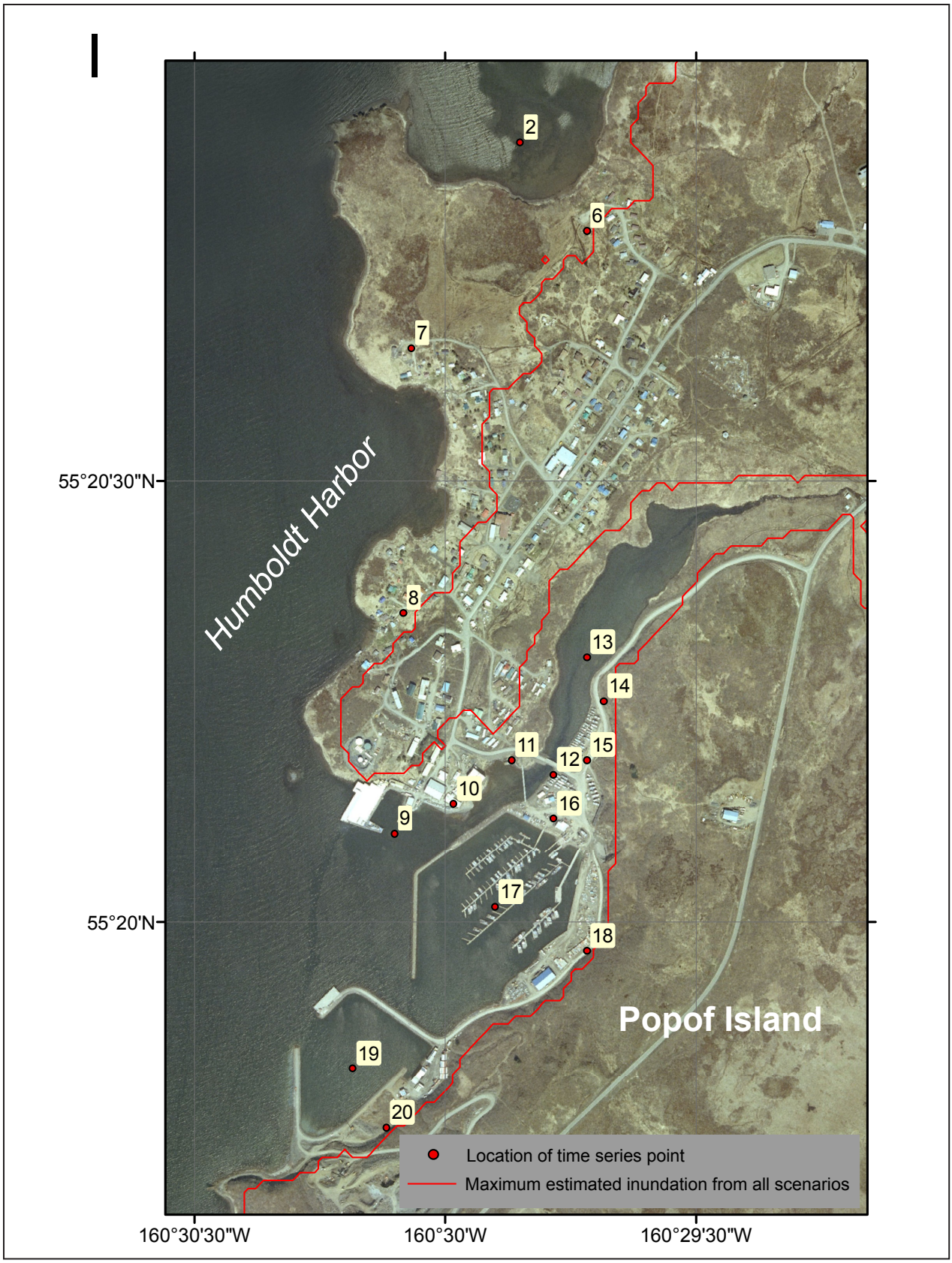

Figure A-2. Locations of time-series points (I) near the Sand Point harbor and (II) near the airport. Longitude and latitude locations of time-series points are listed in table 4.

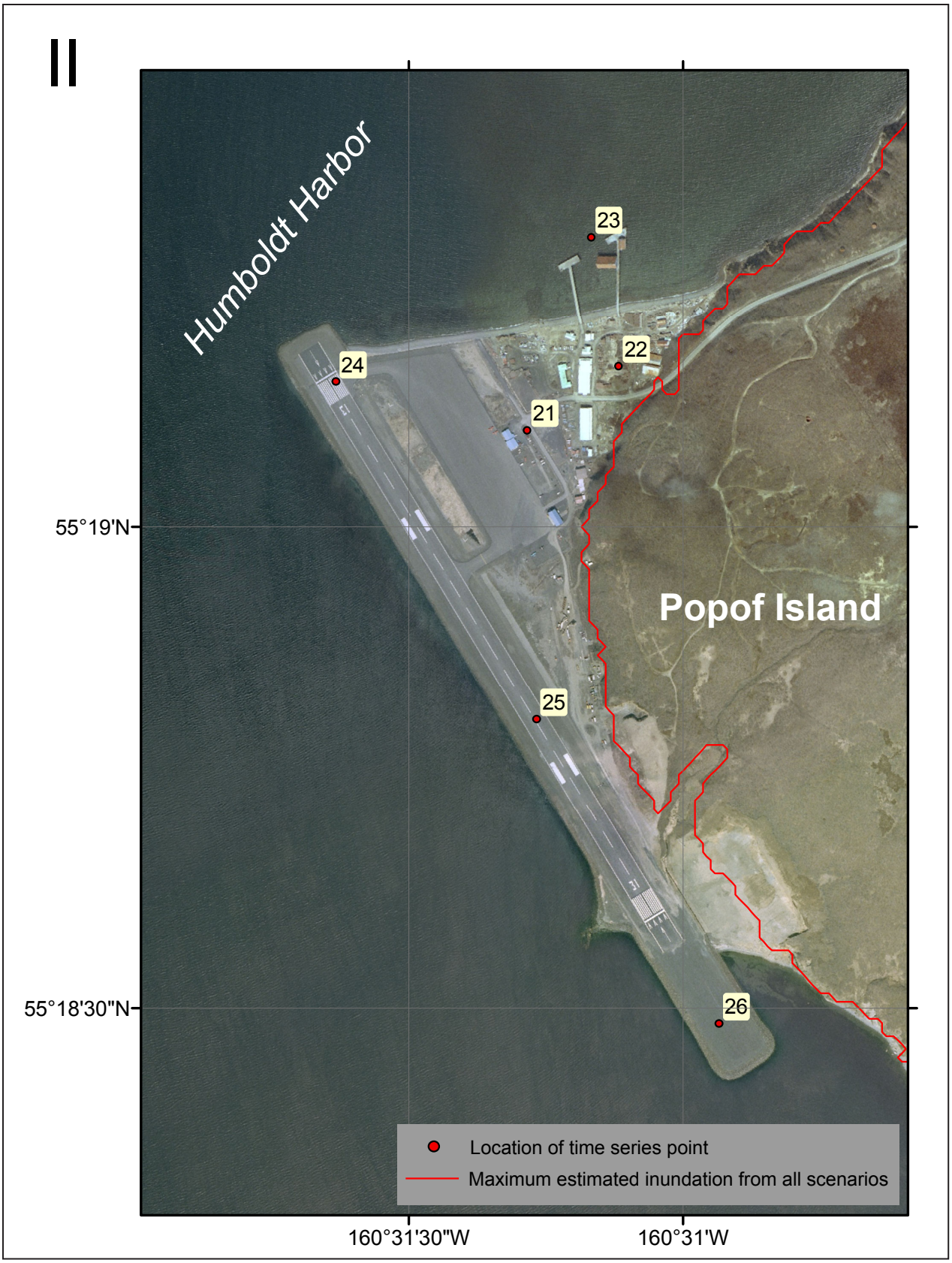

Figure A-2, continued. Locations of time-series points (I) near the Sand Point harbor and (II) near the airport. Longitude and latitude locations of time-series points are listed in table 4.

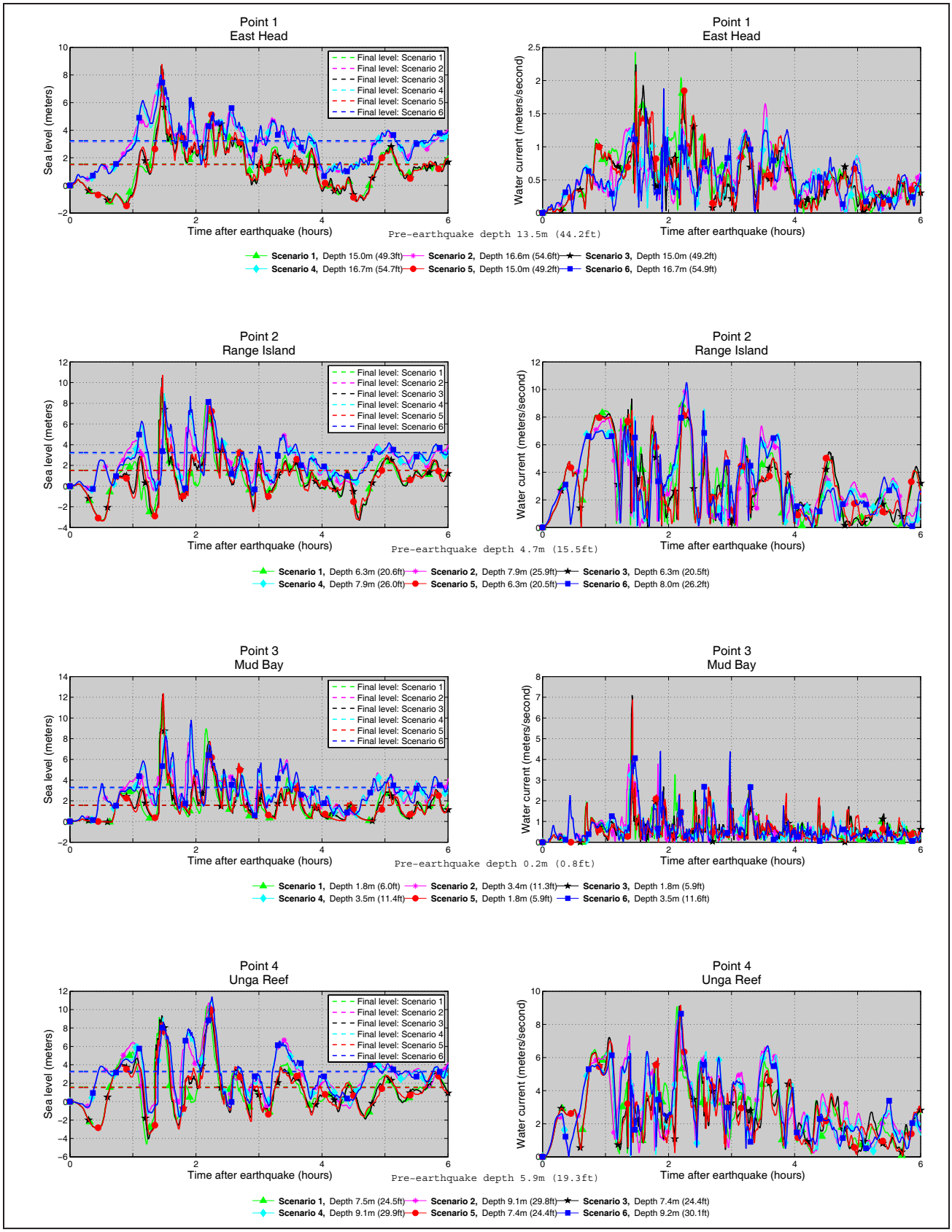

Figure A-3. Time series of water level and velocity at selected locations in Sand Point for scenarios 1–6. Elevations of onshore locations correspond to post-earthquake MHHW datum. For offshore locations, to show the height of an arriving tsunami the vertical datum is such that zero corresponds to the pre-earthquake sea level.

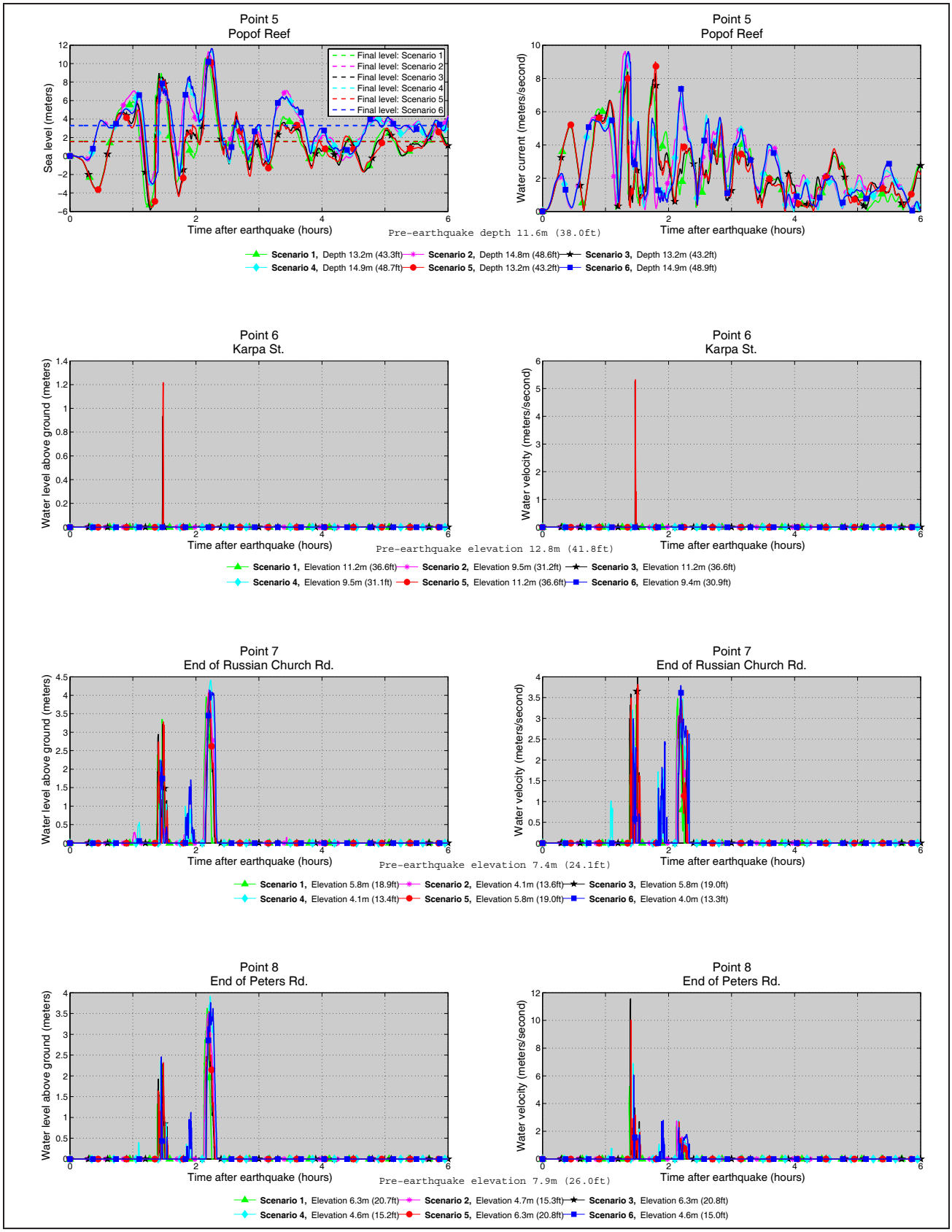

Figure A-3, continued. Time series of water level and velocity at selected locations in Sand Point for scenarios 1–6. Elevations of onshore locations correspond to post-earthquake MHHW datum. For offshore locations, to show the height of an arriving tsunami the vertical datum is such that zero corresponds to the pre-earthquake sea level.

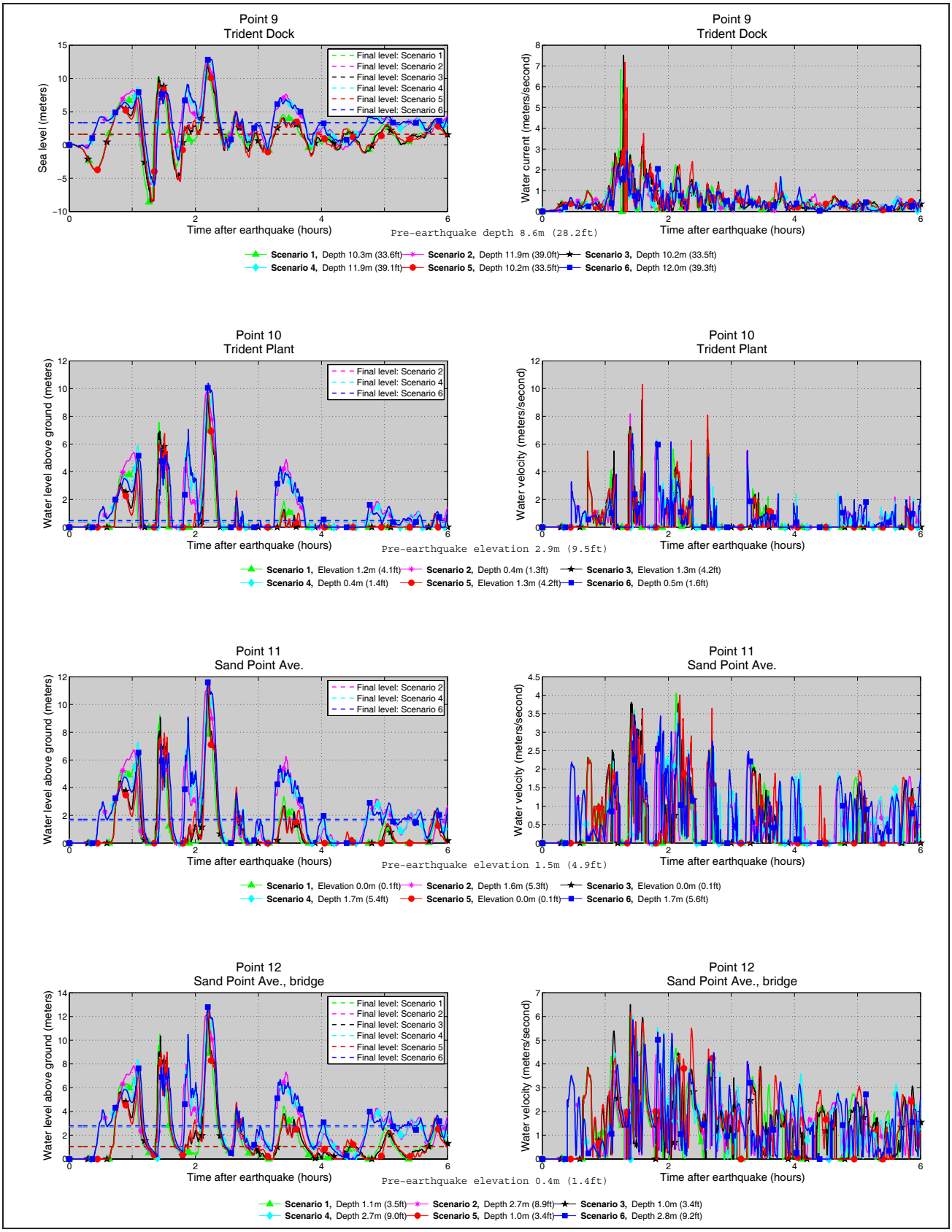

Figure A-3, continued. Time series of water level and velocity at selected locations in Sand Point for scenarios 1–6. Elevations of onshore locations correspond to post-earthquake MHHW datum. For offshore locations, to show the height of an arriving tsunami the vertical datum is such that zero corresponds to the pre-earthquake sea level.

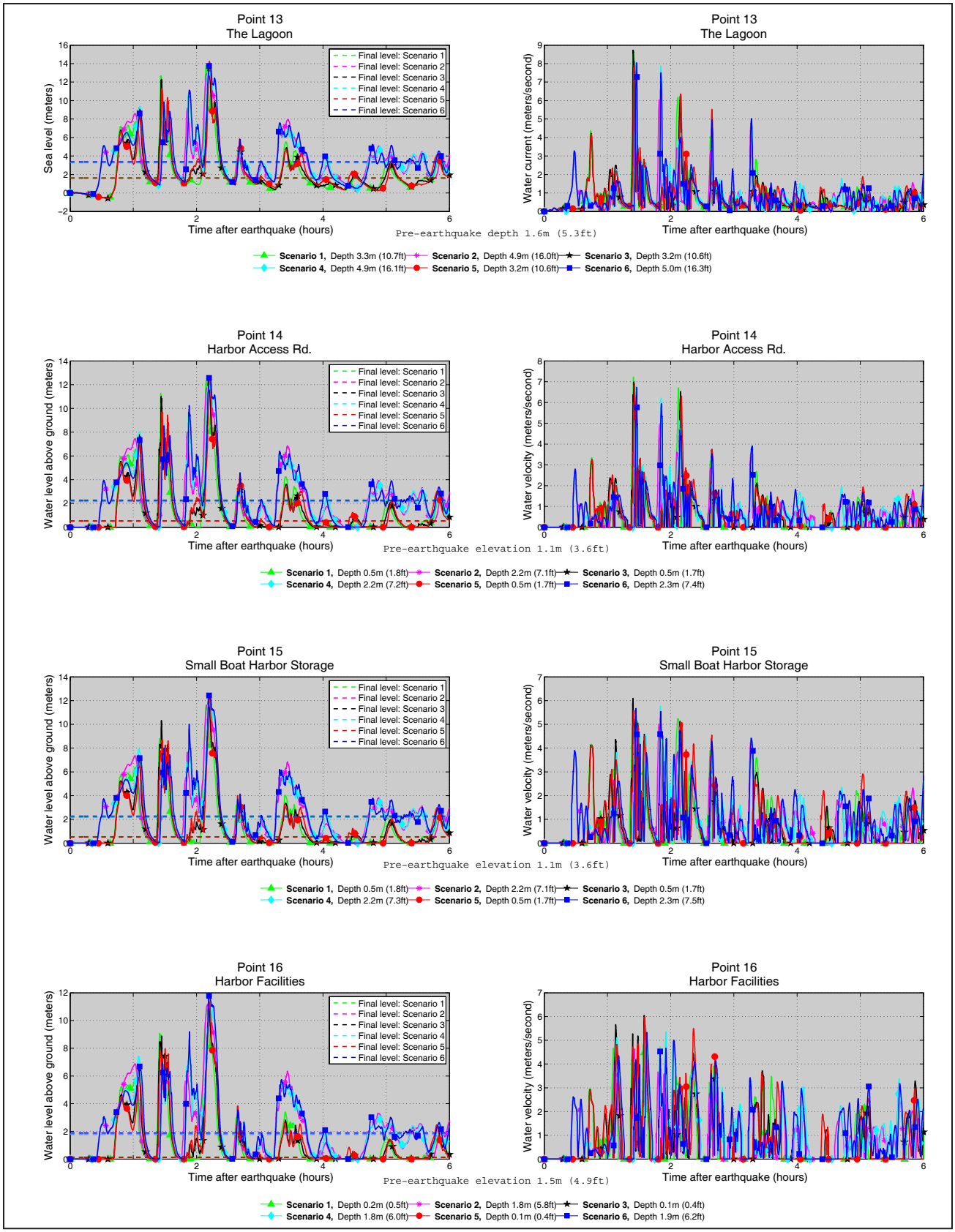

Figure A-3, continued. Time series of water level and velocity at selected locations in Sand Point for scenarios 1–6. Elevations of onshore locations correspond to post-earthquake MHHW datum. For offshore locations, to show the height of an arriving tsunami the vertical datum is such that zero corresponds to the pre-earthquake sea level.

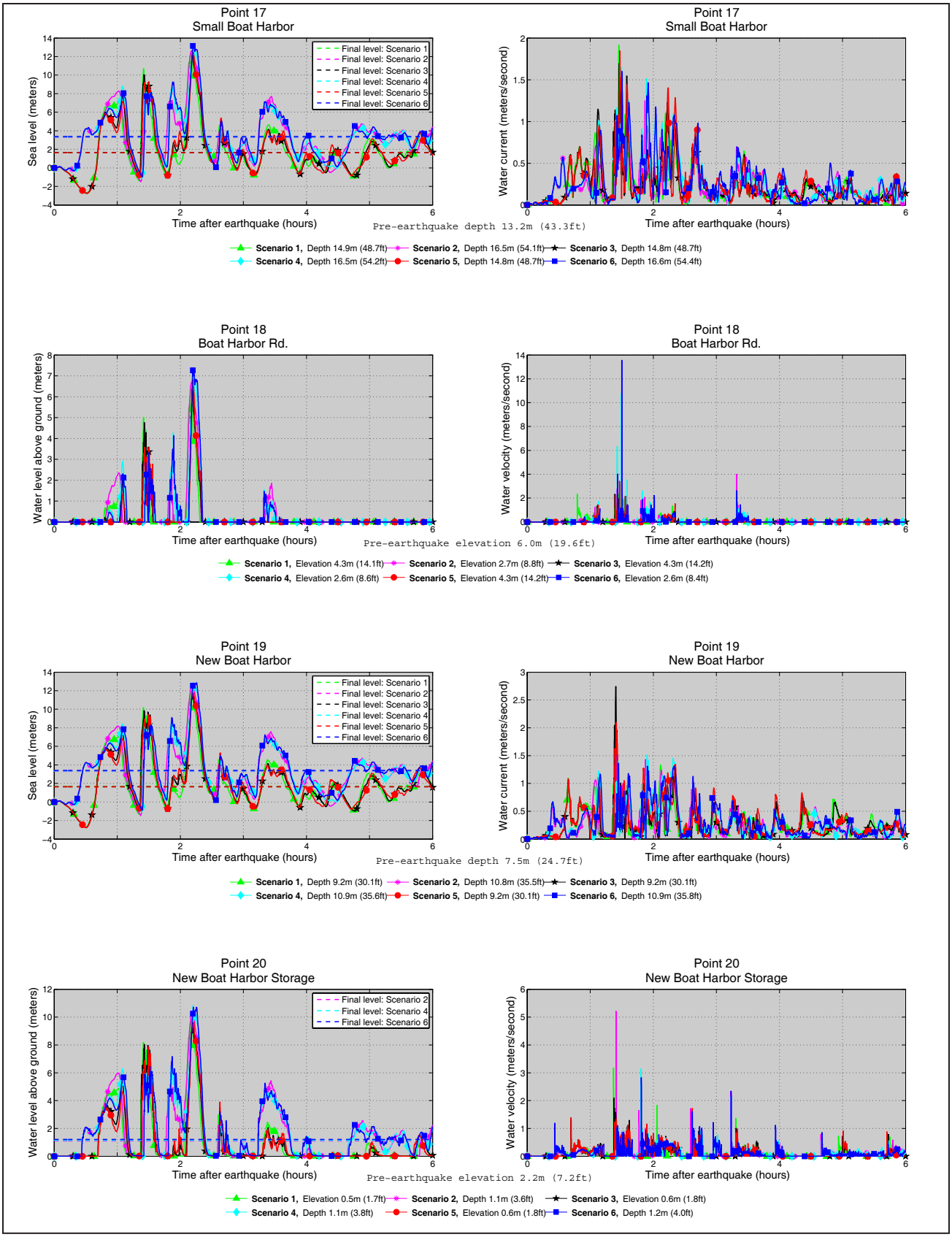

Figure A-3, continued. Time series of water level and velocity at selected locations in Sand Point for scenarios 1–6. Elevations of onshore locations correspond to post-earthquake MHHW datum. For offshore locations, to show the height of an arriving tsunami the vertical datum is such that zero corresponds to the pre-earthquake sea level.

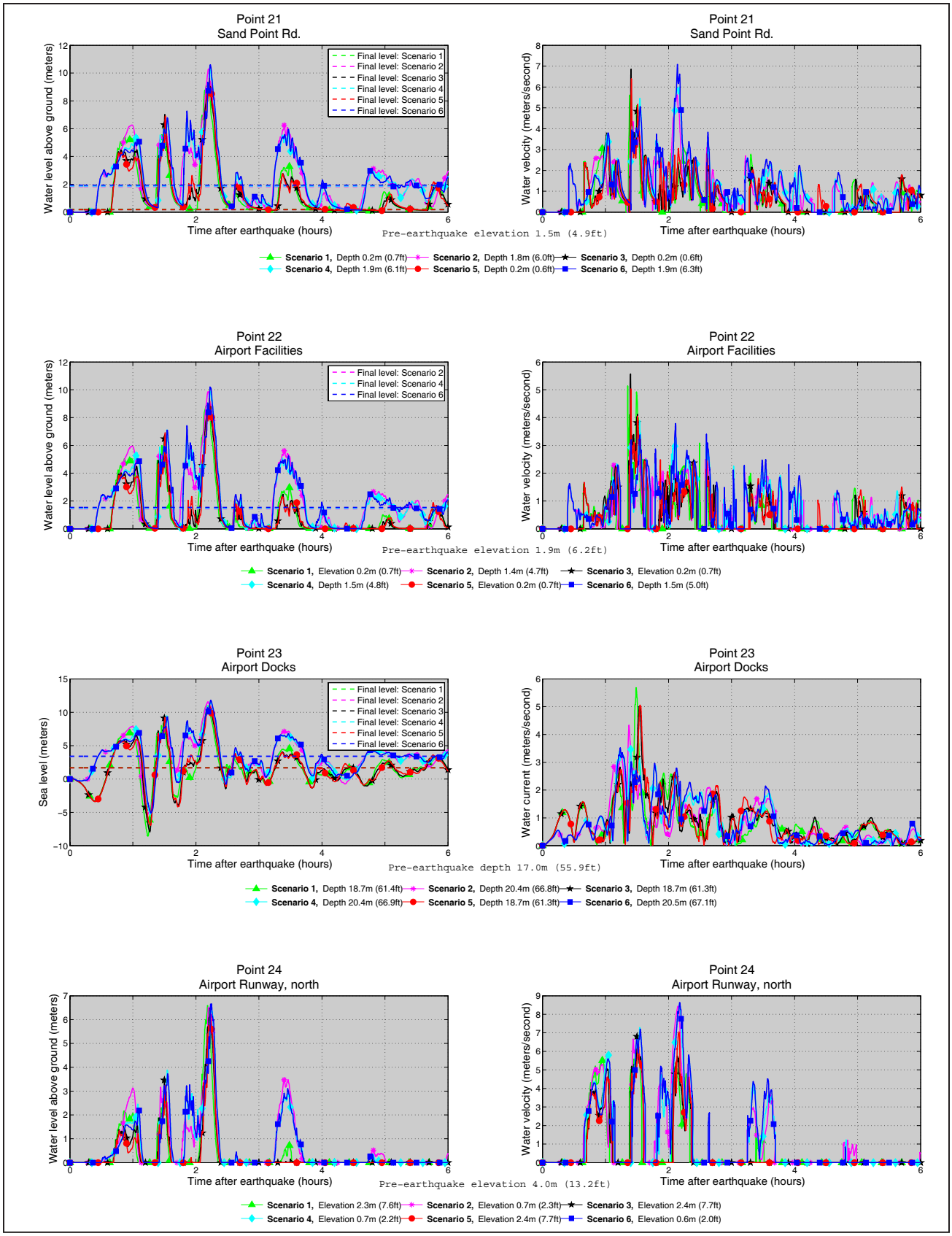

Figure A-3, continued. Time series of water level and velocity at selected locations in Sand Point for scenarios 1–6. Elevations of onshore locations correspond to post-earthquake MHHW datum. For offshore locations, to show the height of an arriving tsunami the vertical datum is such that zero corresponds to the pre-earthquake sea level.

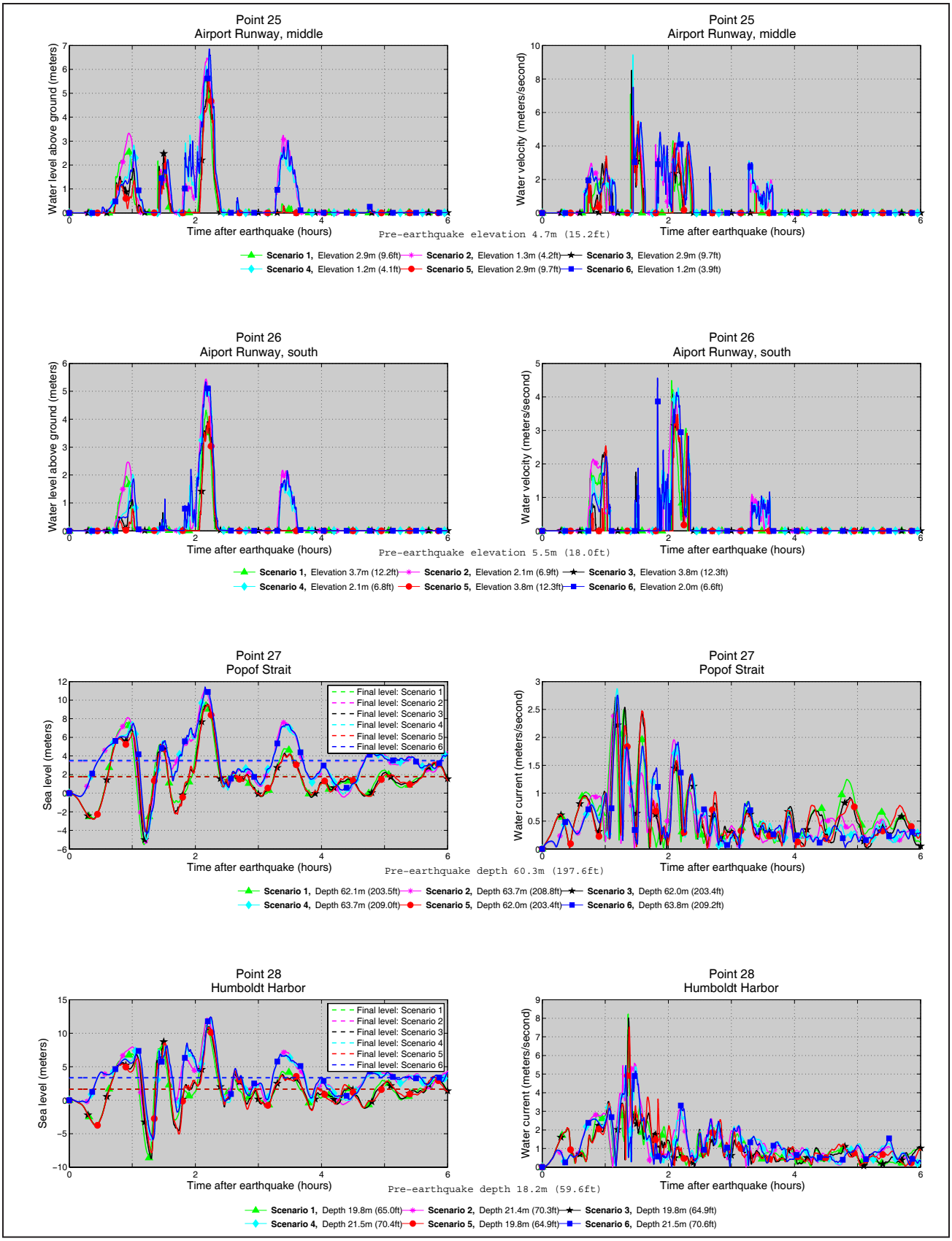

Figure A-3, continued. Time series of water level and velocity at selected locations in Sand Point for scenarios 1–6. Elevations of onshore locations correspond to post-earthquake MHHW datum. For offshore locations, to show the height of an arriving tsunami the vertical datum is such that zero corresponds to the pre-earthquake sea level.

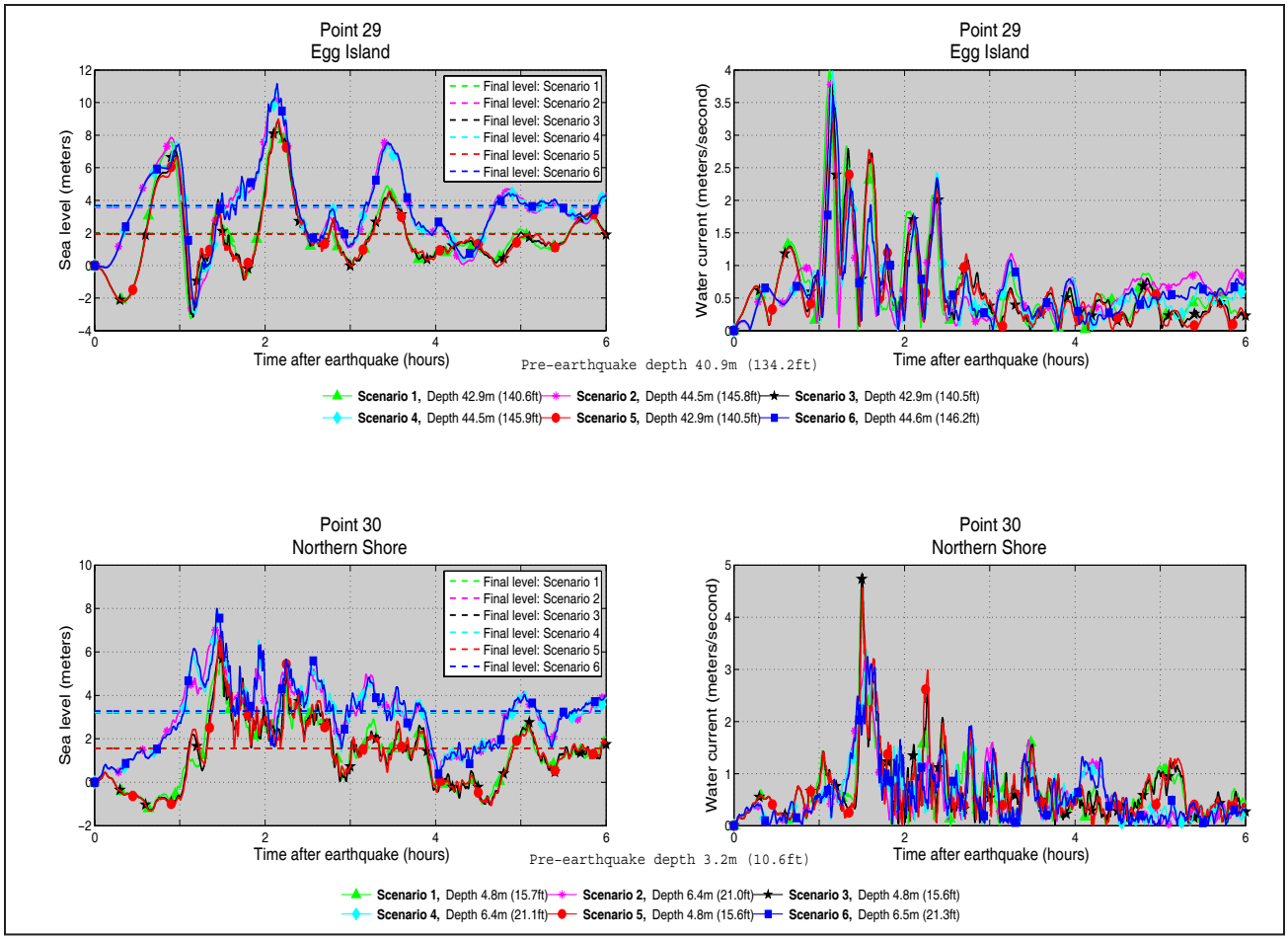

Figure A-3, continued. Time series of water level and velocity at selected locations in Sand Point for scenarios 1–6. Elevations of onshore locations correspond to post-earthquake MHHW datum. For offshore locations, to show the height of an arriving tsunami the vertical datum is such that zero corresponds to the pre-earthquake sea level.

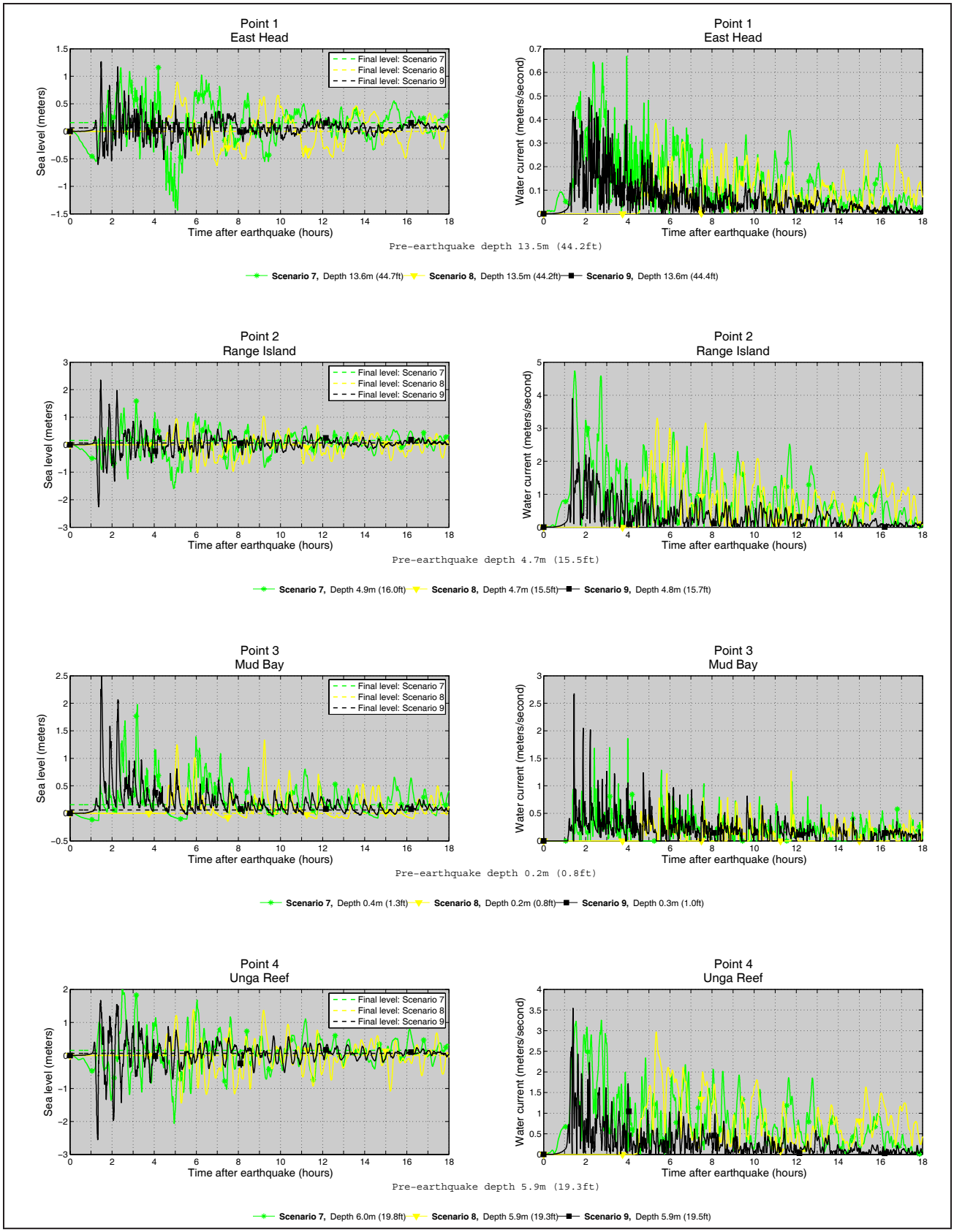

Figure A-4. Time series of water level and velocity at selected offshore locations for scenarios 7–9. Elevations of onshore locations correspond to post-earthquake MHHW datum. For offshore locations, to show the height of an arriving tsunami the vertical datum is such that zero corresponds to the pre-earthquake sea level.

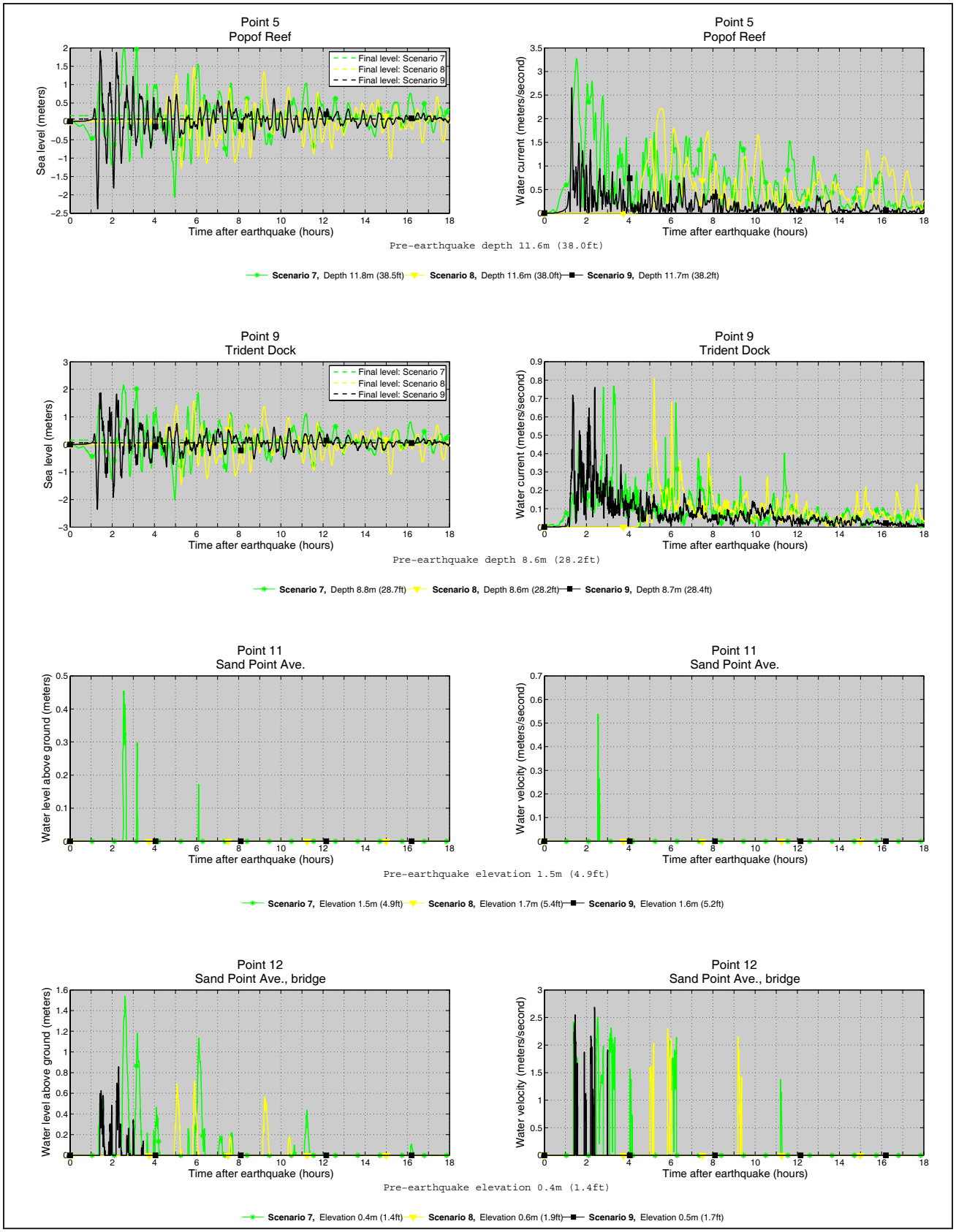

Figure A-4, continued. Time series of water level and velocity at selected offshore locations for scenarios 7–9. Elevations of onshore locations correspond to post-earthquake MHHW datum. For offshore locations, to show the height of an arriving tsunami the vertical datum is such that zero corresponds to the pre-earthquake sea level.

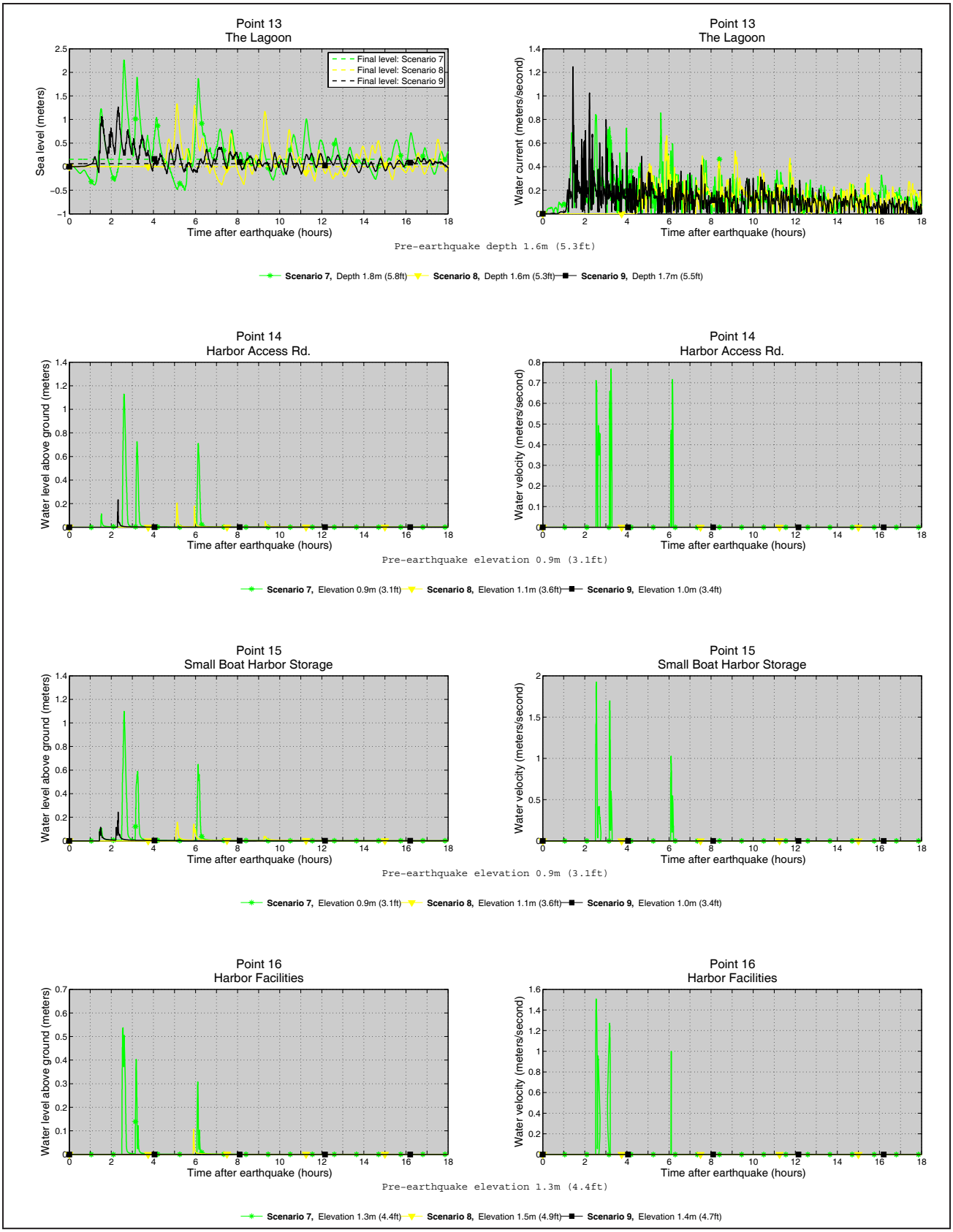

Figure A-4, continued. Time series of water level and velocity at selected offshore locations for scenarios 7–9. Elevations of onshore locations correspond to post-earthquake MHHW datum. For offshore locations, to show the height of an arriving tsunami the vertical datum is such that zero corresponds to the pre-earthquake sea level.

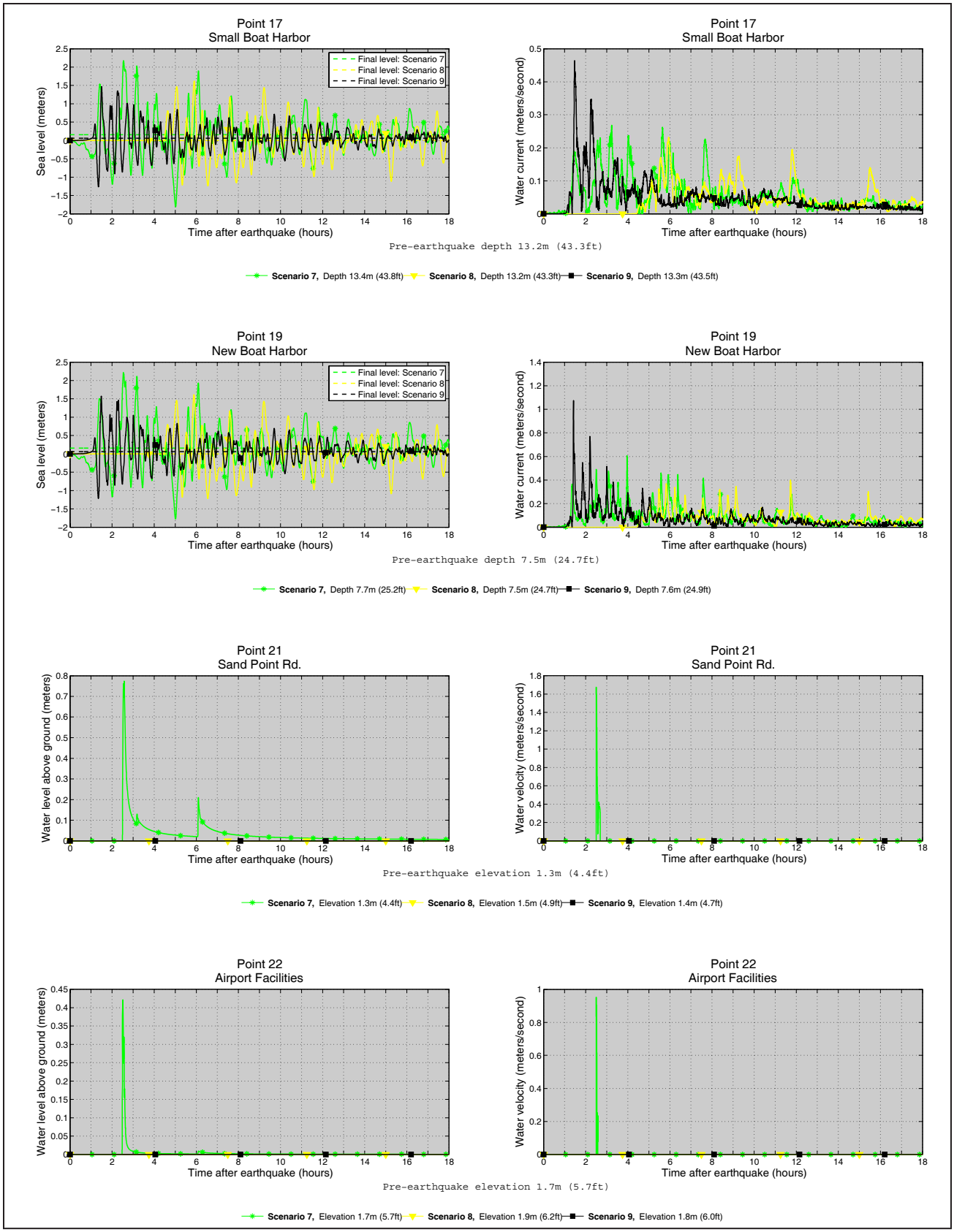

Figure A-4, continued. Time series of water level and velocity at selected offshore locations for scenarios 7–9. Elevations of onshore locations correspond to post-earthquake MHHW datum. For offshore locations, to show the height of an arriving tsunami the vertical datum is such that zero corresponds to the pre-earthquake sea level.

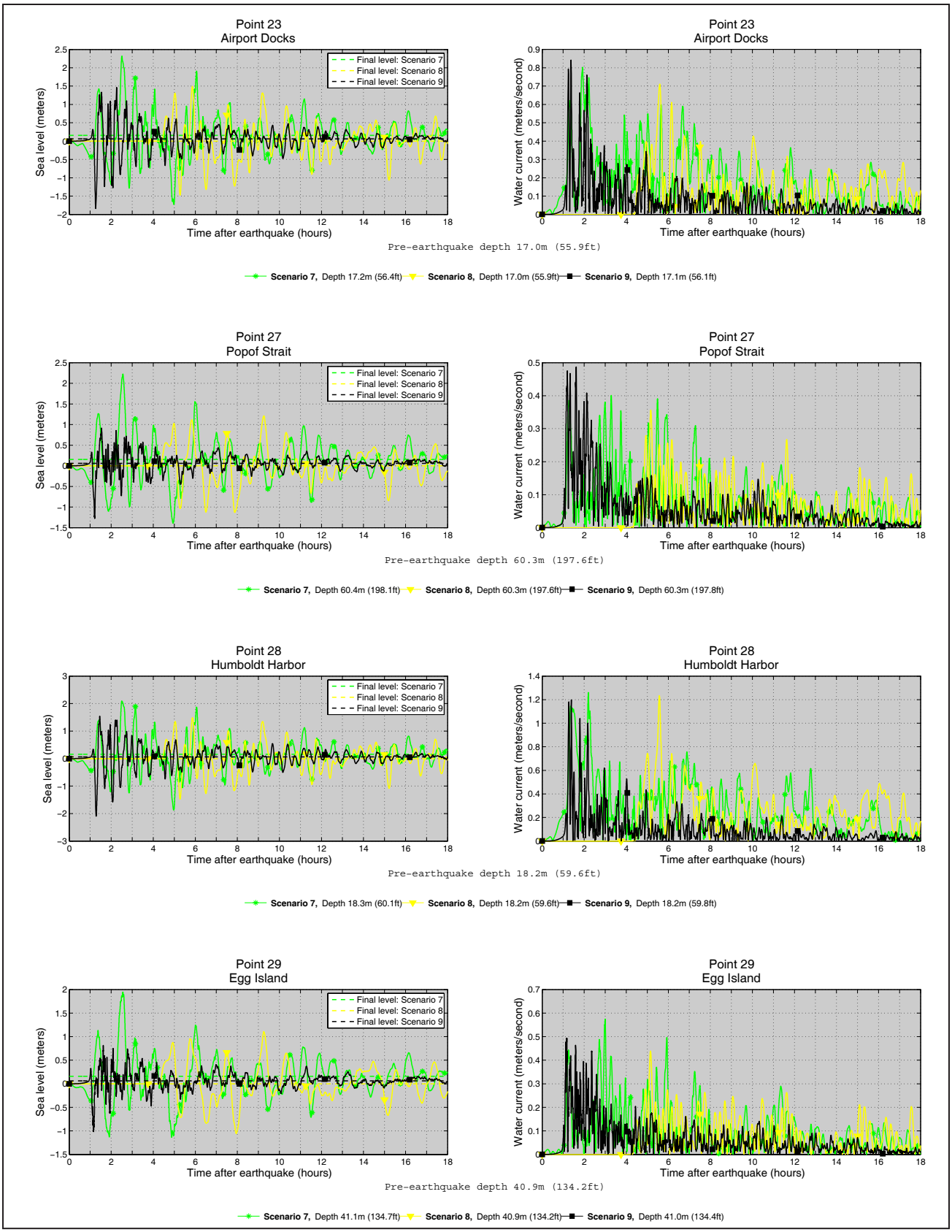

Figure A-4, continued. Time series of water level and velocity at selected offshore locations for scenarios 7–9. Elevations of onshore locations correspond to post-earthquake MHHW datum. For offshore locations, to show the height of an arriving tsunami the vertical datum is such that zero corresponds to the pre-earthquake sea level.

APPENDIX B

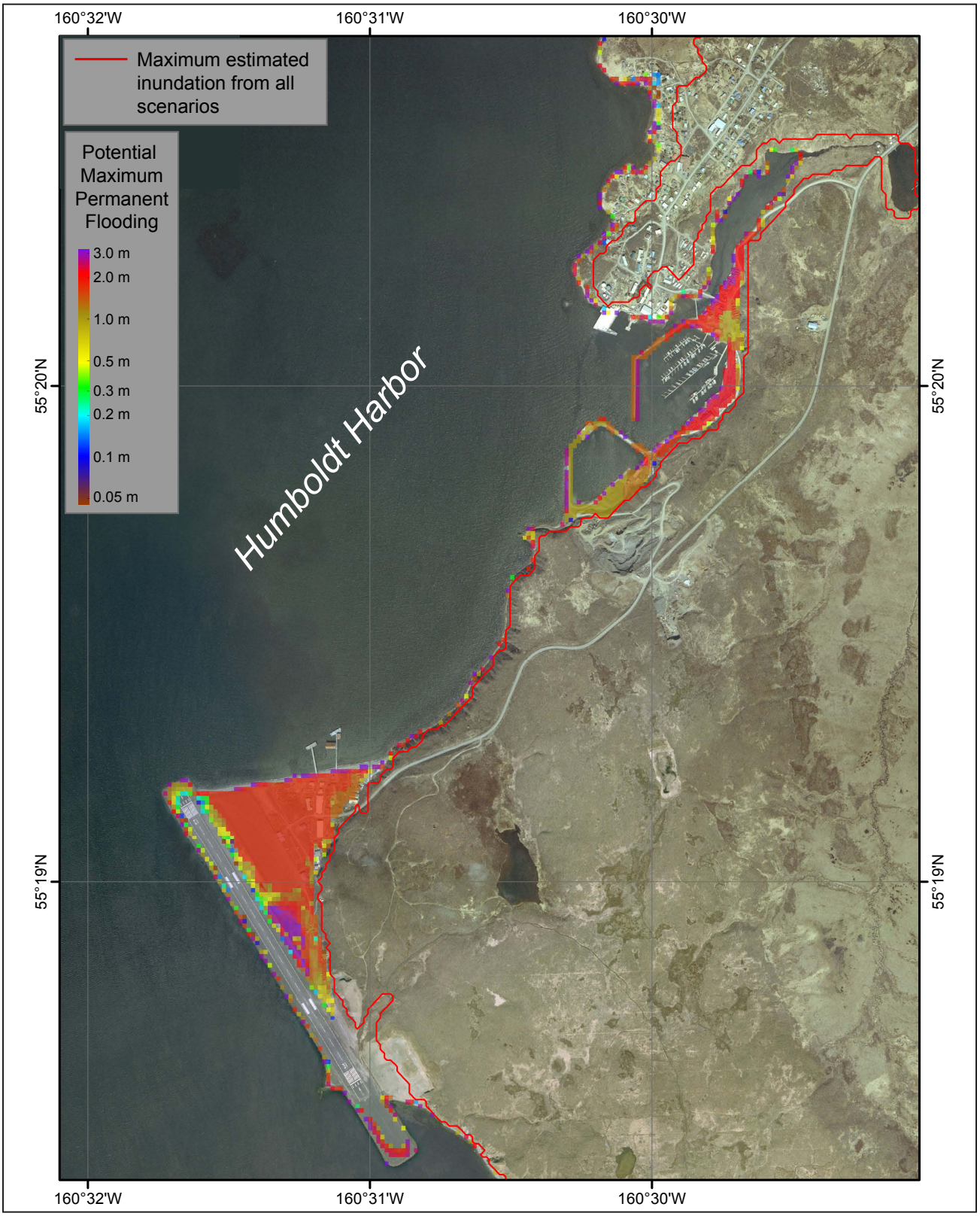

Appendix B-1. Map showing potential maximum permanent flooding in Sand Point. Values of the subsidence according to each scenario are listed in table 2.